Computational Phase Imaging based on Intensity Transport

by

Laura A. Waller

B.S., Massachusetts Institute of Technology (2004)
M.Eng., Massachusetts Institute of Technology (2005)

Submitted to the Department of
Electrical Engineering and Computer Science
in partial fulfillment of the requirements for the degree of

Doctor of Philosophy in Electrical Engineering and Computer Science

at the

MASSACHUSETTS INSTITUTE OF TECHNOLOGY

June 2010

Author .....
Department of
Electrical Engineering and Computer Science
May 14, 2010

Certified by .....
George Barbastathis
Associate Professor of Mechanical Engineering
Thesis Supervisor

Accepted by .....
Terry P. Orlando
Chairman, Department Committee on Graduate Theses

Computational Phase Imaging based on Intensity Transport

by

Laura A. Waller

Submitted to the Department of
Electrical Engineering and Computer Science
on May 14, 2010, in partial fulfillment of the
requirements for the degree of
Doctor of Philosophy in Electrical Engineering and Computer Science

Abstract

Light is a wave, having both an amplitude and a phase. However, optical frequencies are too high to allow direct detection of phase; thus, our eyes and cameras see only real values - intensity. Phase carries important information about a wavefront and is often used for visualization of biological samples, density distributions and surface profiles. This thesis develops new methods for imaging phase and amplitude from multi-dimensional intensity measurements. Tomographic phase imaging of diffusion distributions is described for the application of water content measurement in an operating fuel cell. Only two projection angles are used to detect and localize large changes in membrane humidity. Next, several extensions of the Transport of Intensity technique are presented. Higher order axial derivatives are suggested as a method for correcting nonlinearity, thus improving range and accuracy. To deal with noisy images, complex Kalman filtering theory is proposed as a versatile tool for complex-field estimation. These two methods use many defocused images to recover phase and amplitude. The next technique presented is a single-shot quantitative phase imaging method which uses chromatic aberration as the contrast mechanism. Finally, a novel single-shot complex-field technique is presented in the context of a Volume Holographic Microscopy (VHM). All of these techniques are in the realm of computational imaging, whereby the imaging system and post-processing are designed in parallel.

Thesis reader: James Fujimoto, Professor of Electrical Engineering, MIT
Thesis reader: Cardinal Warde, Professor of Electrical Engineering, MIT
Thesis reader: Colin J. R. Sheppard, Professor, Head of Division of Bioengineering, National University of Singapore

Thesis Supervisor: George Barbastathis
Title: Associate Professor of Mechanical Engineering

Acknowledgments

Having been at MIT for $\sim 1/3$ of my life, I will always appreciate having spent the formative years of my education at such a unique and wonderful institution. It is the intelligent, passionate people who make this place unlike any other, and I can only name a few here. First and foremost, I want to thank my advisor, Prof. George Barbastathis, for his guidance, knowledge and mentorship, and for creating a truly academic environment for learning and research. I thank my thesis readers, Prof. James Fujimoto and Prof. Cardinal Warde, for insightful suggestions, and especially Prof. Colin Sheppard, who has always welcomed me into his lab in Singapore to discuss ideas and borrow equipment.

I have learned something from all of my colleagues in the 3D Optical Systems group, and I thank in particular Pepe Dominguez-Caballero, Nick Loomis, Se Baek Oh, Lei Tian and Hanhong Gao for all the whiteboard discussions, and Satoshi Takahashi, Chi Chang, Se Young Yang and Nader Shaar for their 'nano' help. I also thank everyone at my second research home in Singapore - members of CENSAM, BIOSYM and the NUS Bioimaging Lab, especially Shan Shan Kou, my collaborator and friend.

Specific recognition goes to Jungik Kim and Prof. Yang Shao-Horn for fuel cell expertise, Mankei Tsang for the idea and help with Kalman filters, Yuan Luo for use of and help with the VHM system, the MIT Kamm lab and Yongjin Sung for cell samples, Boston Micromachines and Prof. Bifano of BU for use of the deformable mirror array. Furthermore, none of this work would have been possible without funding from the Dupont-MIT Alliance (DMA) and the Singapore-MIT Alliance for Research and Technology (SMART).

Finally, I thank my friends and family for making life fun, particularly Sameera Ponda and my awesome boyfriend, Robin Riedel, who is my best friend and greatest advocate. My parents, Eva and Ted, and my sister Kathleen were collaborators in my first backyard optics experiments and taught me by example the importance of education. After 22 years of school, I am no longer a student, but I will never stop learning.

Contents

List of Figures

List of Tables

Chapter 1

Introduction

Phase is an important component of an optical field that is not accessible directly by a traditional camera. Transparent objects, for example, do not change the amplitude of the light passing through them, but introduce phase delays due to regions of higher optical density (refractive index). Where these phase delays can be measured, previously invisible information about the shape and density of the object can be obtained (see Fig. 1-1). Optical density is related to physical density, so phase images can give distributions of pressure, temperature, humidity, or other material properties [2]. Furthermore, in reflection mode, phase carries information about the topology of a reflective object and can be used for surface profiling.

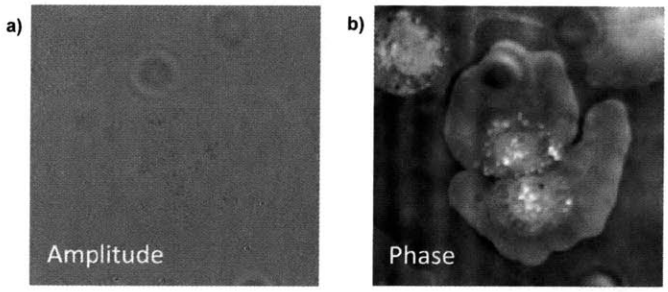

Figure 1-1: Complex-field of a HeLa cell sample. (a) Amplitude transmittance shows no contrast because the cells are transparent. (b) Phase image, obtained by method of Chapter 7, reveals details of the projected density.

When objects are semi-transparent, it becomes important to be able to separate phase effects from those due to absorption. Since only intensity measurements are

made, decoupling phase and amplitude generally requires two measurements for each data point. Techniques which can fully decouple phase from amplitude will be referred to as 'complex-field' imaging techniques, or 'quantitative phase imaging', since they provide a linear map of phase values.

1.1 Phase contrast

The first phase visualization techniques were not quantitative. In the early 1900s, microscopists recognized that a focused image contains no phase information, whereas a slightly defocused image reveals something about the phase of the object [1]. Indeed, an in-focus imaging system has a purely real transfer function and thus no phase contrast. Defocus introduces an imaginary component, converting some phase information into intensity changes [3, 4]. However, the phase to intensity transfer function is generally nonlinear. Thus, a defocused image of a phase object is neither in-focus nor quantitative, yielding only a qualitative description of the object.

Phase contrast microscopy [5] solved the problem of providing in-focus phase contrast, for which Frits Zernike won the Nobel prize in 1953. The method uses a phase mask to shift only the DC term, such that it interferes with higher spatial frequencies. This provides a simple, efficient method for converting phase information to intensity information (see Fig. 1-2), however, is not a quantitative technique.

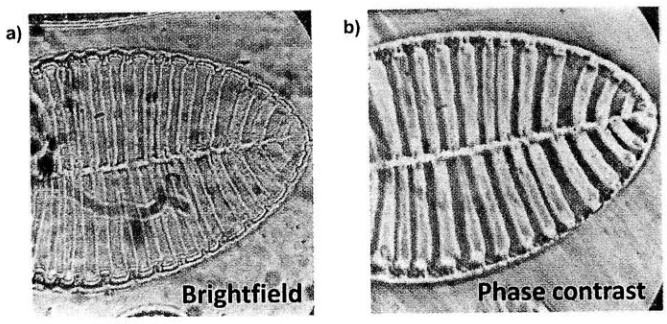

Figure 1-2: Original phase contrast image, by F. Zernike, 1932 [1].

1.2 Interferometric phase imaging techniques

With the invention of the laser, coherent interference techniques for phase retrieval became accessible, allowing extremely sensitive phase measurements (up to $\lambda/100$) [6]. There are many experimental configurations for interferometry, but the main idea is that the phase-delayed object wave $\psi(x,y) = A(x,y)e^{i\phi(x,y)}$, where $A(x,y)$ is amplitude and $\phi(x,y)$ is phase, is coherently added to a known plane wave reference $A_r e^{i\theta}$ and the measured intensity is related to the cosine of the phase difference,

$$\begin{aligned} I(x,y) &= \left|\psi(x,y) + A_r e^{i\theta}\right|^2 \\ &= |A(x,y)|^2 + |A_r|^2 + 2\,|A(x,y)A_r|\,cos(\phi(x,y) - \theta). \end{aligned} \tag{1.1}$$

Again, intensity is a function of both amplitude and phase, so the technique is not quantitative.

1.2.1 Phase-shifting interferometry

Interferometry can become a complex-field technique by phase-shifting the reference beam at least twice by a known small amount (usually $\lambda/2$) and using multiple images to reconstruct the phase distribution [7]. Sequential capture of the images leads to experimental complexities which will be discussed in Chapter 2. Pixellated phase-shift masks use a different method for single-shot phase imaging by shifting every 4^{th} pixel [8, 9].

Since the measurement is related to the cosine of the phase, there will be 2π ambiguities and an unwrapping process is required [10]. A sample interferogram is shown in Fig. 1-3 along with the recovered amplitude map and the wrapped and unwrapped quantitative phase maps. Images were obtained in a Mach-Zehnder interferometer with four phase-shifted images and the unwrapping method proposed by Ghiglia [11]. The phase object is a cubic phase plate from CDM Optics.

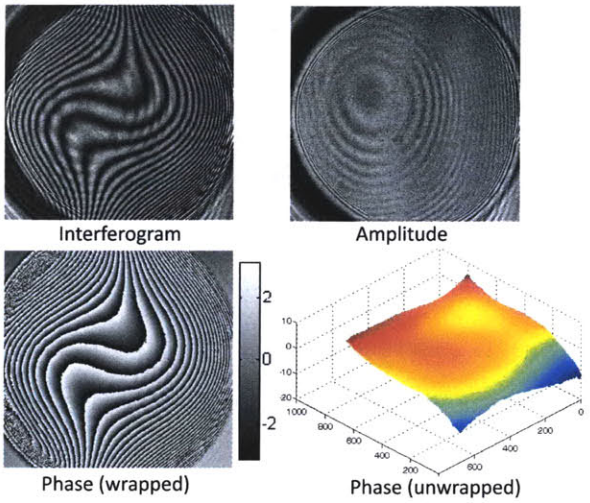

Figure 1-3: Phase-shifting interferometry of a cubic phase plate.

1.2.2 Digital holography

Digital holography (DH) is an interferometric method where light diffracts from an object and the intensity of that diffraction pattern is captured on a camera [12, 13, 14, 15]. Since we know exactly how light propagates, the field can be digitally back-propagated to the focal plane of the object within any linear isotropic medium (or nonlinear medium [16]). When the phase of the diffracted field at the camera is not measured, it must be assumed, leading to the 'twin-image' problem, an artifact caused by a defocused replicate of the object at twice the distance (see Fig. 1-4). Phase-shifting [17] or other phase imaging methods which capture both the amplitude and phase at the camera plane do not suffer from the twin image problem.

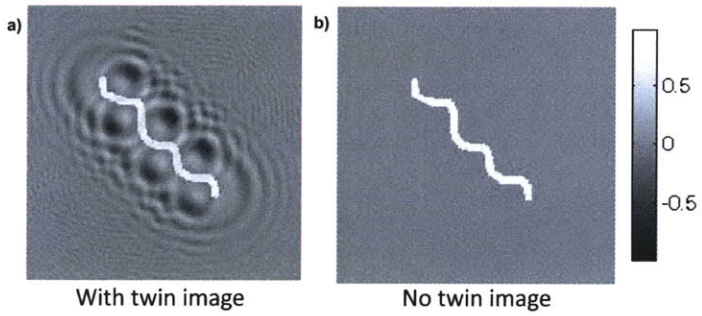

Figure 1-4: Twin image problem. (a) Amplitude reconstruction without phase information at hologram plane, (b) amplitude reconstruction with phase information.

One popular alternative to complex-field DH is the off-axis configuration [18, 19]. By adding a tilt to the reference beam, a spatial carrier frequency modulates the diffracted field and shifts the object and twin image spectrum to different parts of the Fourier plane, such that they can be extracted independently by selecting out the proper section of the hologram's Fourier transform. The major advantage is the capability for single-shot complex-field imaging, at the cost of a large loss in resolution, since only a small number of the total available pixels are used.

The importance of phase in propagation

Light propagation under the Fresnel approximation is a convolution of the field with the quadratic pure-phase factor given by the Fresnel kernel [20],

$$h(x, y; \lambda z) = \frac{e^{i2\pi z/\lambda}}{i\lambda z} \exp\left\{\frac{i\pi}{\lambda z}(x^2 + y^2)\right\}, \tag{1.2}$$

The intensity of the propagated field is:

$$I(x, y; \lambda z) = |\psi(x, y) \otimes h(x, y; \lambda z)|^2 = \left|\mathcal{F}^{-1}\left\{\Psi(u, v)H(u, v; \lambda z)\right\}\right|^2, \tag{1.3}$$

where $\otimes$ denotes convolution, $\mathcal{F}^{-1}$ denotes 2D inverse Fourier transform, u, v are the spatial frequency variables associated with x, y, $\Psi(u, v)$ is the Fourier transform of the field to be propagated, λ is the wavelength of illumination, z is the propagation distance, and $H(u, v; \lambda z) = \mathcal{F}\{h(x, y; \lambda z)\}$ is the Fourier domain Fresnel kernel.

Since propagated intensity is dependent on both amplitude and phase, both are needed to back-propagate the field uniquely. As an example, Fig. 1-5 shows two different complex-fields which produce the same intensity pattern after propagation by the same distance. If one were to measure the phase of the propagated fields, they would not be the same. This emphasizes the benefits of measuring the full complex field in DH experiments.

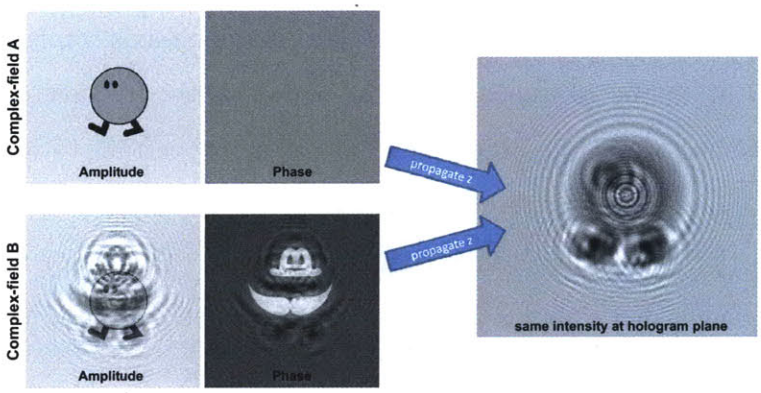

Figure 1-5: Two different complex fields having the same propagated intensity.

1.2.3 Differential interference contrast microscopy

Differential interference contrast (DIC) [21, 22] is a popular technique for phase imaging, due to its high spatial resolution, lack of scanning and high sensitivity to small phase gradients [23, 24]. In a DIC microscope, a Wollaston prism is used to create two sheared wavefronts of orthogonal polarization, $\psi_\delta = A_\delta e^{i(\phi_\delta - \theta)}$ and $\psi_{-\delta} = A_{-\delta} e^{i(\phi_{-\delta} - \theta)}$, then a second prism re-shifts these wavefronts after passing through the object. Thus, the object wave interferes with a shifted version of itself. The intensity in a DIC image is the interference pattern created by the sheared wavefronts:

$$I(x,y) = |A_\delta|^2 + |A_{-\delta}|^2 - 2A_\delta A_{-\delta} cos(\phi_\delta - \phi_{-\delta} + 2\theta), \tag{1.4}$$

where θ is a bias controlled by the prism and δ is the shear. Like interferometry, the intensity measurement from DIC is not quantitative in phase, but can become quantitative with versions of spatial phase-shifting [25, 26, 27], assumption of pure-phase [28], or multiple images at different depths [29]. We include DIC as an interferometric phase imaging technique, although its main application is in partially coherent microscopy.

1.3 Non-interferometric phase imaging techniques

There is great incentive to avoid the complexity and coherence requirements of interferometric techniques in order to obtain useful information directly from brightfield images [30]. Partially coherent illumination enables imaging systems to capture information beyond the coherent diffraction limit [31], avoids the problem of speckle [32], and has potential for use in ambient light, opening up important applications in astronomy and high-resolution microscopy. The problem involves computing phase from a set of intensity measurements taken with a known complex transfer function induced between the images (usually defocus). This leads to a versatile and experimentally simple imaging system where the main burden is on the computation.

1.3.1 Shack-Hartmann sensors

Shack-Hartmann sensors place a lenslet array in front of the camera such that, for each lenslet, the lateral location of the focal spot specifies the direction of the incoming light at that lenslet, which is re-interpreted as wavefront slope [33]. The image can be thought of as a low-resolution discretized Wigner distribution. Phase retrieval can be very accurate and robust to noise if the lenslets are much larger than the camera pixel size, causing a severe loss in spatial resolution since each lenslet provides only one measurement of lateral phase. Shack-Hartmann sensors are popular in wavefront sensing for adaptive correction of atmospheric turbulence, where incoming light is not coherent and spatial resolution is not critical.

1.3.2 Iterative techniques

Some of the earliest algorithms for computing phase from propagated intensity measurements are iterative techniques based on the Gerchberg-Saxton (GS) [34] method. GS uses both an in-focus and Fourier domain image (*i.e.* far field), and alternately bounces between the two domains. At each step, an estimate of the complex-field is updated with measured or a priori information [35, 36, 37, 38]. A more general algorithm, of which GS is a subset, accounts for non-unitary transforms between the

image planes [39], and similar algorithms with Fresnel (instead of Fourier) transforms between the two images have been used for both phase imaging [40, 41] and phase mask design in computer-generated holography (CHG) [42, 43, 44, 45] (see Fig. 1-6). In this case, the amount of defocus between the images will affect the accuracy of the phase retrieval [46] and optimal defocus is object-dependent. Generally, such techniques work better with larger propagation distances, since this provides better diffraction contrast [46, 47].

All of the iterative techniques can be classified as a subset of the more general projection-based algorithms [48], which place no restriction on the transforms used for the optimization, allowing simultaneous enforcement of constraints across multiple domains [49, 50]. Solutions are not provably unique, but are likely to be correct [51], and many tricks exist for reducing the solution space [52]. A priori information can be incorporated and phase-mask design can be guided to a particular class of practical solutions, such as pure-phase [50] or binary phase [45]. In the case of imaging, where there is only one correct solution, one can reduce the solution space by using more than two intensity images (*i.e.* a stack of defocused images) [53, 54] or using phase masks to introduce custom complex transforms between the image planes [55]. Still, defocus remains a popular contrast mechanism, due to its simplicity and the fact that the optimal transfer function is object-dependent. Here, we refer to this entire class of techniques as 'iterative techniques'.

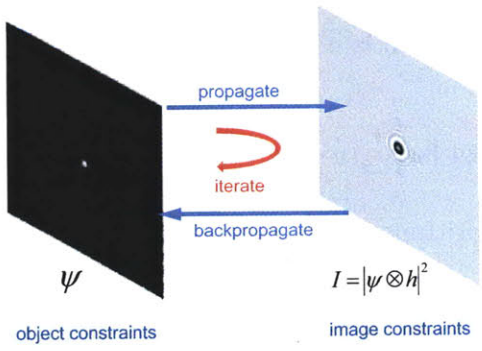

Figure 1-6: Schematic of an iterative technique, with two images in the Fresnel domain. ψ is the complex-field at the first image plane and h is the propagation kernel.

1.3.3 Direct methods

Direct solutions have been proposed to retrieve phase from intensity measurements in 1D [56] or under the assumption of pure-phase [57], small-phase [58, 59] or homogeneous objects [60]. Recursive [61] and single-shot methods [62] trade off spatial resolution for complex information. One direct technique which has found great use is the Transport of Intensity (TIE) technique, described below.

1.3.4 Transport of Intensity

When light passes through a phase object, the wavefront gets delayed and bends the rays, defined to be perpendicular to the wavefront (see Fig. 1-7). If the change in slope of the rays (or, the axial derivative of intensity) can be measured, then the associated phase delay is given by the TIE [63, 64, 65]:

$$\frac{\partial I(x,y)}{\partial z} = \frac{-\lambda}{2\pi}(\nabla_\perp \cdot I(x,y)\nabla_\perp \phi(x,y)), \tag{1.5}$$

where $I(x,y)$ is the intensity in the image plane, λ is the spectrally-weighted mean wavelength of illumination [66] and $\nabla_\perp$ denotes the gradient operator in the lateral dimensions (x,y) only.

TIE imaging is able to produce accurate complex-field reconstructions with partially coherent light [67], right out to the diffraction limit of the imaging system [68] and without the need for unwrapping [69]. The properties and limitations of the TIE method will be discussed in detail in Chapter 4.

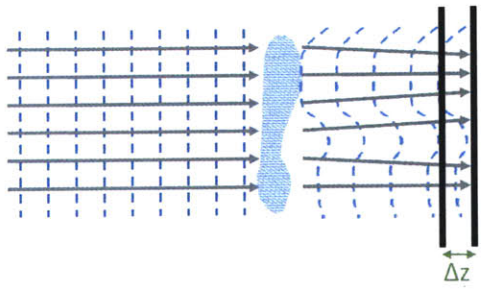

Figure 1-7: A plane wave passing through a phase object. Grey arrows are rays and blue dashed lines are the associated wavefronts.

1.3.5 Estimation theory

Estimation theory provides a framework for recovering complex-field from partial measurements. A maximum likelihood estimation [70] method has been proposed and extended for use with multiple intensity images [71, 72], decreasing the error bounds [73]. The practical application is still iterative, and it can get stuck at local maxima when noise disrupts the images [74, 75]. Regularization of the objective function enables a trade-off between noise and information [75, 76], but the technique does poorly for small defocus between the images [77]. In Chapter 6, a new way of using estimation theory for complex-field imaging is proposed which uses the extended complex Kalman filter to recursively guess the wave-field and separate it from severe noise.

1.4 Computational imaging

All of the complex-field techniques presented above fall under the category of 'computational imaging'. Computational imaging refers to the idea of the computer becoming a part of the imaging system. The goal is not to capture the desired final image directly, but to capture an image or images that can efficiently be processed to recover the desired quantity. Phase imaging techniques are one of the earliest forms of computational imaging. In fact, since phase cannot be measured directly and there is no known optical mapping that converts phase directly to linear intensity, quantitative phase imaging is necessarily a computational imaging technique.

Computational imaging has been named the third revolution in optical sensing, after optical elements and automatic image recording [78]. Over the years, computers have gotten much better, while physical optics still faces many of the challenges it faced in the early days (*e.g.* precision polishing and aberration correction). Computational design of optical elements is still fabrication-limited [79], but automatic image recording allows images to be manipulated at will after capture, enabling the revolution of computational imaging.

The goal is no longer to design an optical system to relay the desired informa-

tion to the camera, but to design a system which optimizes the optical system and post-processing simultaneously. Optical elements can be considered analog signal processing blocks, and it is up to the designer to decide, based on experimental and computational constraints, which processing is best done by the optical system vs. the computer. Unnecessary information need not be captured, as in compressive sensing [80], and multiple images can be used to recover higher-dimensional data that cannot be captured in a 2D plane, as in tomography [81] and phase-space tomography [82]. Even under the constraint of taking a single 2D image, spatial pixels can be traded for information in other dimensions. For example, when a cubic phase mask is inserted in a camera, the entire image appears blurred, but inversion allows one to recover a sharp image with extended depth of focus [83]. Other coded aperture techniques recover depth information [84], allow multiple view angles by inserting a lenslet array [85, 86] or use novel coding of the integration time [87] to capture an image that looks nothing like the object but can be used to gain useful information. Volume holograms [88], which will be discussed in Chapter 8, are particularly useful optical elements for computational imaging, in that they can be designed to filter and multiplex a wide variety of spatial, spectral and angular information.

Much of the work in this thesis describes new methods of computational phase imaging. Illumination, optics and processing are optimized simultaneously to achieve different goals, including in situ imaging, real-time processing and accuracy in the presence of noise.

1.5 Outline of thesis

Chapter 2 introduces phase tomography using phase-shifting interferometry and describes new ways of including a priori information in the inherently ill-posed reconstruction, particularly in the case of diffusion distributions, where useful information can be extracted from very few projections.

Chapter 3 demonstrates the implementation of a specific novel application of interferometric phase tomography which uses just two angles to detect and localize large

changes in water content in a fuel cell membrane while the fuel cell is in operation.

Due to the experimental limitations of interferometric phase imaging, non-interferometric methods for phase imaging are often more suitable. Chapter 4 introduces and discusses the properties of TIE imaging and describes methods for improving the limitations on this technique, which will be the focus of the remaining chapters.

Chapter 5 proposes a modification of TIE imaging that allows more accurate phase results by using multiple defocused images to remove nonlinearity effects. This technique is accurate, computationally efficient and greatly extends the range of the TIE. However, it does not sufficiently address the problem of noise instability. Thus, the next improvement is to use estimation theory to recover the complex field from a noisy data.

Chapter 6 describes the use of an extended complex Kalman filter to recover complex-field from very noisy intensity images. The method is highly computational and requires compression techniques for making it computationally tractable, but offers near-optimal smoothing of data.

From methods that use lots of images and are heavily computational, Chapter 7 moves in the opposite direction, to a phase imaging technique that is single-shot and achieves real-time phase in a standard optical microscope. The technique leverages the inherent chromatic aberrations of the imaging system to obtain at the camera plane a color image that can be processed to obtain quantitative phase (in the absence of color-dependent absorption or material dispersion). The processing is parallelizable and a real-time system has been implemented on a Graphics Processing Unit(GPU).

Chapter 8 presents one final implementation of TIE imaging for use in a volume holographic microscope (VHM). The VHM enables capture of multiple defocused images in a single-shot by using a thick holographic multiplexed filter, and these images are then used to solve for phase via the TIE.

Finally, Chapter 9 states conclusions and future work.

Chapter 2

Complex-field tomography

Computerized tomography (CT) is one of the earliest examples of computational imaging, the principles of which were suggested before computers existed [89]. The method involves recovery of $N+1$ dimensional information from a set of N dimensional projections taken at varying angles. In this chapter, the basics of tomographic imaging are reviewed as a basis for a discussion of complex-field tomography and the error considerations in sequential phase-shifting applications. Finally, a look at sparse angle tomography of diffusion distributions reveals that useful information can be extracted from projection data at very few angles using a priori information.

2.1 Tomography

For simplicity, we introduce the concept of tomography in terms of a purely absorbing semi-transparent 2D object, to be reconstructed from 1D projections under the geometric optics approximation ($\lambda \to 0$)). The object is illuminated by a plane wave with intensity I_0. The intensity of the ray, I, after projection through the object is given by Beer's law [31],

$$I = I_0 exp\left(-\int \alpha(x,y)dl\right), \tag{2.1}$$

where $\alpha(x,y)$ is the absorption coefficient and the line integral is taken along the

length of the ray, l. Assuming parallel ray illumination, the Radon transform [90] describes the projections of $f(x, y)$ in a 2D matrix encoded on the axes (ξ, θ), where $\xi = xcos\theta + ysin\theta$ describes the projection axis variable and θ is the projection angle (see Fig. 2-2 for geometry). The Radon transform $p(\xi, \theta)$ of $f(x, y)$ is,

$$p(\xi, \theta) = \int \int f(x, y)\delta(xcos\theta + ysin\theta - \xi)dxdy. \tag{2.2}$$

Thus, each column of the Radon transform is a projection along a different angle. A sample object and its Radon transform are shown in Fig. 2-1. Since each point on the object traces out a sinusoidal path through the Radon transform, the representation is also called a 'sinogram'.

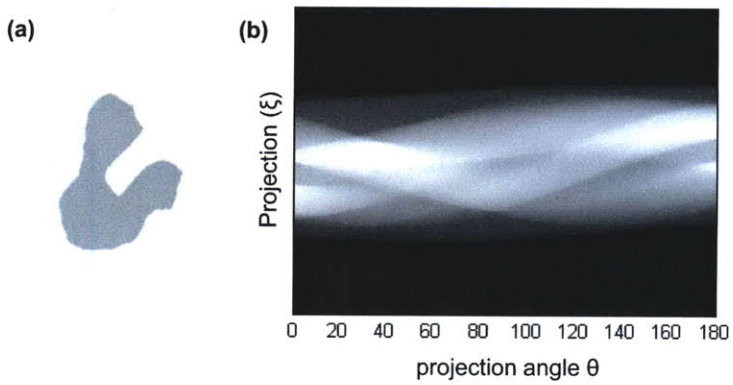

Figure 2-1: The Radon transform. (a) Object density map $f(x, y)$ and (b) its Radon transform.

Once the set of projections has been collected and arranged into its Radon transform, the solution of $f(x, y)$ can be obtained via an inverse Radon transform. The tomographic inversion process is most intuitive in terms of the Projection-slice theorem.

2.1.1 The projection-slice theorem

The Projection-slice theorem states that the 1D Fourier transform of the projection at angle θ is a line in the 2D Fourier transform of the object, perpendicular to the projection ray (see Fig. 2-2). Mathematically, the 1D Fourier transform of the projec-

tion is $P(w,\theta) = \mathcal{F}_{1D}\{p(\xi,\theta)\}$ and it defines a line in the object Fourier transform, $F(u,v)$, given by:

$$P(w,\theta) = F(wcos\theta, wsin\theta), \tag{2.3}$$

an elegant derivation of which is found in Kak [81].

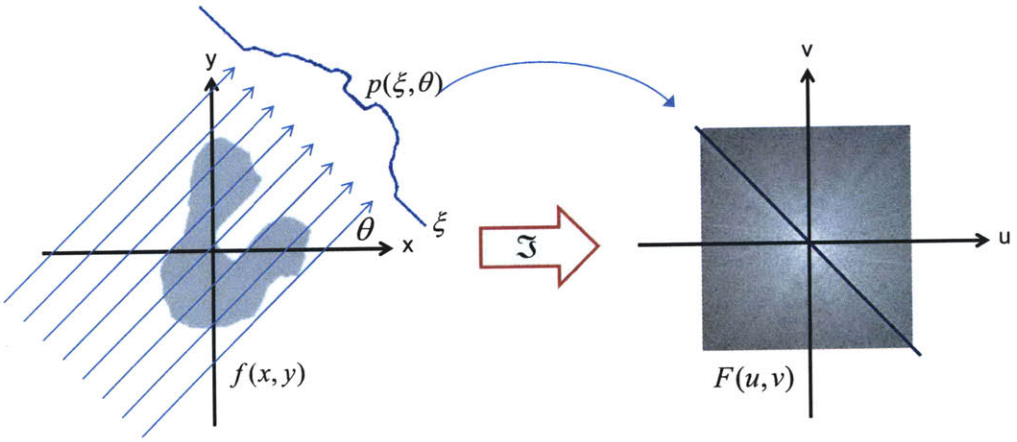

Figure 2-2: The Projection-slice theorem.

2.1.2 Filtered back-projection

Projections at equally spaced angles from 0 to 180 degrees will fill in lines of the Fourier domain reconstruction of $F(u,v)$ in a spoke-wheel pattern, as seen in Fig. 2-3(a), and the desired field $f(x,y)$ is the inverse 2D Fourier transform of $F(u,v)$. However, since it would require an infinite number of angles to fully specify $F(u,v)$, the inversion is inherently ill-posed. Furthermore, the sampling of $F(u,v)$ is non-uniform, with low frequencies being more densely sampled than high frequencies, causing noise instability in the high frequencies. It is for these reasons that the practical inversion of the tomographic problem usually takes the form of a filtered-back-projection algorithm [81], where each projection-slice in the Fourier domain is pre-multiplied by a ramp filter (Ram-Lak) to account for uneven sampling, and some sort of apodization filter to attenuate high frequency noise (see Fig. 2-3b).

Many alternative inversion algorithms exist [91], one of which uses the unique

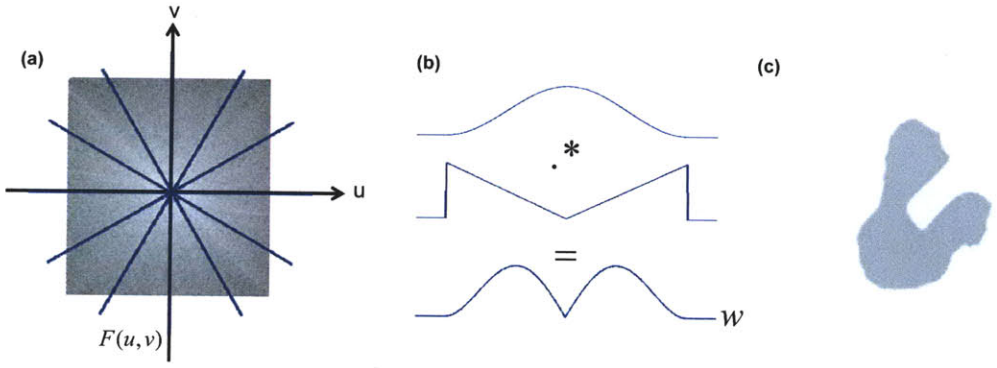

Figure 2-3: Filtered back-projection. (a) Sampling in the Fourier domain by projections, (b) a Hamming window (top) is pixel-wise multiplied by a Ram-Lak filter (middle) to get the Fourier domain projection filter (bottom). (c) Reconstruction using 180 projections.

mathematical properties of the sinogram to interpolate incomplete projection data in the Radon domain by constraining the data to produce a valid sinogram [92, 93]. For example, in the case of sparse binary objects, the sinogram will be a finite superposition of sine waves with varying amplitude and phase according to their radial and angular positions, respectively. Each sinusoid requires only a few data points to specify it, leading to interesting methods in compressive imaging.

2.2 Phase tomography

Tomography has traditionally taken the form of amplitude tomography [94], yet the extension to complex-field tomography is straightforward. In this case, the attenuation constant $\alpha(x, y)$ becomes complex, and separate Radon transforms may be derived independently for the amplitude and phase projections. Phase tomography was first presented in the context of large-scale refractive index fields [2, 95, 96, 97] and later used in microscopy with phase-shifting interferometry [98], TIE [99, 100] or other phase imaging methods [101, 102].

In the case of microscopy, when the object is no longer large compared to the wavelength, scattering effects cannot be ignored. Diffraction tomography is a well-studied and important extension to CT which allows true 3D imaging of scattering

objects [103, 104, 105, 106, 107, 98, 108, 109]. Under the Rytov approximation, the 3D scattering potential can be solved for directly by using intensity diffraction tomography [110, 111, 112], of which CT is a subset [113].

2.2.1 Phase-shifting complex-field tomography

Assume that the phase and amplitude at each projection angle is captured using phase-shifting in a Mach-Zehnder interferometer (see Fig. 2-4).

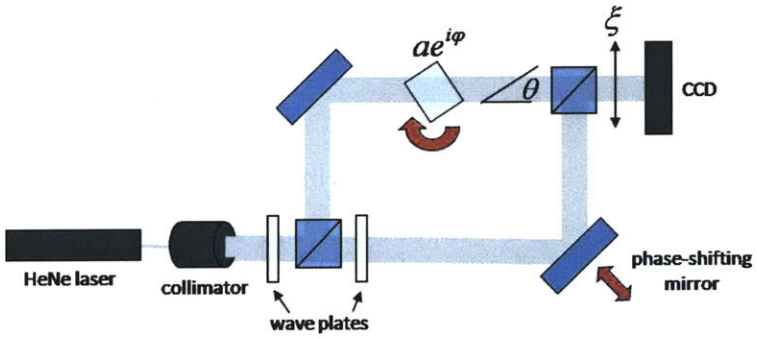

Figure 2-4: Tomographic arrangement in a Mach-Zehnder interferometer.

For simplicity, the analysis is restricted to two-dimensional objects. The complex object is denoted as $a(x,y)e^{i\phi(x,y)}$, where $a(x,y)$ is the amplitude distribution and $\phi(x,y)$ is the phase distribution. A phase-shifting projection set (PS^2) is defined as the set of four phase-shifting sinogram measurements:

$$\begin{aligned} I_0(\theta,\xi) &= |1 + A(\theta,\xi)e^{i\Phi(\theta,\xi)}|^2 \\ I_1(\theta,\xi) &= |e^{\pi/2} + A(\theta,\xi)e^{i\Phi(\theta,\xi)}|^2 \\ I_2(\theta,\xi) &= |e^{\pi} + A(\theta,\xi)e^{i\Phi(\theta,\xi)}|^2 \\ I_3(\theta,\xi) &= |e^{3\pi/2} + A(\theta,\xi)e^{i\Phi(\theta,\xi)}|^2, \end{aligned} \tag{2.4}$$

where $A(\theta,\xi)$ and $\Phi(\theta,\xi)$ are the integrals of object absorption and phase delay, respectively, along the projection angle θ, ξ is the projection index and I_0, I_1, I_2,

I_3 are the measurements with phase shifts equal to 0, $\pi/2$, π, and $3\pi/2$ radians, respectively. The reconstruction proceeds as follows: First, for each PS^2 we obtain the quantity [114]

$$\tan \hat{\Phi}(\theta, \xi) = \frac{I_1(\theta, \xi) - I_3(\theta, \xi)}{I_0(\theta, \xi) - I_2(\theta, \xi)}. \tag{2.5}$$

More phase-shifted interferograms may be used with an n-point reconstruction algorithm where available [7]. Phase is solved for and unwrapped at each projection, before applying the inverse Radon transform algorithm to $\hat{\Phi}(\theta, \xi)$, and recovering the estimate of the object phase distribution. The mean intensity of PS^2 gives $|A(\theta, \xi)|^2$ to get an estimate of amplitude.

Two-dimensional phase unwrapping is an important research area, as noise and phase-shifting error cause the unwrapped solution to become ill-posed [10]. After studying the merits and effectiveness of varying techniques, we chose the Preconditioned Conjugate Gradient solution [11] with Discrete Cosine Transform initial condition [115] to unwrap the phase and obtain the unwrapped phase.

2.2.2 Experimental results

Using the setup of Fig. 2-4, and extending the mathematical description to 3D, we experimentally reconstruct complex volumetric objects by taking 2D projection sets at 36 equally-spaced angles. Inter-frame phase-shifts were induced by moving a mirror linearly on a piezo-controlled stage, and the actual phase shifts were determined by an inter-frame intensity correlation method [116]. The object was rotated in 5 degree steps from 0-180 degrees, taking a four-frame projection set at each angle. In these experiments, the objects were immersed in index-matching oil, to reduce refractive ray-bending and increase fringe spacing (to avoid aliasing at the CCD). Phase-shifting error is a major source of inaccuracy; hence, a study of the effects of this type of error on tomographic reconstructions follows.

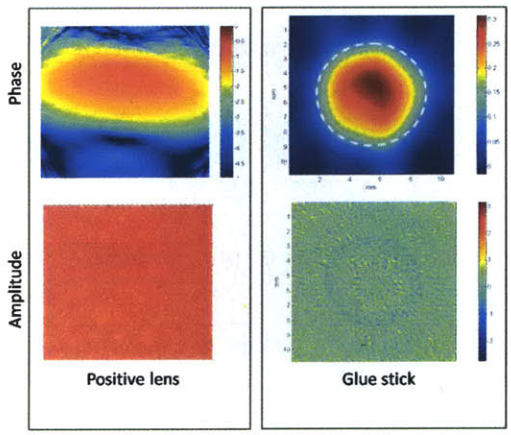

Figure 2-5: Sample 2D cross-sections of 3D complex-field objects immersed in index-matching fluid.

2.2.3 Error analysis of phase-shifting tomography

The effect of phase-shifting error for 2D interferometry of phase-only objects has been well-analyzed in the literature [7, 117, 118]. Here, we extend these studies to show how the effects of phase-shifting error propagate to the tomographic phase and amplitude reconstruction [119].

Phase-shifting alone theoretically gives perfect reconstruction. Tomography, however, has inherent error due to finite data in the projection-slice theorem [81]. The propagation of phase-shifting errors to the amplitude reconstruction and further, to the tomographic reconstruction, is not intuitive, since each projection contains error, which is then input to the Radon transform.

We consider five types of error (see Table 2.1). Type I, constant phase error, is a constant phase δ_c added to each phase-shift. Type II represents a miscalibration of the phase-shifter, resulting in each phase-shift between successive measurements deviating from the prescribed value of $\pi/2$ by a fixed amount δ_l. Type III simulates normally distributed statistical error in the phase-shifter. Types IV, V simulate error due to mirror tilt during phase-shifting for one or all three phase-shifts, respectively. These are the commonly encountered error types when using a piezo-controlled mirror to phase-shift, however may also apply to other phase-shifting methods including

Ideal shift	Type I Constant error	Type II Miscalibration	Type III Statistical	Type IV Tilt	Type V Statistical tilt
0	0	0	0	0	0
$\pi/2$	$\pi/2+\delta_c$	$\pi/2+\delta_1$	$\pi/2+\delta_1$	$\pi/2+\alpha x$	$\pi/2+\alpha_1 x$
π	$\pi+\delta_c$	$\pi+2\delta_1$	$\pi+\delta_2$	π	$\pi+\alpha_2 x$
$3\pi/2$	$3\pi/2+\delta_c$	$3\pi/2+3\delta_1$	$3\pi/2+\delta_3$	$3\pi/2$	$3\pi/2+\alpha_3 x$

Table 2.1: Types of phase-shifting error

Electro-Optic Modulators, diffraction gratings, and rotating half-wave plates.

Figure 2-6 plots the mean-squared relative amplitude and phase error for Type I-V phase-shifting errors, along with the tomographic reconstruction error map of a null object. Statistics were performed across an ensemble of 40 randomly generated complex phantom objects, using the filtered back-projection algorithm with a Ram-Lak interpolation filter, number of pixels $N = 128$ and number of projections $N_{proj} = 180$.

Type I error is the mildest type, as can be seen in Figure 2-6(a), but in practice it is not commonly encountered. As expected, the phase error is concentrated near the outer edges, where the inverse radon transform is more sparsely sampled. Type II(miscalibration) has the same effect, only with twice as much sensitivity (Figure 2-6(b)). Type III phase-shift errors are unavoidable and can be modeled as zero-mean normally distributed random variables $\delta_1, \delta_2, \delta_3$ added to the phase shifts (Fig. 2-6(c)). For comparison, a standard commercial piezo-stage mirror positioner, with 50nm positional accuracy, gives a standard deviation $\sigma(\delta) = 0.08$ waves error at 632.8nm.

If the phase-shifting mirror is tilted with respect to the object beam, a linear phase variation across x results for all phase shifts, as modeled in Type IV error (Fig. 2-6d). The difference in tilt between one phase-shifted interferogram and its successors causes an obvious radially varying phase error in the tomographic reconstruction (see Fig. 2-6(d), error map) which could be erroneously interpreted as measured data. Finally, in Type V error, the tilt error coefficients $\alpha_1, \alpha_2, \alpha_3$ are normally distributed

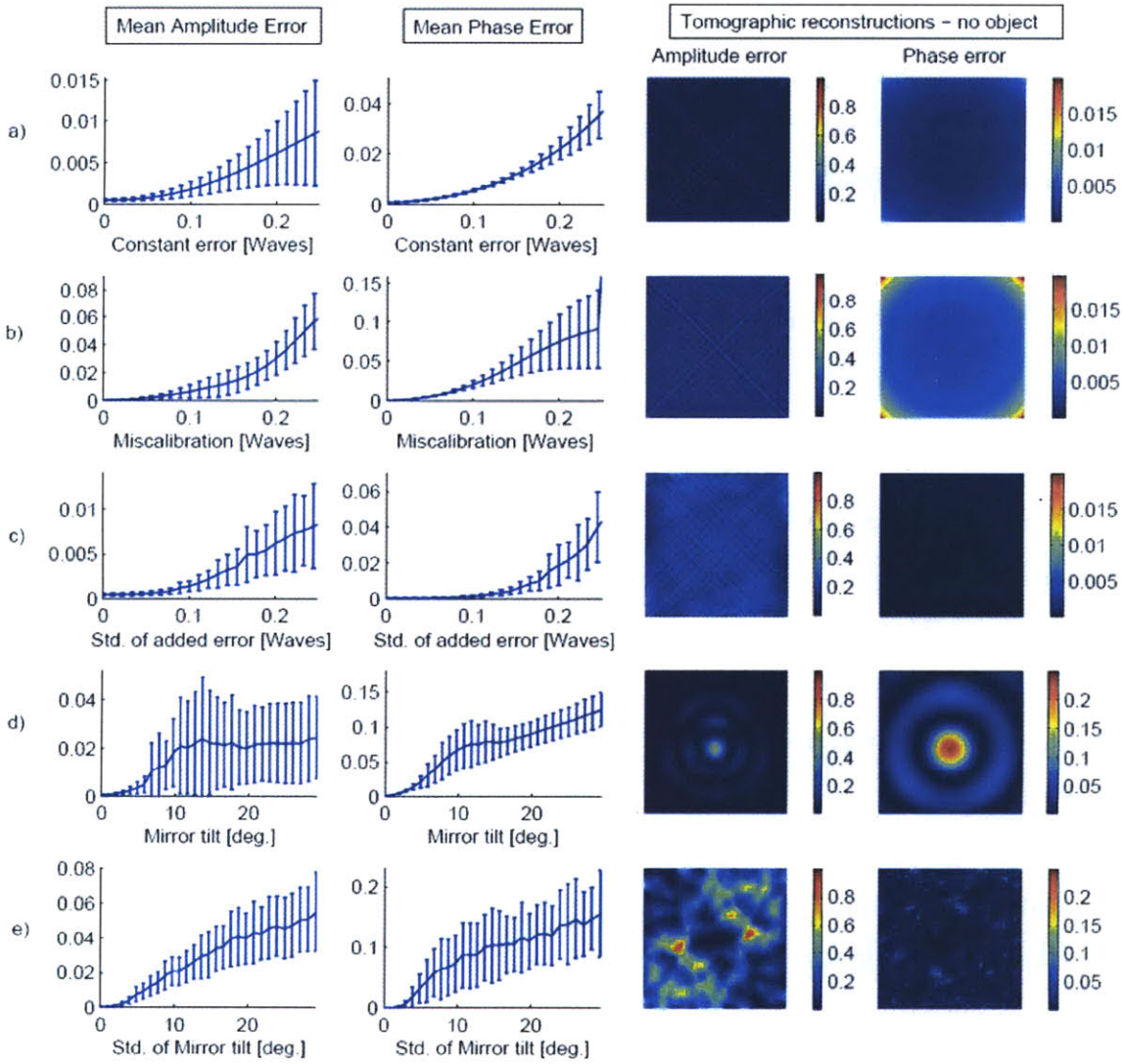

Figure 2-6: Left: Tomographic error due to phase-shifting. Right: Error maps for reconstruction of null object (phase in radians). Error bars indicate standard deviation. a) Type I, b) Type II, c) Type III, d) Type IV, e) Type V error.

random variables. Statistically varying tilt can cause greater phase errors (Fig. 2-6(e)). However, the error distribution is more uniform when compared to Type IV errors.

Generally, systematic or miscalibration errors (Types I, II, and IV) result in non-uniform distribution of the error across the object, whereas the opposite is true for random errors (Types III and V). As in any tomographic system, the error will be heavily object-dependent; however, these models may help in digitally detecting and removing unwanted error.

2.3 Sparse-angle tomography of diffusion processes

In the previous section, errors were explored for tomographic reconstructions assuming many projection angles. Practically, it is often impossible to get projection data simultaneously for many angles. Thus, we look now at the important case of sparse-angle tomography, where very few angles of projection data are available. A general rule for managing interpolation error and sampling sufficiently the Cartesian grid of $F(u, v)$ is that the number of samples in each projection, N, should be similar to the number of projections, N_{proj} [81]. Using a 1200 pixel camera would imply that we should measure the phase at 1200 evenly spaced projection angles in order to get a good reconstruction over the whole frequency range. We show here that the inherent spatial and temporal smoothness of the diffusion processes allows us to decrease the number of required projection angles in tomography of diffusion processes.

As mentioned in Sec. 2.1.2, when more angles are added to the reconstruction, low frequencies near the origin become oversampled, while higher frequencies are more sparsely sampled. If the object contains only low frequency information, the required number of projection angles (for a given resolution) should decrease. Limited angle tomography, where projections from a contiguous range of angles is missing due to occlusions, has been studied [120, 121] and is generally non-unique [122, 123, 124], but the case of sparse anglular sampling of smooth data is not well-studied.

The Kaiser filter has been suggested as a basis for reconstructing smooth distribu-

tions [125] and is applied here in the Fourier Domain. The Kaiser window is defined as [126],

$$K(u) = \frac{I_0(\beta(C^2 - u^2)^{0.5})}{I_0(\beta)}, \tag{2.6}$$

with I_0 being the modified Bessel function of the first kind, order 0, C the cutoff frequency for the window, and β controls the spatial influence of the basis functions. A Kaiser function with large β tends to a Gaussian curve in frequency and object spaces, and the Gaussian function is a solution to the diffusion equation. While a Gaussian curve technically has infinite bandwidth, we assume that it is effectively bandlimited by the noise floor of the camera. Thus, the expected effective bandwidth covers only a small portion of the available bandwidth determined by the camera. Happily, this low frequency information is also the area in frequency space which has the least interpolation error due to the restricted number of angles. By redesigning the filter in the back-projection method to restrict the solutions to the class that we are looking for, we eliminate the higher frequency information that would normally corrupt the image. It should also be noted that this processing step serves also as a data compression step.

2.3.1 Projections of diffusion distributions

The diffusion equation is a partial differential equation (PDE) that shows up in many important physical and mathematical situations. It describes the statistics of random walk processes such as heat conduction.

We start with the linear 2D diffusion equation:

$$\frac{\partial f(x,y,t)}{\partial t} = D\nabla_{\perp}^2 f(x,y,t), \tag{2.7}$$

where $f(x,y,t)$ is the diffusion field (for example, temperature or concentration) over space and time and D is the diffusion coefficient (or thermal conductivity in the case of heat conduction).

Equation 2.7 is separable in (x,y,t) and so it can be split into uncoupled dimen-

sionally independent equations in x, y and t (*i.e.* $f(x,y,t) = X(x) \cdot Y(y) \cdot T(t)$) [127].

One consequence of this separability is that the projection of a 2D diffusion profile along any angle is a 1D diffusion profile.

Take the 2D Gaussian function, a fundamental solution to Eq. 2.7,

$$\widehat{g}(x,y;\sigma) = \frac{1}{2\pi\sigma^2} e^{-\frac{x^2+y^2}{2\sigma^2}} \tag{2.8}$$

Taking a projection along x,

$$p(y) = \frac{1}{2\pi\sigma^2} e^{-\frac{y^2}{2\sigma^2}} \int e^{-\frac{x^2}{2\sigma^2}} dx. \tag{2.9}$$

A change of variables $\widetilde{x} = \frac{x}{\sqrt{2}\sigma}$ leads to,

$$p(y) \;\; = \frac{\sigma\sqrt{2}}{2\pi\sigma^2} e^{-\frac{y^2}{2\sigma^2}} \left(\int e^{-\widetilde{x}^2} d\widetilde{x} \right) \;\; = \frac{1}{\sqrt{2\pi}\sigma} e^{-\frac{y^2}{2\sigma^2}}, \tag{2.10}$$

which has the form of a 1D Gaussian curve. Similarly, the projection of a sum of 2D Gaussians is a sum of 1D Gaussians and any 2D diffusion solution of the Gaussian form will have projections that are 1D diffusion solutions.

Chapter 3

Two angle interferometric phase tomography of fuel cell membranes

3.1 Introduction

As an application of complex-field tomography, we apply a modified phase tomography system for the purpose of water content monitoring in fuel cell systems [128]. Fuel cells are compact, reliable sources of clean energy. A PEM fuel cell consists of current collectors, an anode and a cathode, separated by a thin membrane. Hydrogen gas and oxygen are supplied to the anode and cathode sides, respectively, through serpentine gas flow channels, shown in Figure 3-1. With the help of a Platinum catalyst, the hydrogen splits into positive ions, which pass through the membrane, and electrons, which go through the circuit to supply the load. On the other side, the positive and negative ions recombine with supplied oxygen to form water.

The performance and breakdown of PEM fuel cell systems is critically dependent on the local water content in the membrane [129, 130]. High humidity increases the fuel cell efficiency and prevents failure [131, 132]. However, excessive humidity causes condensed droplets to form in the flow channels, locally blocking the reaction [133, 134, 135]. In order to design more durable and efficient fuel cell systems, it is desired to detect water content changes while the fuel cell is in operation [136]. Furthermore, real-time monitoring of the local water content could be used as input to a feedback

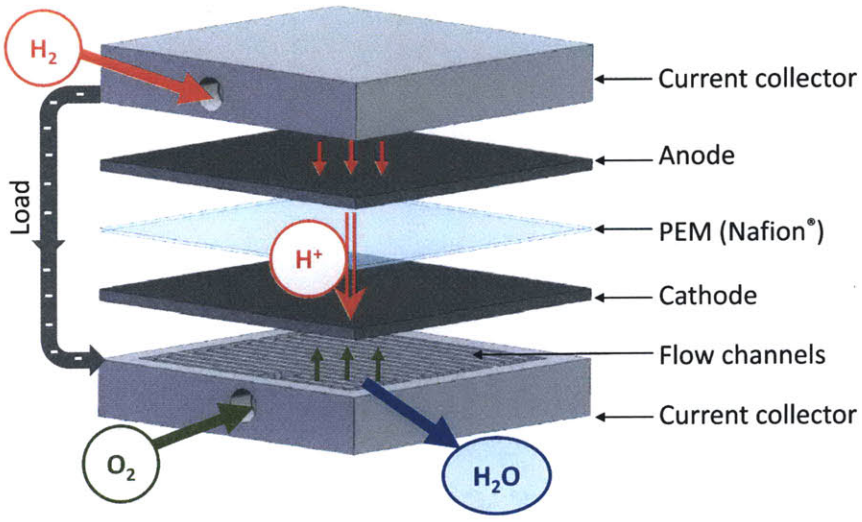

Figure 3-1: Schematic of a PEM fuel cell system.

control system which would maintain ideal humidity across the entire membrane during operation.

Several groups have developed methods of imaging water content in fuel cell systems, using Magnetic Resonance Imaging [137, 138], Neutron imaging [139, 140, 141, 142], X-ray imaging [143], transparent windows [144, 145] and optical fluorescence spectroscopy [146]. However, all of these methods are either invasive, expensive or have poor spatial or temporal resolution. St.Pierre [136] compares many methods and reviews their limitations. The end goal is to develop a real-time water imaging method which is inexpensive, non-invasive, and has good spatial and temporal resolution [147].

We develop here a system using interferometric phase tomography for 2D in situ monitoring of the water content in the membrane from 1D projection data with high spatial and temporal resolution. The refractive index is assumed to be directly proportional to water content [148, 149] and the membrane is more than 95% optically clear. Interferometry has often been used for concentration gradient measurements of transparent liquid solutions [150] and we have shown previously that it is also suitable for measuring water concentration gradients in solid Nafion® PEM membranes [151, 152]. In these experiments, light was shone through the flat face of the membrane;

thus, water content changes cause small changes in optical path length (OPL). For in situ measurements, light cannot be shone through the face of the membrane, as the surrounding current collectors are opaque (see Fig. 3-1). Thus, we shine the light through the length of the membrane, 'in-plane'. Preliminary results from our in-plane configuration were demonstrated in [153]. Nafion®'s refractive index is very close to that of water, and it is sometimes used for index-matching in biofilms [154]. This means that the index changes due to humidity are very small ($\sim 10^{-4}/\%RH$); however, in the in-plane configuration, the OPL is longer by orders of magnitude than in the through-plane case, causing large phase gradients and serious problems with aliasing in the phase unwrapping process, as well as increased internal absorption, refraction and scattering.

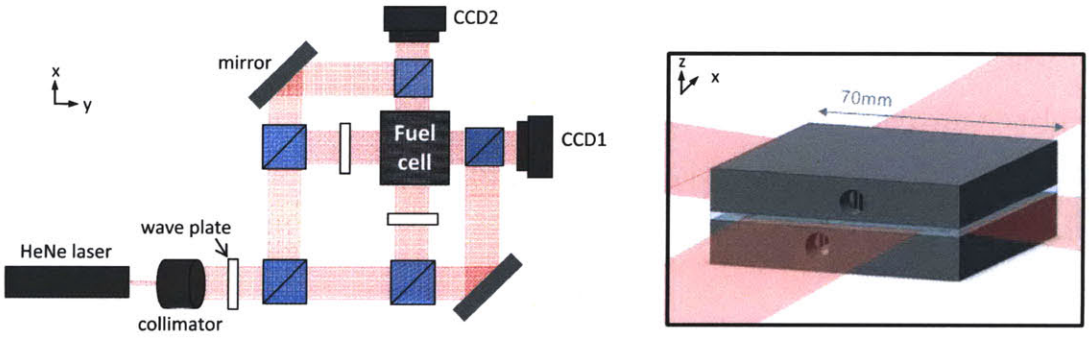

Figure 3-2: Double Mach-Zehnder interferometer configuration. Waveplates are used to adjust the relative intensities of the reference and object arms.

The extreme sensitivity of interferometry prevents its widespread implementation for large phase change measurements. We show here how these problems might be avoided for many diffusion distributions by unwrapping the phase temporally instead of spatially. Furthermore, we use two-angle tomography to reconstruct the in-plane water content from projections. We are limited in physical space to only imaging two projections at once, and the desire for temporally resolved reconstructions makes rotation of the object impractical. This presents a new and interesting problem in the reconstruction of tomography data from a severely limited number of projections. Generally, two angles will not be enough to recover accurately a 2D distribution [81]. However, by taking advantage of the inherently smooth and well-known diffusion

process of the water in time and space, we are able to modify the backprojection filter with this a priori information in such a way as to recover useful 2D water content data.

3.2 Optical system

The PEM fuel cell system sandwiches a 3cm x 3cm x 125μm semi-transparent membrane between two 7cm x 7cm x 2cm opaque current collectors with flow channels etched into them (see Figure 3-1). Light is shone in-plane at two orthogonal angles using the custom designed double Mach-Zehnder interferometer (Figure 3-2). We model the fuel cell as a thick slit with a complex transmission function, due to line integrals of absorption and refractive index through the membrane (see Figure 3-3). For each angle, we record the interference between the diffracted field from the slit and a plane wave reference. Figure 3-4 shows a sample interferogram and amplitude-only image. We then reconstruct via our modified inverse Radon transform, as described in Section 3.5.

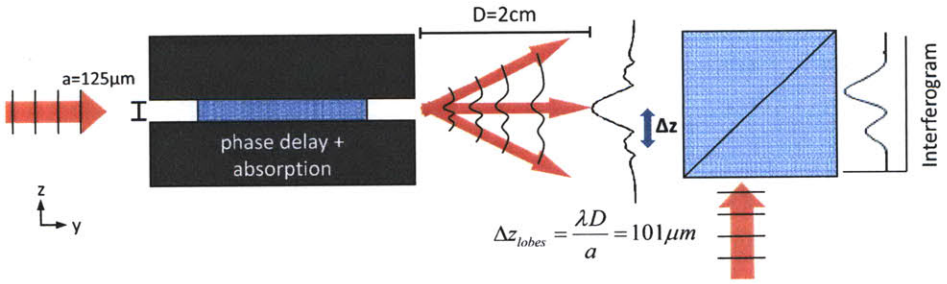

Figure 3-3: Optical model of light in system.

In this system, internal refraction, absorption and scatter are assumed small and will be a source of error. The absorbing electrodes of the fuel cell prevent higher order modes from passing through, leaving only the DC term; thus, waveguiding may be ignored. The main source of error in our measurements comes from the external scatter that occurs at the input and output edges of the membrane, due

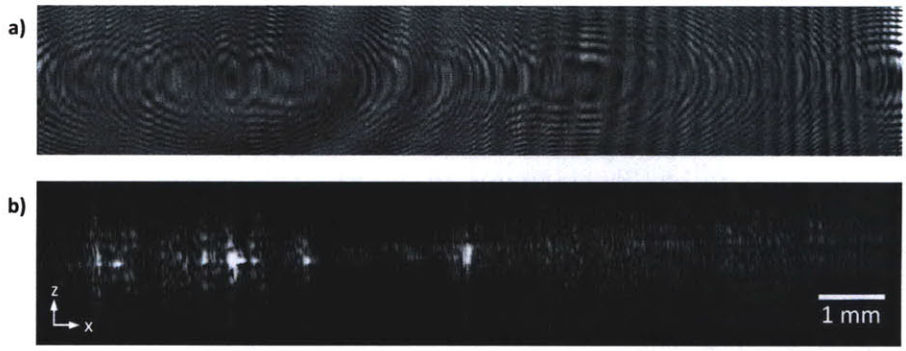

Figure 3-4: In-plane images a) interferogram and b) amplitude only.

to rough edges and striations created when cutting the membrane (see Figure 3-5(a-b)). In this experiment, the rough edges were polished with 12,000 grit sandpaper to make them optically smooth. The reduction in roughness and edge scatter can be seen in Figure 3-5(c-d). This polishing step greatly improves the contrast of the interferograms and reduces information crosstalk in the lateral direction, improving the effective spatial resolution of the system.

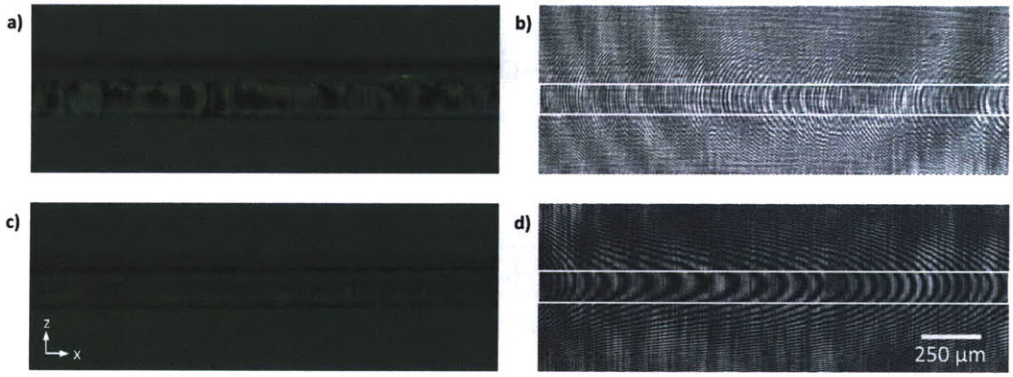

Figure 3-5: Effect of membrane edge polishing. a) Unpolished edge, b) interferogram with unpolished membrane, c) polished edge, d) interferogram with polished membrane.

Diffraction of the object beam at the slit created by the fuel cell electrodes will cause reduced signal intensity at the interferogram, as well as crosstalk between the horizontal pixels, which reduces resolution. The effect is predictable and reversible, using digital holographic (DH) techniques to numerically backpropagate the field at the camera to the slit. Figure 3-6 shows one such solution, using an iterative

Gerchberg-Saxton-Fienup type algorithm in the Fresnel domain [36]. However, DH techniques require large data sets, which become expensive at the fast frame rates we desire and suffer from numerical error and large computation complexity. Thus, we simply mitigate diffractive spreading by moving the camera as close to the slit as possible and assuming a smooth phase distribution. This method and assumption work well in practice in our system.

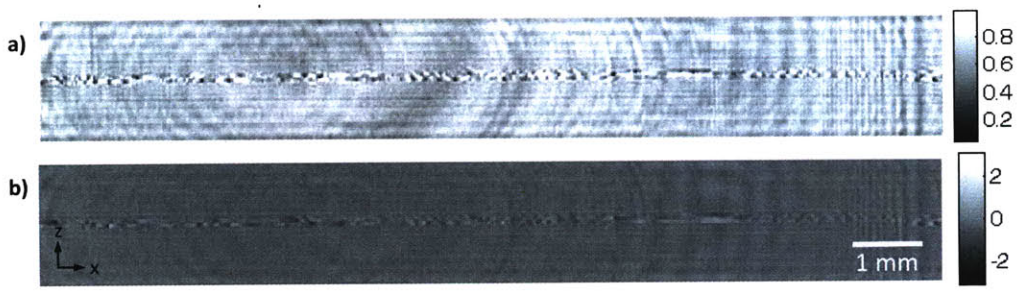

Figure 3-6: Backpropagated solution using Gerchberg-Saxton-Fienup type iterative method in the Fresnel domain with 50 iterations. (a) Amplitude and (b) phase.

3.3 Sampling diffusion-driven distributions

The intensity at the detector plane for a projection across y, is given by:

$$I(x,t) = I_r + I_o(x,t) + 2\sqrt{I_r I_o(x,t)}\cos\left(\frac{2\pi}{\lambda}\int_Y \Delta n(x,y,t)dy\right) \tag{3.1}$$

where I_r is the reference beam intensity (assumed to be uniform), $I_o(x,t)$ is the object beam, $\lambda = 632.8nm$ is the HeNe laser wavelength, Y is the membrane length in the y direction, and $\Delta n(x,y,t) = \frac{\partial n}{\partial \Lambda}\Delta\Lambda(x,y,t)$ is the refractive index in the plane of the membrane, where Λ is the water content of the membrane. Water content is defined as the ratio of water molecules to Nafion® molecules, where $\Lambda_{dry} \approx 2$ and $\Lambda_{wet} \approx 20$. The expression for the second projection $I(y,t)$ is analogous. The measured phase $\phi_x(x,t)$ which wraps every 2π is

$$\phi_x(x,t) = \frac{2\pi}{\lambda}\int_Y \frac{\partial n}{\partial \Lambda}\Delta\Lambda(x,y,t)dy. \tag{3.2}$$

After obtaining two data sets of interferogram projections over time, our reconstruction algorithm goes as follows. For each pixel along x, variations in water content over time appear as changes in frequency of intensity oscillations (Figure 3-7(a)). Faster oscillations indicate larger changes in water content. A simple peak and valley detection algorithm is applied to the intensity vs time data, then the phase is cumulatively integrated across time, adding π for each subsequent peak or valley detected. This unwrapped phase data is then interpolated and multiplied by the known constant, $\frac{\partial n}{\partial \Lambda}$, as measured in previous literature [148, 149], to convert it to water content (Figure 3-7(b)).

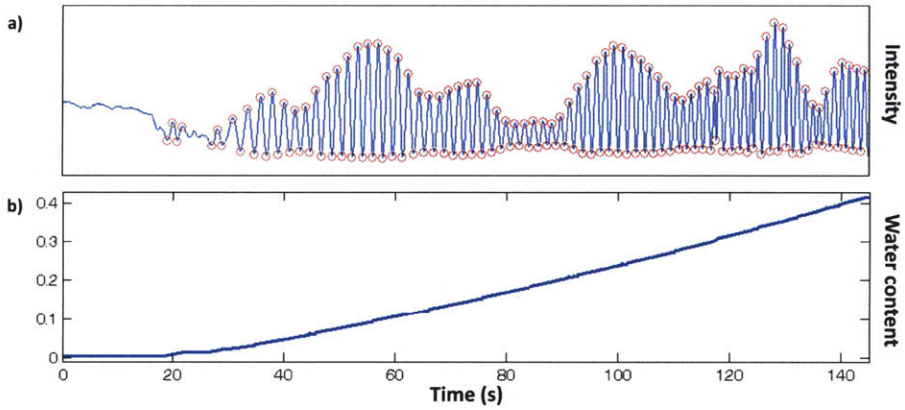

Figure 3-7: Unwrapping intensity variations. (a) Intensity vs time for one pixel, while humidifying. Circles indicate detected peaks and valleys. (b) Water content change vs time after phase unwrapping and conversion.

Usually, phase unwrapping is done in the spatial domain. Algorithms attempt to integrate the cosine of the phase, as measured, over the entire domain, either in 1D or 2D. Any noise or phase discontinuity makes the inversion ill-posed, and various algorithms have been developed to best approximate the true phase [10]. All of these methods, however, carry the restriction that the phase difference between two adjacent pixels must not exceed π in order to avoid aliasing in the unwrapping process. This smoothness restriction is much more difficult to meet when taking a phase projection through a long OPL, as here, or a large phase change. To avoid aliasing in diffusion interferometry, we find that it is much easier to use temporal rather than spatial unwrapping of the phase.

Given that water can only diffuse into and through the membrane, the water content distribution must be a solution to the diffusion equation,

$$\frac{\partial \Lambda}{\partial t} = D\frac{\partial^2 \Lambda}{\partial x^2}. \tag{3.3}$$

Assuming a linear diffusion coefficient, D, the change in water content over x due to a step variation is

$$\frac{\partial \Lambda}{\partial x} = (\Lambda_f - \Lambda_i)\frac{\partial}{\partial x}\left[\text{erfc}\left(\frac{x}{\sqrt{4Dt}}\right)\right]. \tag{3.4}$$

where Λ_i and Λ_f are the initial and final water content in the membrane, respectively. Using this solution, we require that the phase difference between pixels be less than π to meet Nyquist sampling conditions, and substitute known values of our system, to get the minimum spatial sampling:

$$\Delta x_{\text{min}} = \left(\frac{\partial \Lambda}{\partial x_{\text{max}}}\right)\left(\frac{\partial \phi}{\partial \Lambda}\right)\left(\frac{\text{sample}}{\pi}\right) = \frac{6 \text{ samples}}{\mu m} \tag{3.5}$$

Therefore, to avoid aliasing, we must use a camera with $0.16\mu m$ or smaller pixel pitch, which is not possible. On the other hand, the temporal derivative of water content in a diffusion profile is:

$$\frac{\partial \Lambda}{\partial t} = \left(\frac{\partial \Lambda}{\partial x}\right)\left(\frac{x}{2t}\right) \tag{3.6}$$

which leads to a minimum temporal sampling:

$$\Delta t_{\text{min}} = \left(\frac{\partial \Lambda}{\partial t_{\text{max}}}\right)\left(\frac{\partial \phi}{\partial \Lambda}\right)\left(\frac{\text{sample}}{\pi}\right) = \frac{352 \text{ samples}}{\text{sec}} \tag{3.7}$$

It is easy to find inexpensive cameras or line sensors achieving frame rates above 352 fps. Line sensors with speeds up to 40MHz are available, allowing even faster and larger phase changes to be imaged. Temporal unwrapping will give us valid reconstructions, where spatial unwrapping would not.

3.4 Temporal phase unwrapping

One type of temporal phase unwrapping was proposed by Huntley and Saldner [155] in terms of fringe projection profiling. They took many interferograms while shifting the fringe pitch, then unwrapped each pixel independently of the others, in order to reconstruct a single 2D unwrapped phase image without reverting to complicated 2D phase unwrapping techniques [10]. In our approach to temporal phase unwrapping, phase changes are not actively induced in the reference beam. Rather, the phase changes are precisely what we are trying to measure from the object beam. Thus, we essentially perform a differential phase measurement.

3.5 Two angle tomography

Once the temporally unwrapped phase is computed for each projection set, yielding the data sets $\phi_x(x,t)$ and $\phi_y(y,t)$, the two projection sets are then used to tomographically reconstruct the phase at each time sample. A naive application of the inverse Radon transform will yield useless results due to the huge amount of missing information that must be interpolated by the tomographic algorithm. As in Sec. 2.3, the inherent spatial and temporal smoothness of the water diffusion process allows us to drastically decrease the number of required projection angles while still accurately detecting and localizing water content changes. In the extreme case of only two projection angles, where we collect $2N$ data points and try to reconstruct an N^2 image, we expect only the lowest frequency data to be properly reconstructed. With only two angles, there is no need for a ramp interpolation filter, and we simply place the two projections in the center row and column of the Fourier domain reconstruction, averaging the DC term,

$$\Phi(u \neq 0, 0, t) = \mathcal{F}\{\phi_x(x,t)\}K(u);$$
$$\Phi(0, v \neq 0, t) = \mathcal{F}\{\phi_y(y,t)\}K(v);$$

$$\Phi(0,0,t) = (\mathcal{F}\{\phi_y(0,t)\} + \mathcal{F}\{\phi_y(0,t)\})/2; \tag{3.8}$$

where Φ is the 2D Fourier transform of the phase reconstruction, with spatial frequency variables u and v, $\mathcal{F}$ denotes a 1D Fourier transform, and $K(u)$ is the Kaiser window, defined in Sec. 2.3. The C parameter is set here at the maximum frequency expected from diffusion of water into Nafion®, given that the water must diffuse through half of the thickness of the membrane before a measurement is taken. A fairly large β value of 5 was chosen to match the spreading of water from a point, based on the known diffusion coefficient.

3.6 Experimental results

A simple test object was built, consisting of two $15mm$ x $15mm$ aluminum plates sandwiching a Nafion® membrane of the same dimensions. The top aluminum plate has a $2mm$ radius hole drilled into it. A drop of water was placed in this hole, and the 1D interferogram data were collected and processed from both cameras. Six frames from the $500fps$ 2D experimental reconstruction video are shown in Figure 3-8, with a white circle indicating the hole position. As expected, water content originates within the hole, then diffuses outward into the surrounding regions. The positional accuracy of the water drop centroid is better than 1mm throughout the experiment's duration. The reconstruction has visible 't' shaped artifacts, due to the two angles used. If only large changes in water content need be detected, such as those which occur when a water drop forms in the flow channel, then a simple threshold process may be applied to reduce data. Such a modification would be useful in real-time feedback control of the membrane humidity, where we do not require high resolution images, but rather simple detection and 2D position of changes.

Next, the same system was used to monitor water content in-situ in a real fuel cell system. For this experiment, the water was introduced by flowing humidified air through the flow channels. A finite element (FEM) simulation of the expected

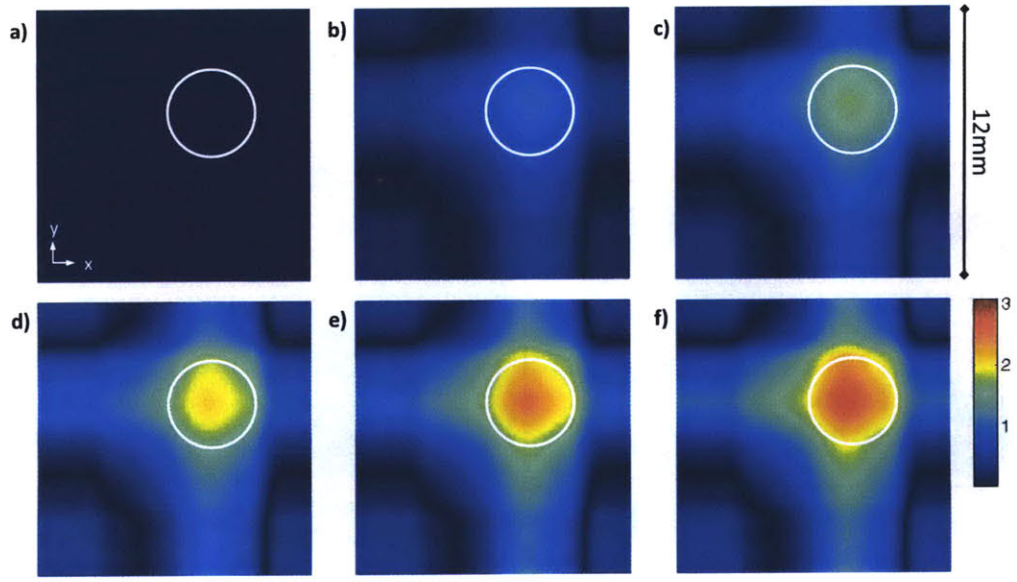

Figure 3-8: Experimental results for a test object. 2D water content reconstructions after a) 0 s, b) 160 s, c) 320 s, d) 480 s, e) 640 s, f) 800 s. The white circle indicates the location of the water drop.

water content profile near the corner of the flow channel area, and its projections, are shown in Figure 3-9(a). For this simulation, a nonlinear diffusion coefficient curve was used [156, 157].

In the experimental data, when we look at a subsection of the data from one angle over time, we are able to resolve three individual flow channels taking on water (Figure 3-9(b)). These experimental results show the overall water content in the membrane increasing greatly in the area where the flow channels are present, then diffusing to the outer areas via in-plane diffusion. As expected, no water content is detected outside the area of the membrane.

Figure 3-10 shows select tomographically reconstructed frames of 2D water content distribution, recovered from the full two angle projection data. As expected, the water is introduced into the membrane first in the area where the flow channels are present, then diffuses outward to the rest of the membrane. The computed water content maximum values are consistently somewhat lower than expected, most likely due to the information spreading caused by few angle tomographic reconstruction.

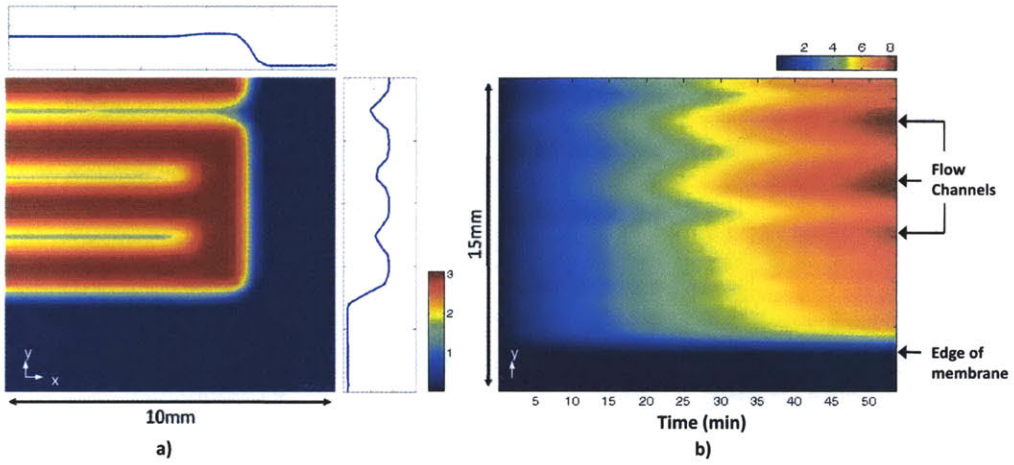

Figure 3-9: (a) FEM simulation of water diffusing outward from flow channels in one section of the Nafion® membrane after 3 min. (b) Projection data over time for one angle. Three individual flow channels are resolved.

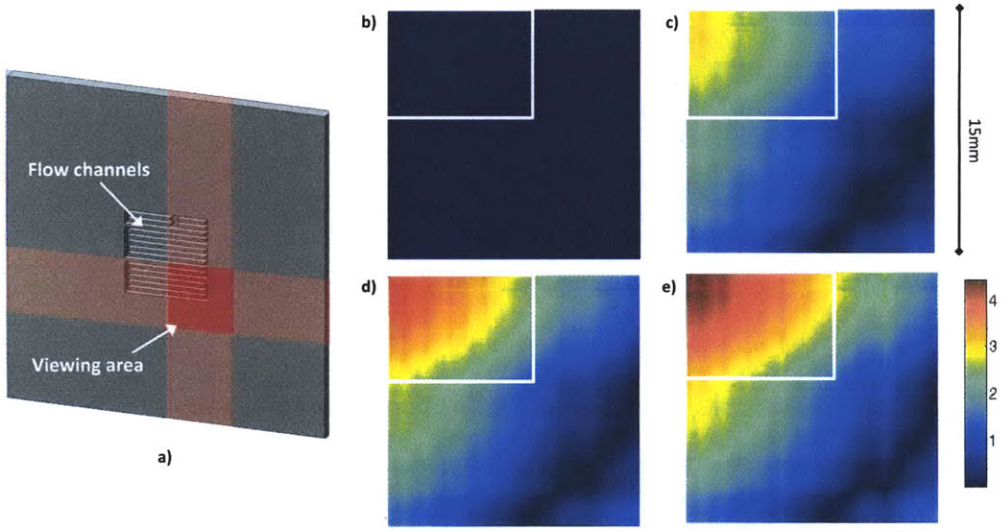

Figure 3-10: Experimental results for fuel cell. 2D water content reconstructions after a) 0 min, b) 15 min, c) 30 min, d) 45 min, e) 65 min, f) 95 min.

3.7 Discussion

We have demonstrated a system capable of in-situ monitoring of water content changes in a PEM fuel cell system by using two-angle interferometric phase tomography with temporal unwrapping of the phase data before conversion to water content data. The unique constraints of the system require modification of standard techniques for phase unwrapping and tomographic reconstruction. We are nevertheless able to obtain reasonable reconstructions of the water content in the fuel cell membrane with only two projection angles, by using a priori knowledge of the distribution smoothness in space and time. This system forms the possible basis for a real-time monitoring system that could be integrated with feedback to keep the fuel cell system operating at maximum efficiency and to prevent failure.

Chapter 4

Transport of Intensity imaging

While interferometry is a useful tool for complex-field imaging, it suffers from extreme sensitivity to environmental conditions and complexity of implementation due to the requirement for a laser source and reference beam. Thus, 'noninterferometric' methods of phase imaging may be more useful in many applications where illumination and optical components are limited. The Transport of Intensity equation (TIE) offers an experimentally simple phase imaging technique for computing phase quantitatively from only two defocused images [63, 65], and the work of Chapters 5-8 is based on or inspired by this technique.

TIE imaging is uniquely able to produce accurate quantitative phase reconstructions with partially coherent light [67], right out to the diffraction limit [68] and without the need for unwrapping [69]. It was originally developed for the Transmission Electron Microscope (TEM) [158] and X-ray imaging [159, 160, 47], where lenses and monochromatic sources are extremely expensive. For the same reasons, TIE has also found use in neutron imaging [161], Lorentz microscopy of magnetic microstructure [162] and matter-wave phase measurement of quantum-mechanical wave-fields [163]. In the optical regime, TIE imaging has been used for cell tracking and confluence [164] and can emulate non-quantitative modalities like DIC [165]. Other extensions involve adding gratings to the system to improve performance [166], use with multi-focal systems [167], solution of the twin image problem in digital holography [168] and tomographic 3D phase imaging [100].

The TIE is a wave-optical technique which involves measuring the derivative of intensity along the optical axis, then solving a partial differential equation (PDE) to recover phase directly. While one cannot in general determine phase from intensity alone, the wave equation specifies uniquely how intensity will propagate [169].

4.1 Theory

When two images are only slightly defocused from each other, phase contrast due to diffraction between the images is linear in intensity [47]. In this regime, the TIE describes a direct solution for phase and amplitude. The general form of the TIE, given previously in Eq. 1.5, is:

$$\frac{\partial I(x,y)}{\partial z} = -\frac{\lambda}{2\pi}\left(\nabla_\perp \cdot I(x,y)\nabla_\perp \phi(x,y)\right), \tag{4.1}$$

where $I(x,y)$ is the intensity in the image plane, λ is the spectrally-weighted mean wavelength of illumination [66], $\phi(x,y)$ is phase at the image, and $\nabla_\perp = \frac{\partial}{\partial x} + \frac{\partial}{\partial y}$ denotes the gradient operator in the lateral dimensions only. Phase can therefore be recovered (to within a constant) from a measurement of the intensity derivative along the optical axis. In the derivation of the TIE [63], another related equation results which is not used for imaging but is included here for completeness (neglecting the (x,y) indices),

$$\frac{4\pi}{\lambda} I^2 \frac{\partial \phi}{\partial z} = \frac{I\nabla_\perp^2 I}{2} - \frac{(\nabla_\perp I)^2}{4} - I^2(\nabla_\perp \phi)^2 + \frac{2\pi}{\lambda} I^2. \tag{4.2}$$

In the case of uniform intensity, the object is a 'pure-phase' object and $I(x,y)$ can be taken out of the gradient operator in Eq. 4.1 and rearranged to simplify the equation to [170]

$$-\frac{2\pi}{\lambda}\frac{1}{I(x,y)}\frac{\partial I(x,y)}{\partial z} = \nabla_\perp^2 \phi(x,y). \tag{4.3}$$

This is a classic Poisson equation, stating that the contrast from a pure-phase object at small defocus is proportional to the Laplacian of the phase [171]. The result

is edge-enhanced images and the potential for single-shot phase imaging [60]. Note that there is no weak phase assumption and the limits on the measurable magnitude of the phase object are only those due to sampling. Furthermore, since the measurement is proportional to the second derivative of phase, large gradients in phase can be recovered with relaxed sampling requirements, compared to the aliasing problems that were described in Section 3.3 for interferometric measurements.

4.1.1 Analogies with other fields

The TIE can be thought of as a local conservation of energy equation, describing the flow of energy in terms of intensity, which is true only in a homogeneous media. Optical rays follow trajectories of the Poynting vector, obeying Fermat's principle and the Eikonal equation, where phase variations bend the rays and redirect the Poynting vector.

The general form for a continuity equation, which describes local conservation of some quantity, q, is

$$\frac{\partial q}{\partial t} = -\nabla \cdot f + s \tag{4.4}$$

where f is flux of the conserved quantity and s incorporates any sources or sinks. This equation appears in many fields, some of which are given in table 4.1. If the TIE (Eq. 4.1) is a continuity equation expressing local conservation of intensity, with t replaced by z, then $I\nabla_\perp\phi$ must describe the flux of intensity along z, or the Poynting vector, which we show to be true in Appendix A. The TIE further assumes that there is no generation or loss of intensity at the boundaries ($s = 0$), though loss at the boundary due to finite apertures could be modeled as a sink.

Light propagation has previously been suggested under the fluid mechanics analogy of optical hydrodynamics [172], for which it also obeys the Euler equation for irrotational flow of inviscid (zero viscosity) fluids [173],

$$k_0\frac{\partial a}{\partial z} + a \cdot \nabla_\perp a = k_0^2 n_0 \nabla_\perp(\Delta n), \tag{4.5}$$

	Conserved quantity
Fluid dynamics	Mass
Heat transfer	Energy
Navier-Stokes	Linear momentum
Electromagnetics	Charge density
Quantum mechanics	Probability density
Optics	Intensity

Table 4.1: Analogies to the continuity equation

where k_0 is the free-space wavevector, n_0 is the refractive index of the media and Δn is the change in index. Here, a is analogous to fluid velocity and z replaces time. Indeed, optical 'flow' has be used to study complicated fluid phenomena by analogy in nonlinear optical media [174] and optics has recently helped to explain fluid phenomena [175, 176].

4.2 Solving the TIE

The solution of Eq. 4.3 is a simple inverse Laplacian, whereas the full complex-field solution to Eq. 4.1 requires two such solutions, as described below [63]. First, we introduce an auxiliary function $\nabla_\perp \Gamma(x,y) = I(x,y)\nabla_\perp \phi(x,y)$ and sub it into Eq. 4.1 to get,

$$\nabla_\perp^2 \Gamma(x,y) = \nabla_\perp \left(I(x,y)\nabla_\perp \phi(x,y)\right) = \frac{-2\pi}{\lambda}\frac{\partial I(x,y)}{\partial z}. \tag{4.6}$$

This is a Poisson equation which can be solved for $\Gamma(x,y)$. Next, we rearrange the definition of the auxiliary function and take the gradient of that equation to get another Poisson equation in terms of phase,

$$\nabla_\perp \left(\frac{\nabla_\perp \Gamma(x,y)}{I(x,y)}\right) = \nabla_\perp^2 \phi(x,y). \tag{4.7}$$

The Poisson solution to this equation gives the desired phase map, and the amplitude distribution is simply the pixel-wise square root of the measured intensity at focus.

4.2.1 Poisson solvers

There are many numerical solutions to the the Poisson equation [177], each having different accuracy and speed performance. Iterative methods, most of which are on the order of $O(N^2)$, include the Jacobi method, conjugate gradient methods and successive over-relaxation. Multi-grid solutions have been suggested as the most accurate, but are quite slow. Direct methods include LU methods, pseudo inverse or FFT methods, of which the last is the fastest for large images.

In this work, an FFT Poisson solver of order $O(N^2 logN)$ is used, because of its speed and computational efficiency [178, 53]. Figure 4-2 shows error plots using this FFT method vs. a multi-grid method, showing minimal loss of accuracy.

The Fourier domain Poisson solution of Eq. 4.3 is given by,

$$\Phi(u,v) = \frac{F(u,v)}{-4\pi^2(u^2+v^2)}, \tag{4.8}$$

where $F(u,v)$ and $\Phi(u,v)$ are the 2D Fourier transforms of the driving term (left hand side of Eq. 4.3) and the desired phase, $\phi(x,y)$, respectively. This solution can be interpreted as a deconvolution in the Fourier domain.

4.2.2 Boundary conditions

Any solution of 2D Poisson equations will require known or imposed boundary conditions [177]. This would mean that we need to know the phase at the boundary of the image, which is impossible since that is what we are trying to measure. If the object is centered in the field of view, zero phase change at the boundary can be assumed, but when Dirichlet or Neumann boundary conditions are falsely assumed, errors will occur [179].

Due to the cyclic nature of the discrete FFT solution, periodic boundary conditions

are expected, which can cause problems without sufficient padding of the matrices. One way to avoid such problems is to use a mirror-padding scheme to force correct boundaries [180]. It is interesting to note that since every pixel in the Fourier domain affects every pixel in the space domain solution, boundary errors should be spread across all pixels, meaning that large image sizes should be less affected overall by erroneous boundary conditions. A simulation of the effect of padding is shown in 4-1. Here, a test phase object with non-zero boundary conditions was used, the intensity derivative was calculated, and the phase solution was recovered using increasingly larger border around the image. The mean RMS error of the result decreases with increased padding, but never reaches zero, since light very near the border will be lost to the system upon propagation.

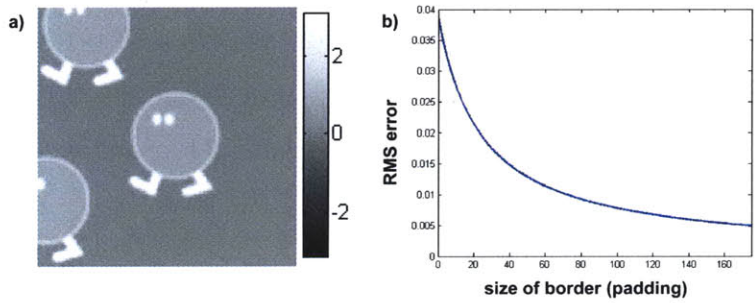

Figure 4-1: (a) Test phase object with non-zero boundary conditions (radians). (b) Error plot as padding is increased (number of extra pixels added to each edge).

4.2.3 Measuring $\partial I/\partial z$

Equation 4.1 is well-posed and invokes only the paraxial approximation. However, since the intensity derivative cannot be measured directly, finite difference methods are used to approximate the derivative from two defocused images centered about the focal plane,

$$\frac{\partial I(x,y)}{\partial z} \approx \frac{I(x,y,\Delta z) - I(x,y,-\Delta z)}{2\Delta z}, \tag{4.9}$$

where Δz is the axial defocus distance. The choice of Δz is an important factor in the quality of the reconstruction. Generally, when Δz is large, the linearity assump-

tion inherent to the finite difference approximation breaks down (see Fig. 4-2(d)). This 'nonlinearity' error blurs the image, in that multiple diffraction fringes give rise to nonlinear phase contrast. Small Δz avoids nonlinearity error, but also leads to a small numerator in Eq. 4.9, which reduces the signal to noise ratio (SNR) of the derivative approximation and results in noisy phase reconstructions, as seen in Fig. 4-2(a). Noise is 1% Poisson noise and plots are of the mean root mean squared (RMS) error across all pixels and 100 trials. Thus, there will be an optimal Δz [181] which is dependent on the object spatial spectrum and the noise characteristics of the camera (see Fig. 4-2(c,e)). As a rule of thumb, we require a Fresnel-like number associated with characteristic feature size, x, to be greater than 1, such that $\lambda \Delta z \leq x^2$.

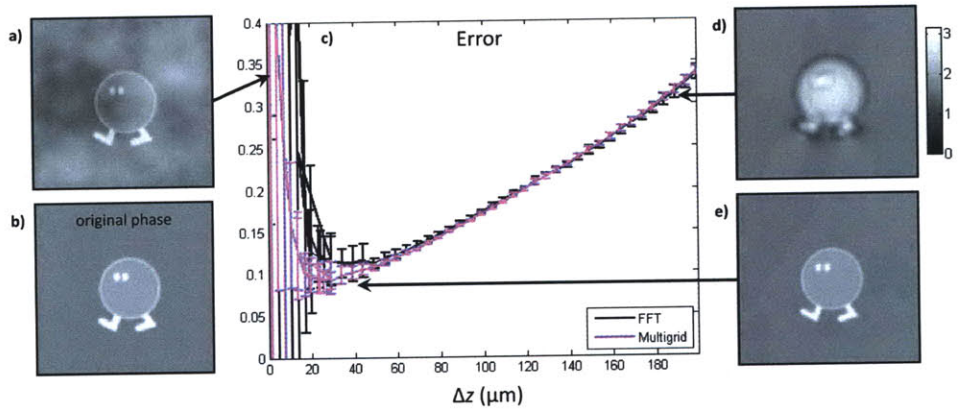

Figure 4-2: Error mechanisms in TIE imaging. (a) Noise corrupted reconstruction at small Δz, (b) actual phase, (c) error in phase reconstruction for increasing Δz. Error bars denote standard deviation, and FFT and Multi-grid refer to the method of Poisson solver. (d) Nonlinearity corrupted phase reconstruction at large Δz, and (e) phase reconstruction at optimal Δz. Phase color scale is $0 - \pi$.

4.2.4 Noise

Due to the requirement for low phase contrast in order to maintain accuracy, the TIE technique becomes extremely noise-sensitive [182], and maximum accuracy is set by the noise floor. As can be seen in Fig. 4-3(a), as noise increases, the optimal Δz also increases because longer propagation distances provide stronger phase contrast, overcoming noise. However, the error never goes below the 'nonlinearity line', so the

minimum reconstruction error goes up nonlinearly with noise, as is seen in Fig. 4-3(b).

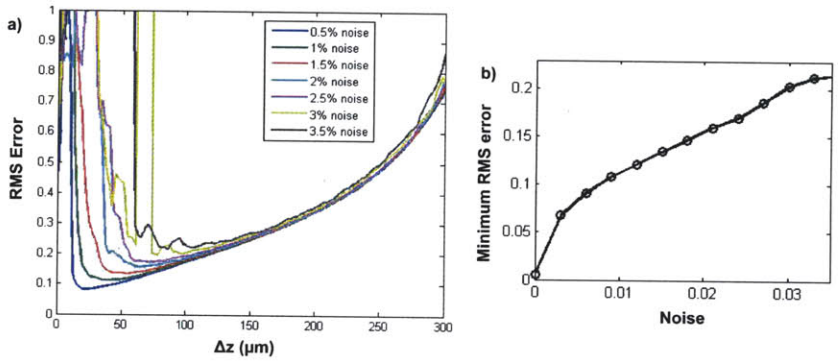

Figure 4-3: (a) Error in reconstructions as Δz is increased for increasing amounts of added noise. Added noise increases the optimal Δz value and (b) increases the error in the optimal reconstruction nonlinearly.

Thus, error is critically dependent on noise and averaging or taking longer exposures is an important way to improve the image quality. Figure 4-4 demonstrates the improvement given by averaging just two images to reduce the noise by a factor of 2.

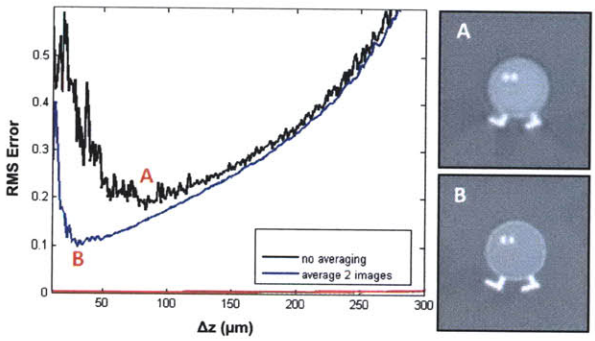

Figure 4-4: Error plots vs. defocus distance for noisy data, where averaging two images leads to a significant improvement in the optimal phase reconstruction.

Work has been done to improve noise instabilities by using more than two images with estimation theory [183], provided that all the images are within the small defocus regime (suggesting low phase contrast). In Chapter 5, we extended the TIE beyond this small defocus limit by using higher order derivatives to correct for nonlinearities, while still allowing improved noise performance [184]. This technique maintains speed and computational efficiency and allows a trade-off between noise performance and accuracy, but fails in the case of significant diffraction between images or large

amounts of noise. In Chapter 6 we seek a more general technique that can adaptively take into account noise and varying distance between images, Δz, with a single model, using Kalman filtering.

4.2.5 Object spectrum

Most of the properties of the TIE are dependent on spatial frequency, because defocus is. Unfortunately, we cannot know a priori the spatial power spectrum for an arbitrary object. The system will be optimal for only one of these at a time. An example of the effect of object spectrum is given in Fig. 4-5, where error is plotted as a function of defocus for increasingly smooth test objects. As expected, smoother objects are better recovered at large defocus distances and nonlinearity error increases with Δz for all objects.

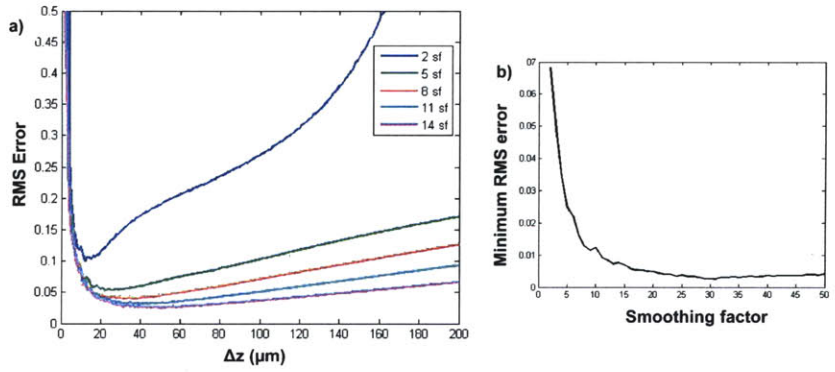

Figure 4-5: (a) Error in reconstructions as Δz is increased for increasing smoothing factor (sf). The 'nonlinearity line' is lower for smoother objects and (b) error drops quickly with smoothness.

4.2.6 Partial coherence

A coherent wave by definition has a well-defined phase. However, in the case of partial coherence, where light is moving in many different directions at once, each direction has a different wavefront and the definition of 'phase' becomes unclear. Nugent [66] has suggested a new definition of phase as the real part of the refractive index of the object under test. Thus, an object can have a clearly defined phase

component, even though the wave-field may not. Furthermore, phase can be defined in terms of the time-average Poynting vector [185] or a particular statistical moment of the mutual coherence [163]. In the coherent case, this becomes the traditional wave phase. The consequence for partially coherent phase imaging with the TIE is that in the paraxial case, where light is mainly traveling in one direction, the average propagation direction of all of the coherent components describes well the average phase contribution [67]. Higher spatial coherence will give better phase contrast; however, lower spatial coherence offers a higher resolution limit, (up to a factor of two greater than the coherent diffraction limit) [4]. This tradeoff was explored using the weakly scattering transfer function formalism of Streibl [186], where it was found that phase information is carried out to the partially coherent diffraction limit with no loss of resolution [68, 187]. An increase in the (in)coherence parameter (NA condensor/NA objective) decreases phase contrast gradually. Temporal partial coherence can also be averaged, such that the TIE can be used with polychromatic illumination [188] using a wavelength value that is the spectrally-weighted mean wavelength of illumination [66]. The validity of the TIE under partially coherent illumination offers a major advantage over interferometric phase imaging techniques for TEM and optical regimes, in that high coherence sources need not be used and resolution can be greater.

4.3 Limitations

TIE methods are known to have a number of practical difficulties, including alignment of the intensity images, accuracy of known Δz, and violation of conservation of intensity due to light leaving the system between images at the boundary [179]. One major disadvantage of the technique is the sequential capture of the images, which requires precise motion of either the object or camera between images. This leads to artifacts caused by object motion and prevents real-time phase imaging. In order to capture both images at once, a beamsplitter could be added to the system and two cameras at slightly different distances from the object could be used. This, however, does not solve the problem of aligning the images and ensuring that there is no tilt

between the images. In Chapter 7, a new version of the TIE will be introduced that allows single-shot phase imaging in real-time, without hardware complications and image registration problems.

One insight gained from the hydrodynamic analogy, which was previously recognized in terms of the TIE [66], is that we cannot measure vector phase contributions with purely orbital angular momentum, since orbital angular momentum will redirect intensity laterally with no change in axial intensity. The consequence of these purely vectorial contributions is phase vortices, which are constrained to have a point where intensity is zero and phase is undefined, thus making the solution non-unique [67]. Luckily, vectorial phase contributions generally do not appear in the near-field, where TIE operates, unless the object itself contains phase vortices.

Chapter 5

Transport of Intensity imaging with higher order derivatives

5.1 TIE imaging with many intensity images

Traditional TIE imaging requires only two images that are defocused from each other; however, there are trade-offs between the amount of defocus, the accuracy of the result and noise considerations, as discussed in Chapter 4. When multiple z plane images are available, the extra information should give better results. However, one cannot simply use the TIE equation to solve for pairs of images and reconstruct the phase from the average of those, as this is equivalent to using the first and last image only, between which the TIE linearity assumption may break down. This chapter demonstrates a method for incorporating many images and correcting for nonlinearity. The technique trades off accuracy and noise suppression while still retaining the computational and experimental advantages of the TIE solution. We show that axial intensity derivatives are well represented by higher order polynomials, where the linear derivative component specifies the phase of the object at focus. This technique greatly increases the validity range of TIE phase retrieval and allows many images to be incorporated into the result for better noise performance.

Soto et al. [183] originally proposed using many images to estimate the derivative by finding the least squares estimator. Their technique allows better noise perfor-

mance; however, higher order derivatives are treated as error. Thus, nonlinearity errors dominate when the total z range exceeds the linear regime defined in Ch. 4. Other approaches for extending the TIE into the Fresnel domain involve using hybrid methods of linearization [189, 190], or using iterative methods [53] very similar to those of the well-known phase diversity technique [36, 71].

We present here a simple modification to the traditional TIE algorithm to account for higher order effects. The result is a better approximation of the first order derivative by estimating higher order derivatives and removing their effect, which leads to more accurate phase retrieval.

5.2 Theory

5.2.1 Derivation

Following the wave-optical derivation of the TIE given in Beleggia [169], in which the Fresnel operator is linearized with respect to z, we showed in [184] and repeat in Appendix B that one can derive a higher order TIE equation by keeping more terms in z when approximating the Fresnel operator by a polynomial. The end result is that keeping higher order terms in the Fresnel operator is equivalent to keeping higher order terms in the intensity derivative. This is expected, since the TIE contains no approximations other than the paraxial approximation, and it is the finite difference measurement of the intensity derivative which causes error. Thus, we may proceed with a simple derivation that seeks to measure as accurately as possible the first derivative of intensity at the focal plane, $z = 0$.

Since intensity does not propagate linearly beyond the small defocus region, due to diffraction, we attempt to estimate and remove the effect of the nonlinear higher order derivatives. Paraxial propagation suggests that the axial intensity curves will remain smooth over multiple wavelengths of defocus. We start with the Taylor expansion of the axial intensity for one pixel in (x, y) as the light propagates,

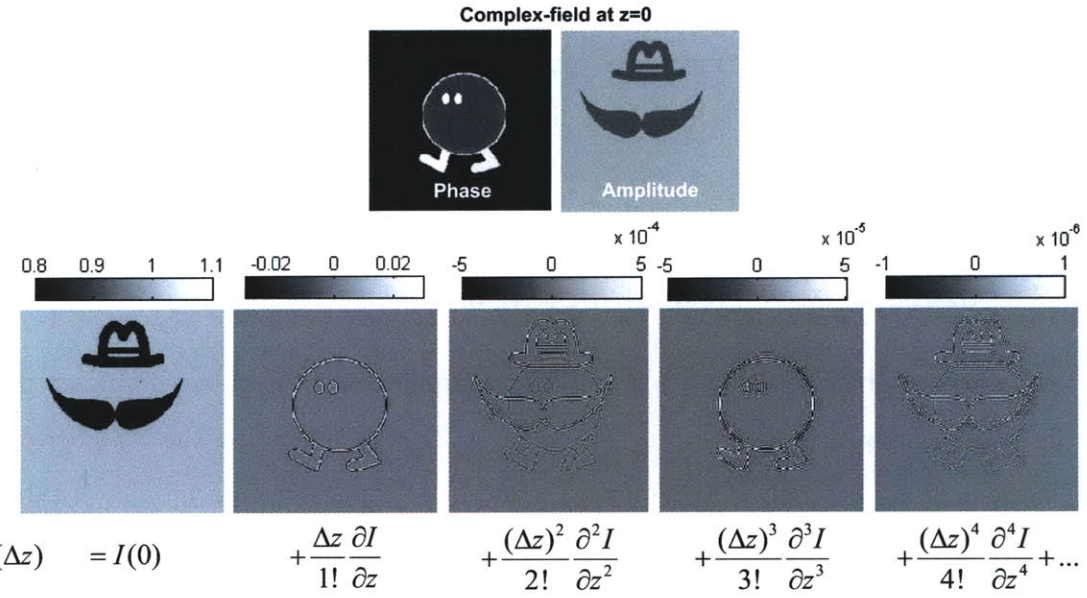

Figure 5-1: Higher order derivative components (bottom) of axial intensity for a propagating test object having separate amplitude and phase variations (top). Note unequal scale bars.

$$I(\Delta z) = I(0) + \frac{\Delta z}{1!}\frac{\partial I}{\partial z} + \frac{(\Delta z)^2}{2!}\frac{\partial^2 I}{\partial z^2} + \frac{(\Delta z)^3}{3!}\frac{\partial^3 I}{\partial z^3} + \frac{(\Delta z)^4}{4!}\frac{\partial^4 I}{\partial z^4} + \ldots \tag{5.1}$$

Here, $I(0)$ is the intensity at focus (including absorption or nonuniform illumination) and $\partial I/\partial z$ is the desired intensity derivative to be used in the solution of Eq. 4.3. These derivative components for a simulated test object (composed of a cartoon phase object and hat and mustache amplitude distribution) are shown in Fig. 5-1. The value of higher order components drops off quickly, suggesting that the Taylor series is a good expansion set for intensity propagation curves. Furthermore, amplitude can be independently extracted from the 0^{th} order derivative, which is the intensity at focus and contains no phase information. Interestingly, only the even derivative orders (0^{th}, 2^{nd},4^{th}) will contain amplitude information. This is because the derivatives of a complex exponential function alternate between being real and imaginary, causing cancellation at every second derivative order upon taking intensity.

Traditional TIE measures the finite difference (FD) approximation to the intensity derivative using Eq. 4.9. Including corrections for the higher order terms given in Eq. 5.1 leads to a new measure of the linear derivative:

$$\frac{\partial I}{\partial z} = \frac{I(\Delta z) - I(0)}{\Delta z} - \left[\frac{(\Delta z)}{2!}\frac{\partial^2 I}{\partial z^2} + \frac{(\Delta z)^2}{3!}\frac{\partial^3 I}{\partial z^3} + \frac{(\Delta z)^3}{4!}\frac{\partial^4 I}{\partial z^4} + ...\right]. \tag{5.2}$$

Thus, the error in the two-plane FD measurement is caused by the higher order derivatives (shown in square brackets in Eq. 5.2). By measuring these higher order components numerically and removing them, one should obtain a more accurate estimate of the first derivative. This new first derivative estimate is then substituted into Eq. 4.3 to solve for phase without reverting to iterative methods.

There is a great body of research on numerical techniques and finite difference schemes for measuring derivatives from more than two measurements [177]. Generally, the n^{th} order derivative of a function can be computed numerically from $(n+1)$ or more equally spaced measurements. Unfortunately, these finite difference approximations for higher orders come with their own error and noise issues. Here, we describe the implementation of two techniques which we found most successful for image-based schemes.

5.2.2 Technique 1: Image weights for measuring higher order derivatives

The effect of measuring and subtracting the unwanted higher order derivatives by finite difference methods leads to the problem choosing a set of image weights such that all but the 1^{st} order in Eq. 5.2 is canceled. Consider the linear derivative that we wish to estimate as a superposition of weighted images:

$$\frac{\partial I}{\partial z} \approx \frac{a_{-m}I_{-m} + a_{-m+1}I_{-m+1} + ... + a_j I_j + ... + a_{n-1}I_{n-1} + a_n I_n}{\Delta z}, \tag{5.3}$$

where a_j is the image weighting, I_j is the intensity image taken at $z = j\Delta z$,

meaning I_0 is the focused image, negative j corresponds to under-focused images, and positive j corresponds to over-focused images. Thus, $(m+n+1)$ is the total number of images. We seek to find coefficients for each image such that the desired orders are canceled. The requirements that must be met in order to expect accuracy of a certain order are given in Table 5.1. Forward derivative measurements refer to using images defocused in one direction only and centered derivative measurements take a set of defocused images both over and underfocused, where the central image is in focus. As expected, canceling higher order derivatives requires more images in order to simultaneously meet all of the desired requirements. The system of equations to be solved is given by [191]:

$$\begin{bmatrix} (-m)^0 & (-m+1)^0 & \dots & (n-1)^0 \\ (-m)^1 & (-m+1)^1 & \dots & (n-1)^1 \\ (-m)^2 & (-m+1)^2 & \dots & (n-1)^2 \\ \vdots & \vdots & \ddots & \vdots \\ (-m)^{m+n} & (-m+1)^{m+n} & \dots & (n-1)^{m+n} \end{bmatrix} \begin{bmatrix} a_{-m} \\ a_{-m+1} \\ a_{-m+2} \\ \vdots \\ a_n \end{bmatrix} = \begin{bmatrix} 0 \\ 1 \\ 0 \\ \vdots \\ 0 \end{bmatrix} \tag{5.4}$$

where $m+n=k$, and k is the order of derivative to be corrected for. Resulting sets of image weights are given in Table 5.1.

The disadvantage of this technique is that the higher order approximations to the first derivative become noise sensitive. For example, in the 2^{nd} order case shown in Table 5.1, I_1 has a weight of 4, meaning that the noise of I_1 is amplified by a factor of 4. Thus, if the 2^{nd} order component is smaller than the noise floor, noise is added to the resulting 1^{st} derivative estimate, making it worse. Since the higher order components are object-dependent, one cannot know where the crossover point will occur without an estimate of the object. One solution is to take 4 images at I_1 and average them, thus achieving noise balance, at the cost of capturing more images at each plane.

Accuracy	Requirements	Forward derivative	Centered derivative
0^{th} order	$\sum_N a_n = 0$		
1^{st} order	$\sum_N a_n n = 0$	$\frac{I_1 - I_0}{\Delta z}$	
2^{nd} order	$\sum_N a_n n^2 = 0$	$\frac{-I_2 + 4I_1 - 3I_0}{2\Delta z}$	$\frac{I_1 - I_{-1}}{2\Delta z}$
3^{rd} order	$\sum_N a_n n^3 = 0$	$\frac{I_3 - 9I_2 + 18I_1 - 11I_0}{6\Delta z}$	
4^{th} order	$\sum_N a_n n^4 = 0$	$\frac{-3I_4 + 16I_3 - 36I_2 + 48I_1 - 25I_0}{12\Delta z}$	$\frac{I_{-2} - 8I_{-1} + 8I_1 - I_2}{12\Delta z}$
k^{th} order	$\sum_N a_n n^k = 0$	Solve Eq. 5.4	

Table 5.1: Finding image weights for a desired order of accuracy.

5.2.3 Technique 2: Polynomial fitting of higher orders

When only a single image at each z position is available, or better noise performance is desired for a large data set, a simple curve fitting technique will offer better performance, at the cost of more computation time. In this technique, $I(z)$ for each pixel is fit to a polynomial model and the first order component is extracted for computing phase via Eq. 4.3. In the limit of first order, the technique will fit to a straight line and the result will be similar to that of of Soto et al. [183]. By fitting to higher order polynomials, however, one can obtain a more accurate estimate of the first order derivative. Here we use a least-squares fit to polynomials which weights all images equally. The order of the polynomial fit function should be less than the number of images used, and more images will result in better noise performance without sacrificing accuracy. The pixel-wise treatment lends itself well to parallel computing, such as computation on a Graphics Processing Unit (GPU).

5.3 Simulations

First, we show simulations of two test phase objects and their nonlinearity error as a function of Δz using Technique 1 (see Fig 5-2). Here we use two simulated intensity images for each phase reconstruction, defocused from each other by Δz. The phase solution is obtained with an FFT Poisson solver, and the root-mean-squared (RMS) error is plotted as the mean over all pixels. As can be seen, the inclusion of a 2^{nd} order correction factor is better than standard TIE (which assumes 1^{st} order) for all values of Δz in the absence of image noise. Note that the curves are object-dependent, though generally, higher order corrections become more useful with large Δz because the nonlinearity is greater in this range. Figure 5-3 shows a similar simulation including up to 4^{th} order correction with no noise. As expected, there is diminished improvement as more orders are corrected for, but the inclusion of higher orders is always beneficial at any Δz. When noise is added, this is no longer true, since the higher order estimates are more sensitive to noise (see Fig. 5-3(b)). Cross-over points form in the error plots and the optimal set of orders to use will be noise and object-dependent, as expected for Technique 1. When the noise balancing scheme described above is used, however, the higher order corrections error curves once again fall below their successive order (see Fig. 5-3(c)).

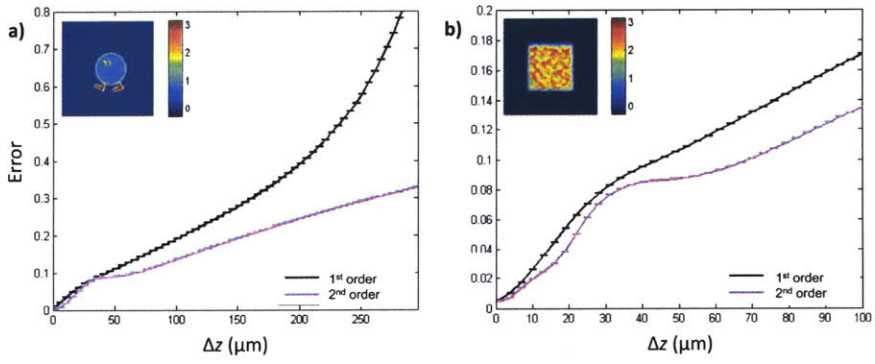

Figure 5-2: Plot of simulated nonlinearity error for two different phase objects as Δz increases, showing improvement when using 2^{nd} order TIE. Inset shows in focus phase image for (a) test phase object and (b) random phase object. Phase values are radians.

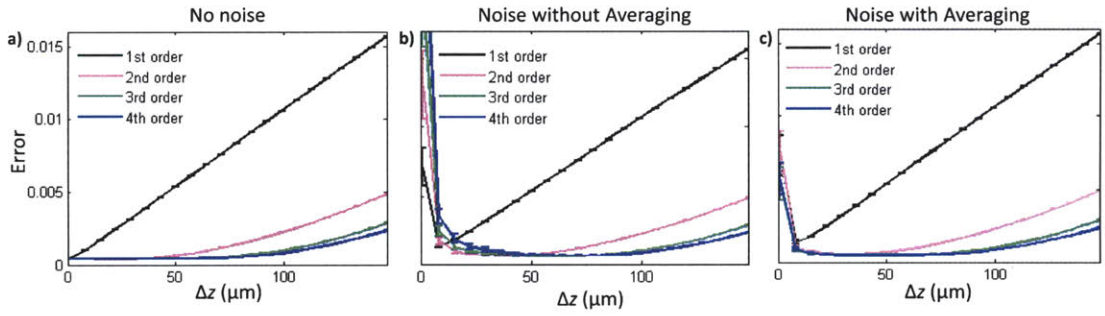

Figure 5-3: Error plots with test object in Fig. 5-2(b) for increasing Δz with a) no noise, b) noise (standard deviation $\sigma = 0.001$) with no averaging, c) noise with averaging. Error bars denote standard deviation.

Figure 5-4(a) shows some simulated intensity images as a pure phase object propagates. The data set uses 80 images axially spaced by $\Delta z = 1\mu$m, with illumination wavelength 532nm and total image size of 90μm. Figure 5-4(b) plots the axial intensity curves for a few randomly selected pixels. Since it is a pure phase object, all pixels have unity intensity at focus ($z = 0$) and the phase contrast is purely antisymmetric. The axial intensity curves in this z range are quite smooth, but severely nonlinear since the data span a z range well beyond the small defocus regime that defines the TIE. Figure 5-4(c) plots a single intensity curve and its corresponding fitted curves for 1^{st}, 7^{th} and 13^{th} orders, showing that the 1^{st} order fit is a very poor estimate, while the 13^{th} order fit is accurate.

Using this data set, we fit each pixel intensity to progressively higher orders of polynomials as described in Technique 2, compute the linear derivative, then solve the TIE for phase. Results are shown in Fig. 5-5. The 1^{st} order reconstruction is quite blurry and cannot pick up sharp edges, which are most susceptible to nonlinearity. Lower spatial frequencies better satisfy the linearity assumption and thus are reconstructed faithfully. Indeed, in the error plots shown in the bottom row of Fig. 5-5, the main source of error is in the pixels near the sharp edges of the lettering. With progressively increasing order polynomial fit, the sharpness of the reconstruction improves and the error decreases.

Figure 5-6 plots the mean actual error in the phase result for increasing polynomial fit order, along with the RMS error of the fit when significant Poisson noise ($\sigma =$

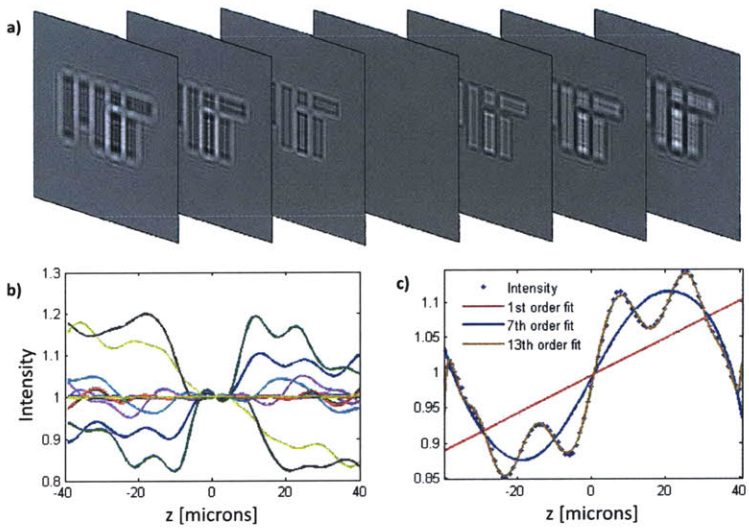

Figure 5-4: (a) Simulated intensity focal stack with a pure phase object (max phase 0.36 radians at focus). (b) Axial intensity profile for a few randomly selected pixels. (c) Single pixel intensity profile with corresponding fits to 1^{st}, 7^{th} and 13^{th} orders, having 0.0657,0.0296 and 0.0042 RMS fit error, respectively.

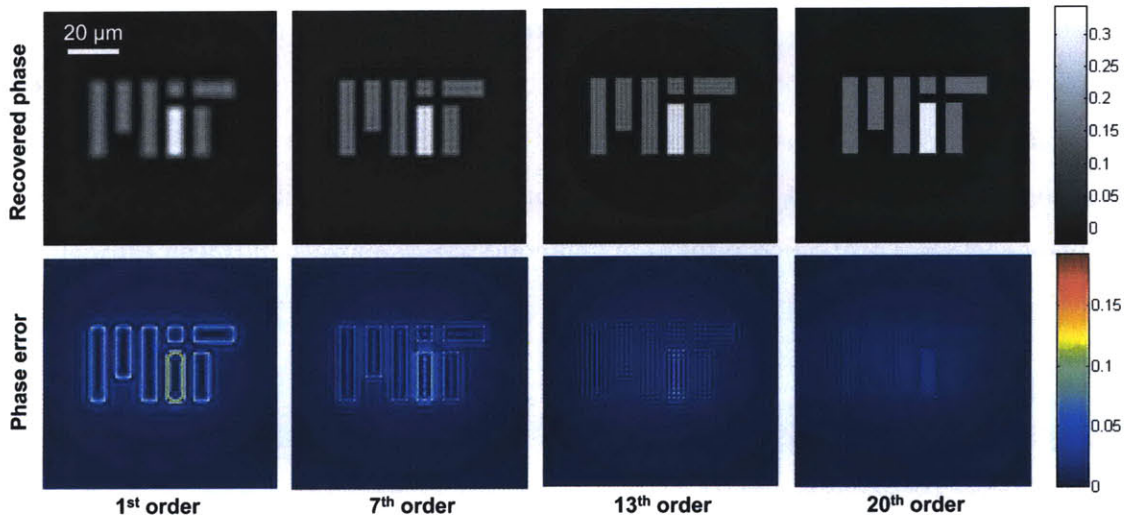

Figure 5-5: Simulation of phase recovery improvement by fitting to higher order polynomials. Top row: Recovered phase (radians). Bottom row: Error maps for corresponding phase retrieved. Polynomial fits are, from left to right, 1^{st} order, 7^{th} order, 13^{th} order, and 20^{th} order.

0.003) is added to each intensity image. It is tempting to use the RMS fit error as a metric for determining the accuracy of the system, but at some point over fitting will occur (*i.e.* adding more fit orders will only serve to fit to noise), resulting in a better fit but more actual error in the result.

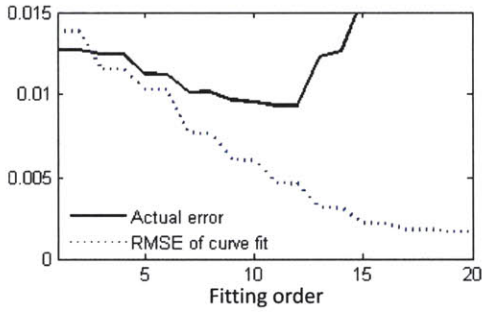

Figure 5-6: Actual error and RMS fit error for increasing fit orders.

A comparison with previously developed techniques using the same data set, but with noise ($\sigma = 0.0015$), is shown in Fig. 5-7. The traditional TIE reconstruction uses only two images, defocused by $2\mu m$ and is extremely sensitive to noise in the low frequencies [182] (mean error=0.110). The Soto method [183] achieves good noise performance, but poor accuracy (mean error=0.025). The blur is due to the model of purely linear light propagation, which is not true. The iterative technique result (mean error=0.024) uses 500 iterations. Finally, the result using 6^{th} order image weighting (technique 1), which uses a data set allowing multiple images at each z plane, achieves both good resolution and good noise suppression (mean error=0.022), as does the result using technique 2 with 20^{th} order TIE (mean error=0.010).

5.4 Experimental results

Intensity focal stack images were taken in an in-line geometry with a $4f$ imaging system between the object and camera. Laser illumination ($\lambda = 532nm$) was used and the CCD sensor was axially translated by $5\mu m$ between each of 60 images (see Fig. 5-8 for results). The phase object in this case is a PMMA substrate with $190nm$ trenches etched into an MIT pattern. As expected, the object becomes nearly invisible at focus,

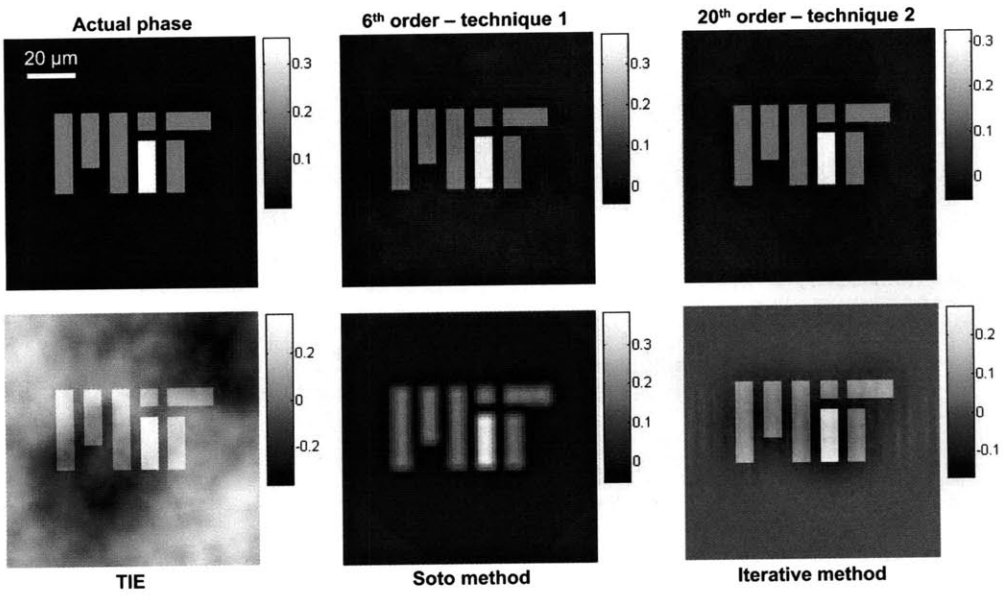

Figure 5-7: Phase reconstructions from simulated noisy intensity images for different phase retrieval algorithms. Color bars denote radians.

with opposite contrast on either side of focus. Phase results are displayed as the height of the object in the axial dimension, where height, h, is given by $h = \phi(\Delta n)\lambda/2\pi$. Similar to the simulated results, the traditional TIE reconstruction is hidden behind low frequency noise and the Soto method is blurred due to nonlinearity. The iterative technique does well for this object but is somewhat noise-sensitive, and 20^{th} order TIE is able to recover a sharp result with good noise performance.

Since the TIE is valid for partially coherent illumination, we can use our improved derivative estimate with stacks of defocused images taken in a brightfield microscope. Experiments were carried out with a 20x objective ($NA = 0.45$), adjusting the microscope focal position in 5 steps separated by $2.6\mu m$. A Tungsten-Halogen lamp source provided broadband illumination. Reconstructions using the two proposed techniques are shown in Fig. 5-9 for both phase and amplitude. Note that sharp edges appear as amplitude effects due to the loss of light from scattering at these edges, and dust particles appear only in the amplitude reconstruction, not the phase reconstruction.

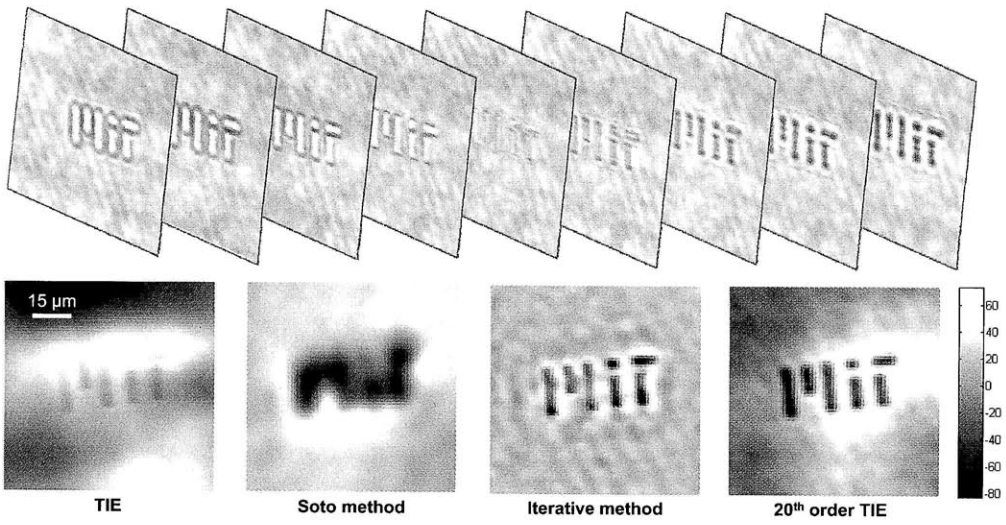

Figure 5-8: Experimental reconstruction of a phase object using different reconstruction algorithms. Top row: subset of the through-focus diffracted intensity images with $\Delta z = 5\mu m$ and effective pixel size of $0.9\mu m$. Bottom row: Traditional TIE phase reconstruction, Soto method, iterative method after 500 iterations, and 20^{th} order TIE using technique 2 (radians).

5.5 Discussion

Including higher order intensity derivatives in the formulation of TIE imaging improves the accuracy of phase estimation. By correcting for nonlinearities, we extend the TIE technique into the Fresnel domain and make use of large stacks of data spanning longer distances, to allow for more practical imaging systems. By fitting to polynomials at each pixel and using many images in the phase solution, we can choose the order of derivative correction to trade off accuracy and noise performance.

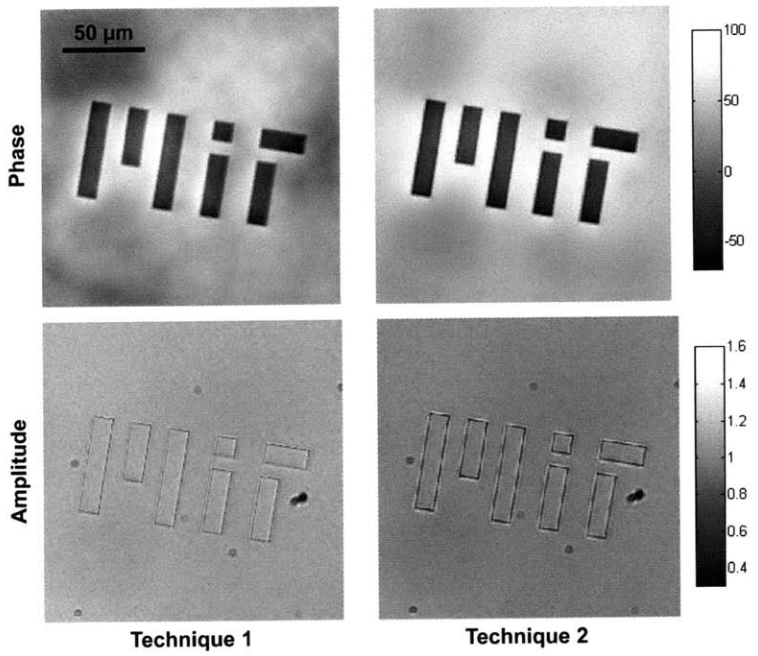

Figure 5-9: Experimental reconstruction of a test phase object from multiple intensity images in a brightfield microscope. Top row: Phase reconstructions (radians), Bottom row: amplitude reconstructions. Left column: technique 1 (4^{th} order), Right column: technique 2 (4^{th} order).

Chapter 6

Complex-field estimation by Extended Kalman Filtering

6.1 Optimal phase from noisy intensity images

In this chapter, a new method for complex-field estimation from noisy intensity measurements in many planes is presented, using a complex extended Kalman filter to model and predict light propagation. The technique offers near-optimal smoothing of noisy measurements and is recursive rather than iterative, so is suitable for adaptive measurements. We discuss several ways to reduce the computational complexity by data compression and block processing. This technique should find use in wavefront sensing for very low-light situations. The framework presented could also allow adaptation for propagation through turbulence, scattering or nonlinear media, where statistical models are available.

The method presented in this chapter allows a stack of noisy defocused images to be used recursively for recovering phase and amplitude, offering near-optimal smoothing in noisy environments. As in all propagation-based phase contrast techniques, the performance of the technique is parameter dependent. To quote Langer [192], "The recorded contrast from the object is non-trivially dependent on the propagation distance, while noise does not follow this relation." Thus, the optimal image planes will depend on the wavefront itself. The recursive and predictive capabilities of the

Kalman filter will enable future applications in adaptive optimal positioning of the image planes by estimating the wavefront and predicting the (wavefront-dependent) optimal next measurement.

6.2 Theory

We wish to determine the 2D optical complex-field, $\psi(x, y, z_0) = A(x, y, z_0)e^{i\phi(x,y,z_0)}$ at a distance z_0 from the camera, where $A(x, y, z_0)$ is amplitude and $\phi(x, y, z_0)$ is phase. We capture a sequence of N noisy intensity measurements, $I(x, y, z_n) = |\psi(x, y, z_n)|^2$ at various distances $z_0, z_1, ...z_n...z_N$ separated by Δz. Assume here propagation through a linear homogeneous medium, so the field propagates according to the homogeneous paraxial wave equation,

$$\frac{\partial \psi(x, y, z)}{\partial z} = \frac{i\lambda}{4\pi}\nabla_\perp^2 \psi(x, y, z), \tag{6.1}$$

where λ is the wavelength of illumination and $\nabla_\perp$ is the gradient operator in the lateral (x, y) dimensions only. Note that $\psi(x, y, z)$ is complex-valued, so this equation is not exactly analogous to the TIE. Assume that the probability distribution of measured intensity at each pixel is independent and Poisson,

$$P\left[I(x, y, z_n)|\psi(x, y, z_n)\right] = e^{-\gamma|\psi(x,y,z_n)|^2}\frac{\left[\gamma\left|\psi(x, y, z_n)\right|^{2I(x,y,z_n)}\right]}{I(x, y, z_n)!}, \tag{6.2}$$

where γ is the gain at the camera. We would like to find the *conditional* probability distribution of $\psi(x, y, z_n)$ given measurements of $I(x, y, z_n)$. Because $I(x, y, z_n)$ is not Gaussian and depends nonlinearly on $\psi(x, y, z_n)$, the estimation problem is nonlinear, and it is extremely computationally expensive to solve for the exact conditional probability distribution $P\left[\psi(x, y, z_0)|I(x, y, z_0), ...I(x, y, z_n)\right]$. One way of obtaining a near-optimal estimate is to use the complex nonlinear Rauch-Tung-Streibel (RTS) smoother [193, 194]. The following theory can be considered an implementation of the extended complex Kalman filter [194, 195, 196].

We represent the complex-field as a raster-scanned complex column vector,

$$a(z) \equiv \begin{pmatrix} \psi(x_1, y_1, z) \\ \vdots \\ \psi(x_M, y_1, z) \\ \psi(x_1, y_2, z) \\ \vdots \\ \psi(x_M, y_M, z) \end{pmatrix}, \tag{6.3}$$

where M is the number of pixels in each dimension (x, y). We must include both the real and imaginary parts of the field in our state vector, since the intensity measurements are a function of both. The evolution of the discretized complex-field is,

$$\frac{da}{dz} = La, \tag{6.4}$$

where L is determined from the paraxial wave equation (Eq. 6.1), which is linear in complex field. The nonlinear measurement set is the intensity of this complex field at all z-steps and is represented by

$$\eta_n \equiv \begin{pmatrix} I(x_1, y_1, z_n) \\ \vdots \\ I(x_M, y_1, z_n) \\ I(x_1, y_2, z_n) \\ \vdots \\ I(x_M, y_M, z_n) \end{pmatrix}. \tag{6.5}$$

The measurement model of the intensity measurement as a function of $a(z_n)$ is given by,

$$\eta_n = h(a(z_n)) + v_n \tag{6.6}$$

$$h(a(z_n))) = \gamma_n \left| a(z_n) a^*(z_n) \right|, \tag{6.7}$$

where the multiplication in Eq. 6.7 is an element-by-element multiplication, * denotes the complex conjugate, γ_n is the camera gain at step n and v_n is sensor noise in the image.

Assume some initial estimate, $\hat{a_0}$, for the statistics of $a(z_0)$ and for its covariance matrices:

$$\hat{a_0} = \langle a(z_0) \rangle \tag{6.8}$$

$$Q(z_0) = \left\langle [a(z_0) - \hat{a}(z_0)] \left[a^*(z_0) - \hat{a}^*(z_0)\right]^T \right\rangle \tag{6.9}$$

$$P(z_0) = \left\langle [a(z_0) - \hat{a}(z_0)] \left[a(z_0) - \hat{a}(z_0)\right]^T \right\rangle. \tag{6.10}$$

where the matrices $Q(z_n)$ and $P(z_n)$ represent discrete values of the coherence functions at z_n, ^{T} denotes transpose, and $Q(z_0)$ and $P(z_0)$ are the initial estimates of these matrices at $z = 0$.

At each subsequent z-step, we propagate forward the state estimate and covariance matrices to find the expected intensity measurement for that z-step:

$$\frac{d\hat{a}}{dz} = L\hat{a}, \tag{6.11}$$

$$\frac{dQ}{dz} = LQ + QL^\dagger, \tag{6.12}$$

$$\frac{dP}{dz} = LP + PL^T, \tag{6.13}$$

where † denotes conjugate transpose. Since the noise covariance $R_n = \left\langle v_n v_n^T \right\rangle$ depends on a_n, we should use the estimated $\hat{a}_n$ to calculate R_n at each step. Since we have assumed that each pixel has independent noise, R_n will be diagonal.

Next, we calculate the Kalman gain matrix, K_n, and the measurement covariance matrix,

$$K_n = \gamma_n \left[Q(z_n)\hat{A}(z_n) + P(z_n)\hat{A}^*(z_n)\right] D_n^{-1}, \tag{6.14}$$

$$D_n = {\gamma_n}^2 \left[\hat{A}^*(z_n)Q(z_n)\hat{A}(z_n) + \hat{A}^*(z_n)P(z_n)\hat{A}^*(z_n) + c.c.\right] + R_n, \quad (6.15)$$

where $\hat{A}(z_n)$ is a diagonal matrix with the diagonal vector equal to $\hat{a}(z_n)$ and H_n is a linearization of the intensity operator matrix,

$$H_n(\hat{a}(z_n)) \equiv \frac{\partial h}{\partial a}|_{a=\hat{a}(z_n)} = \left(\frac{\partial h}{\partial a} \; \frac{\partial h}{\partial a^*}\right)_{a=\hat{a}(z_n)} \quad (6.16)$$

In order for our technique to be valid, this linearization must be justifiable between any two images (*i.e.* the intensity at a given pixel must be linearizable with respect to z). TIE theory tells us that this linearization will be valid when $2\lambda z u^2 < 1$, where z is the propagation distance and u is a given spatial frequency [47]. In practice, nonlinearity, which occurs when the Δz step is too large, causes a low-pass filtering effect of the result.

Next, we update the estimates and covariances:

$$\hat{a}(z_n^+) = \hat{a}(z_n) + K_n\left[\eta_n - h(\hat{a}(z_n)\right], \quad (6.17)$$

$$Q(z_n^+) = \left[I - \gamma_n K_n \hat{A}^*\right] Q(z_n) - \gamma_n K_n \hat{A}^* P^*(z_n), \quad (6.18)$$

$$P(z_n^+) = \left[I - \gamma_n K_n \hat{A}^*\right] P(z_n) - \gamma_n K_n \hat{A}^* Q^*(z_n), \quad (6.19)$$

where I is the identity matrix. These steps are repeated for each z-step until $z = z_N^+$. Once the estimate at z_N is obtained, it can be digitally backpropagated to the focal plane.

A block diagram of the Kalman filter is given in Fig. 6-1. The top loop represents a model of the dynamic system (T represents the transition process and w_n 'process noise', which we assume to be negligible), and the bottom loop represents the estimation process. The iterative technique of Allen et al. [53] can be represented with a similar model, but uses a constant unity gain $K_n = 1$ and iterates through the images many times. In our Kalman filter, unity gain only occurs when there is zero noise (*i.e.* the measurement is exact). Using a gain of less than one suggests that we do not fully trust the measurement. In the input-output method [36] non-unity feedback

is used, but the gain is constant across all pixels and chosen subjectively. In truth, the optimal gain is object-dependent and dynamic across each pixel. By using the Kalman gain matrix, we find the dynamically-changing optimal gain for each pixel as the object propagates, under the limits of model assumptions and linearization. Furthermore, by including the information from each image optimally, we need only consider images once, allowing a recursive rather than iterative algorithm.

An interesting adaptation of this method would involve modeling propagation through turbulent or scattering media as process noise, w_n, or or using an L matrix for propagation through inhomogeneous or nonlinear media.

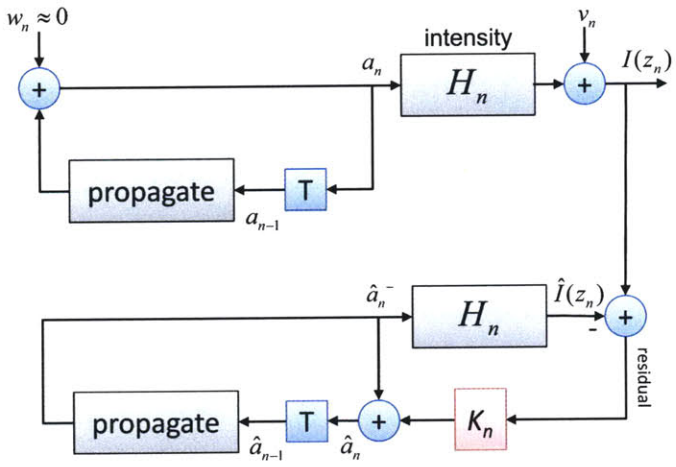

Figure 6-1: Kalman filter schematic diagram.

6.3 Implementation

Direct application of Kalman filtering theory leads to a very large complex state vector of size $2M^2$, where M is the number of pixels in one dimension. This state vector will have a covariance matrix of $4M^4$, which is currently an unrealizable memory requirement on standard computers for typical image sizes. Thus, we suggest two methods for data compression to reduce computational complexity, but point out that the use of 64 bit personal computers and better memory management will significantly relax the computational requirements of this technique in the future. Processing

speed-up was achieved by using parallel processing on a Graphics Processing Unit (GPU), though the main computational limitation was the memory requirements for storage and manipulation of the covariance matrix (currently 3Gb in 32bit Matlab, or hardware limited in 64bit).

6.3.1 Compression method 1. Fourier compression

Smooth images which concentrate most of their information in low spatial frequencies can be represented by less data when sampled in the Fourier Domain (FD). Thus, if Fourier coefficients are used as state variables, a smaller state vector may be used if the image is sparse in the FD. The choice of a suitable sparse domain can use insights from compressive sensing [80]. For example, in imaging through turbulence, phase distributions are often assumed to follow Kolmoogorov statistics [56], namely $\Phi(u) = Cu^{-11/3}$, where $\Phi(u)$ is the power spectrum of the phase and C is a constant. Thus, high frequency information is highly attenuated and a Fourier compression scheme will be useful. For imaging wavefront aberrations in a microscope, the first few Zernike polynomials would be used.

6.3.2 Compression method 2. Block processing

The second method for managing computation involves simply blocking the image into chunks and processing each separately. This will be valid only when phase gradients in one block have negligible effect on the intensity of pixels in the neighboring block. Technically, in Fresnel propagation every pixel transfers information to every other pixel; however, the intensity changes are greatest near the phase disturbance. Thus, one can define, based on Fresnel propagation, a rough estimate of the local area in which the intensity changes at $z = z_N$ occur [20], $\Delta x = 4\sqrt{\lambda z}$. Using a block size larger than this value will minimize crosstalk error.

6.4 Simulations

We simulated the 3D intensity field for a propagating wavefront from a complex object, propagating from focus in $0.5\mu m$ steps over a total distance of $50\mu m$ with wavelength $532nm$. The intensity data was then corrupted by Poisson noise having a standard deviation $\sigma = 0.999$, to yield the noisy test measurements shown in Fig. 6-2. After recursively incorporating all the noisy images into a forward-propagating Kalman filter using block processing (block size 60x60 pixels), the recovered phase and amplitude are shown in Fig. 6-2 as compared to the original object field. Note that the highly scattering sharp edges of the phase information manifest as absorption edges, due to the information being scattered outside the aperture of the system.

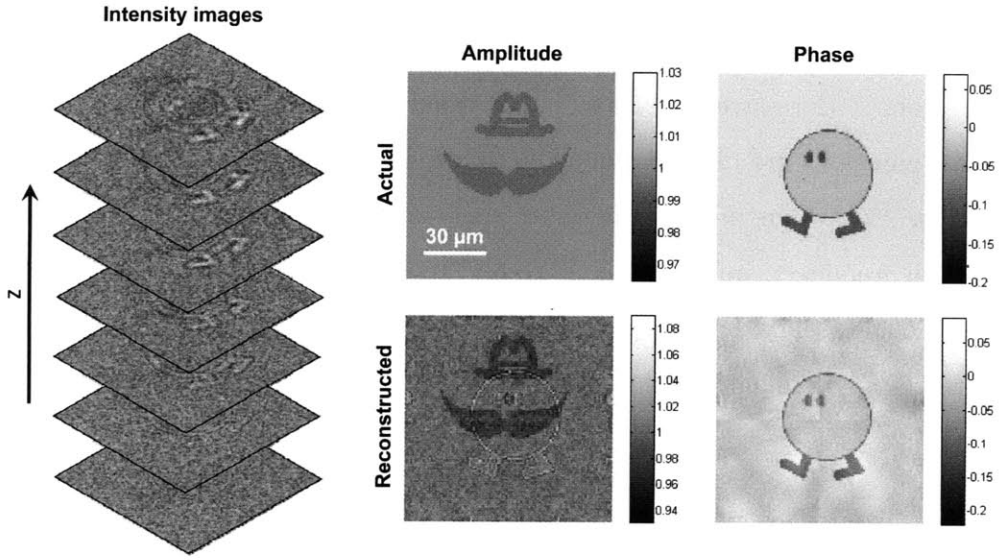

Figure 6-2: Simulated results using Kalman field estimation. Left: selected images from the noisy measurements. Right: actual amplitude and phase at focus compared to the recovered amplitude and phase (radians).

We show in Fig. 6-3 the progress of the filter as images are added and the light propagates. The first and third rows, respectively, show the propagation of amplitude and phase. The second and fourth rows show the Kalman estimation of these quantities as the filter moves from $z = 0$ to $z = 50\mu m$, adding a noisy measurement of intensity at each step to refine the dynamic estimate. We start here with a zero initial

guess and find that the error in both phase and amplitude estimates decreases as more images are added (see Fig. 6-4). Error is defined as the average root-mean-squared (RMS) error across all pixels.

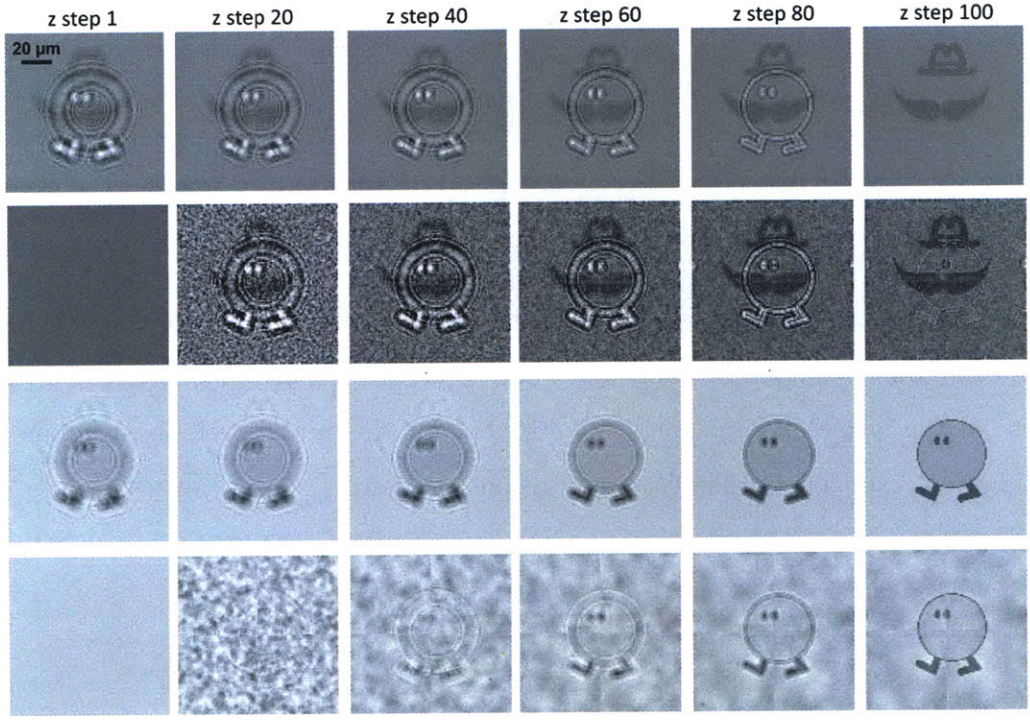

Figure 6-3: Progress of Kalman field estimation. Row 1: Actual intensity as field propagates, Row 2: evolution of intensity estimate from Kalman filter (starts with zero initial guess), Row 3: actual phase (radians) as field propagates, Row 4: evolution of phase estimate (radians) from Kalman filter.

To get a sense of the noise level in the measured data, the simulated actual axial intensity of the central pixel is shown in Fig. 6-5, along with its noise-corrupted measurements. This amount of noise will destroy any complex-field imaging method that does not explicitly account for noise, as we show in Fig. 6-6. We show only the phase of the recovered complex-field, since that is the more difficult parameter to estimate. The TIE technique, even with a large Δz of $50\mu m$ for greater contrast, is taken over by noise. Higher order TIE, as proposed by Waller et al. [184], can trade off noise performance for nonlinearity error correction. The best reconstruction using this noisy dataset is 1^{st} order TIE (similar to Soto method [183]), and is shown in Fig. 6-6

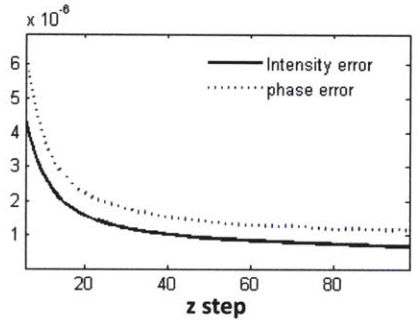

Figure 6-4: Error convergence for Kalman filter as images are added.

to have good noise performance but severe nonlinearity error. Iterative techniques do not account for noise in image data and so are disproportionately affected by the noise of the last image included [39, 46]. So, for this noise level, the Kalman field estimation result offers the best phase reconstruction.

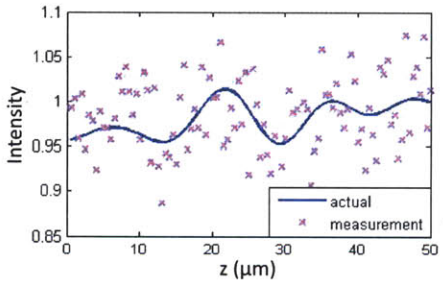

Figure 6-5: Axial intensity curve for a single pixel and its corresponding noisy measurements (Poisson noise, $\sigma = 0.999$).

We present a second demonstration of Kalman field estimation, this time using the Fourier compression scheme described in Sec. 6.2. A smooth (but not bandlimited) pure-phase distribution was used, and results are shown in Fig. 6-7. Here, 50 images with $\sigma = 5.5$ were used, with 18x18 Fourier coefficients kept as state variables, out of 100x100 pixels in (x, y). As expected, the complex-field reconstruction error is on the order of the noise standard deviation divided by the number of images used.

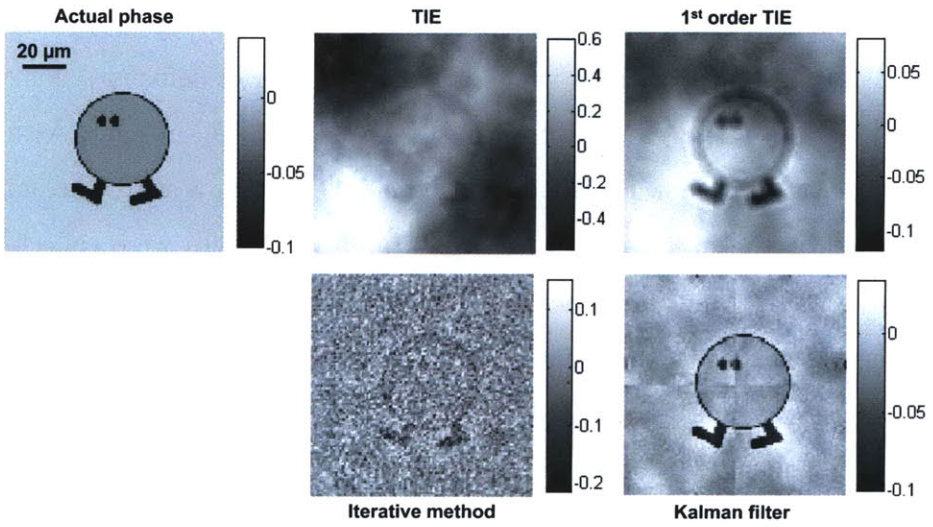

Figure 6-6: Phase retrieval comparison with other techniques. All scale bars indicate radians.

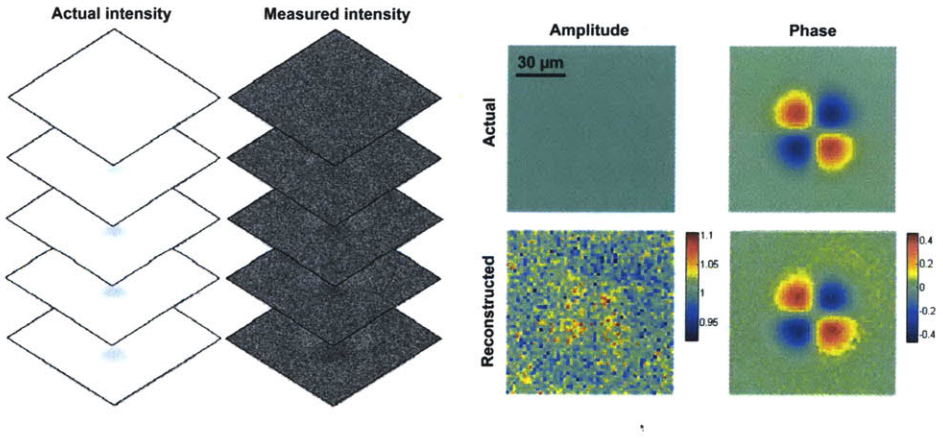

Figure 6-7: Simulated results using Kalman field estimation with Fourier compression. Data set uses 50 images having $\Delta z = 0.2\mu m$ and noise $\sigma = 5.5$. The image is 100 x 100 pixels in size, and 18 x 18 state variables are used. Left: images from actual intensity as light propagates and the noisy measured images. Right: actual amplitude and phase at focus, compared to the recovered amplitude and phase (radians).

6.5 Experimental Results

Experiments were conducted using laser illumination ($\lambda = 532nm$) and a precision motion stage to move the camera while obtaining a stack of defocused images. The test object in this case was an electron beam etched PMMA substrate with $190nm$ trenches. The setup is shown in Fig. 6-8, where a $4f$ system is used to magnify and relay the field at the object to the camera. Intensity images were collected while moving the camera along the optical axis for 50 steps separated by $5\mu m$, where the central image is in focus. A few images from the resulting image stack are shown in Fig. 6-9. Here, the sharp edges of the phase object make the Fourier compression scheme invalid and block processing is used instead. Recovered phase and amplitude are shown in Fig. 6-9.

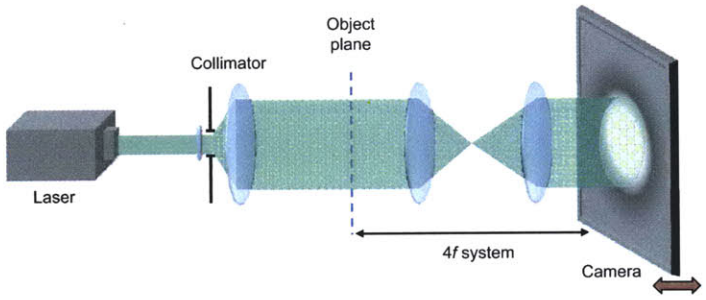

Figure 6-8: Experimental setup using laser illumination and $4f$ system, with camera on a motion stage for obtaining multiple images in sequence.

6.6 Discussion

We have demonstrated the use of Kalman filtering for recovering complex wave-fields from multiple defocused images in severe noise. This technique allows recursive estimation of phase and amplitude with near-optimal smoothing of noise, and has the potential for extension to other difficult imaging situations.

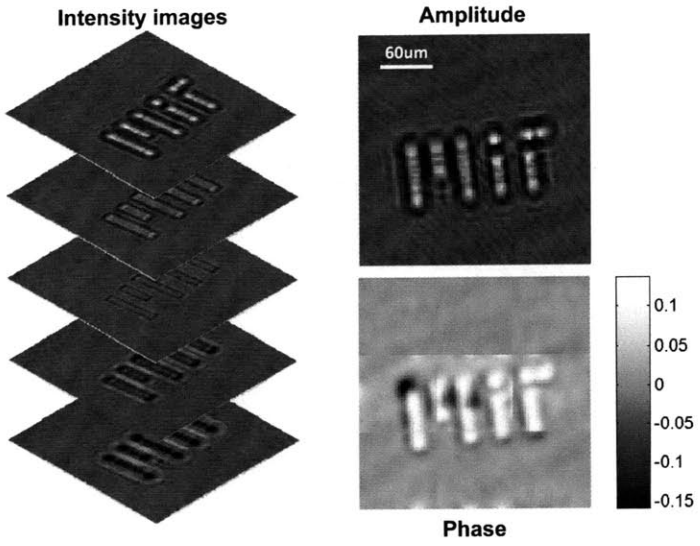

Figure 6-9: Experimental results using Kalman field estimation with block processing. Left: measured images, Right: recovered amplitude and phase (radians).

Chapter 7

Phase from chromatic aberrations

7.1 Introduction

In the previous two chapters, methods were introduced for computing phase accurately from many intensity images and in the presence of noise. Like phase-shifting techniques, these methods will be useful for static or slowly moving objects, where the set of defocused images can be captured quickly enough to avoid motion between images. In many applications, however, dynamic events cannot be captured fast enough using sequential measurements. Examples include fast motion of biological cells, profiling of moving mechanical parts, or fast-changing density fields. A single-shot method would allow real-time quantitative phase imaging of such dynamic events. Furthermore, if efficient algorithms and computing power can be used to recover and display the phase map in real-time, important applications will open up in interactive measurements and adaptive optical correction of wavefront distortions.

Here, we show that phase may be computed accurately from a single color image in a brightfield microscope with no hardware modification. The technique uses a quantification of the chromatic aberration that is inherent to every imaging system [197]. By combining this technique with parallel processing on a standard Graphics Processing Unit (GPU), we demonstrate real-time phase recovery. This leads to a simple and inexpensive way of achieving quantitative phase images in real-time, allowing a new class of high-resolution dynamic and interactive experiments in existing systems.

Our approach is inspired by the TIE under the recognization that, in the Fresnel propagation kernel, wavelength λ and distance z appear always together [198]. Thus, the two variables can be exchanged in the derivation of the TIE equation to yield a version which uses measurements at different wavelengths rather than different positions. By using a color camera (and due to the fact that strict coherence is not required), we are able to capture the images in a single-shot. Furthermore, we show that chromatic dispersion in the imaging system allows in-focus phase images with optimal contrast.

Chromatic dispersion is the phenomenon that causes different wavelengths to propagate at different speeds in a dielectric medium (see Fig. 7-1). The effect was a major impediment to the early development of refractive telescopes. For years, scientists have worked to reduce the resulting chromatic 'aberration' in imaging systems by using long focal lengths, reflective optics or achromatic lenses [199]. Isaac Newton's revolutionary telescope design of the 17^{th} century, which was more powerful than refracting telescopes a dozen times its size, was based on reflective optics to avoid chromatic aberration [200]. In 1973, Courtney-Pratt recognized that these aberrations could be used to gain some depth information about an object [201] because the different colors focused to different depths in the object [202], and this idea was later extended to confocal systems [203] as a method for reducing scanning or for measuring chromatic aberration in a confocal system [204]. Recently, Guichard [205] proposed to use chromatic defocus for extended depth of focus. Here, we propose chromatic dispersion as a phase contrast mechanism, where either free-space dispersion or imaging lens dispersion can be used to recover phase quantitatively. Certainly, it has been recognized previously that image system aberrations can create phase contrast [206] - in fact, defocus is the primary aberration and exactly what is used in the TIE to solve for quantitative phase. The use of chromatic defocus, however, has not been explored as a phase contrast mechanism.

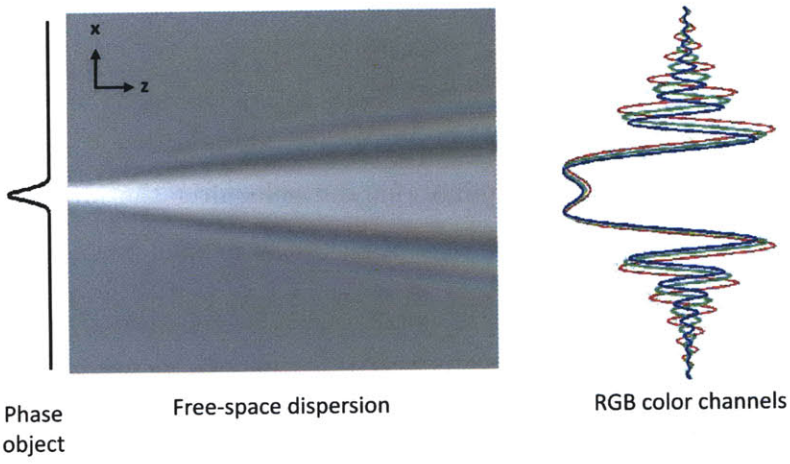

Figure 7-1: Free-space diffraction from a phase object exhibits chromatic dispersion, such that the three color channels (R-red, G-green, B-blue) record different diffracted images.

7.2 Theory

The TIE is derived from the paraxial wave equation after Fresnel propagation [20]. Wavelength λ and distance z are interchangeable in the propagation equation - in fact, defocus is the product of the two $\xi = \lambda z$. Thus, we find:

$$\frac{\partial I(x,y)}{\partial \xi} = \frac{-1}{2\pi}\nabla_\perp \bullet (I(x,y)\nabla_\perp \phi(x,y)), \tag{7.1}$$

where $I(x,y)$ is intensity, $\phi(x,y)$ is phase, and $\nabla_\perp$is the two-dimensional gradient operator in the lateral dimensions. One implementation of this equation allows a defocused phase to be recovered by taking images with different wavelengths in a single plane, similar to that proposed for X-ray imaging with quantified dispersion [159, 207, 208] and in diffraction tomography [209]. Since the technique does not require strict coherence, filters may be used to separate the colors. Thus, we recognize that the images can be retrieved simultaneously from the RGB channels of any color camera, allowing single-shot phase imaging free of lateral or tilt registration problems. Furthermore, we describe below a method for in-focus phase imaging with optimal contrast by introducing a wavelength-dependent z via chromatic aberrations. We assume here a thin phase object with negligible object dispersion.

7.2.1 Derivation

Equation 7.1 is derived as follows. Start with a complex object $\psi(x,y) = A(x,y)e^{i\phi(x,y)}$ where $A(x,y)$ is amplitude, $\phi(x,y)$ is phase and and x, y denote the lateral dimensions. Assuming plane wave illumination, the field after the object is $\psi(x,y)$ and propagates along the optical axis z according to the Fresnel propagation kernel [20],

$$h(x,y;\xi) = \frac{e^{i2\pi z/\lambda}}{i\xi} \exp\left\{\frac{i\pi}{\xi}(x^2+y^2)\right\}. \tag{7.2}$$

At a defocus of ξ, the recorded intensity is

$$I(x,y;\xi) = |\psi(x,y) \otimes h(x,y;\xi)|^2 = \left|\mathcal{F}^{-1}\left\{\Psi(u,v)H(u,v;\xi)\right\}\right|^2, \tag{7.3}$$

where $\mathcal{F}^{-1}$ denotes 2D inverse Fourier Transform, u, v are the spatial frequency variables in Fourier space, and $\Psi(u,v)$ and $H(u,v;\xi)$ are 2D Fourier Transforms of $\psi(x,y)$ and $h(x,y;\xi)$, respectively. We Taylor expand $H(u,v;\xi)$ and linearize with respect to ξ:

$$H(u,v;\xi) = 1 - i\pi\xi(u^2+v^2) - \frac{(\pi\xi)^2(u^2+v^2)^2}{2!} - \ldots \approx 1 - i\pi\xi(u^2+v^2). \tag{7.4}$$

Then, taking into account $i2\pi u \rightarrow \nabla_\perp$, the intensity is given by,

$$I(x,y;\xi) = \left|\psi(x,y) + i\xi\frac{{\nabla_\perp}^2\psi(x,y)}{4\pi}\right|^2. \tag{7.5}$$

After some algebra, this leads to,

$$I(x,y;\xi) = I_0(x,y) - \frac{\xi}{2\pi}\nabla_\perp \bullet (I_0(x,y)\nabla_\perp\phi(x,y)), \tag{7.6}$$

where $I_0(x,y)$ is the in-focus intensity. In the limit of small defocus, this gives Eq. 7.1:

$$\frac{I(x,y;\xi+\delta\xi) - I(x,y;\xi)}{\delta\xi} \approx \frac{\partial I}{\partial\xi} = \frac{-1}{2\pi}\nabla_\perp \bullet (I_0(x,y)\nabla_\perp\phi(x,y)). \tag{7.7}$$

7.2.2 Resolution, accuracy and noise considerations

The x, y resolution of the phase result will be determined by the imaging system; however, accuracy is dependent on the amount of chromatic defocus and noise. Similar to the TIE, Eq. 7.1 is well-posed and invokes only the paraxial approximation; however, the derivative measurement is a finite difference approximation:

$$\frac{\partial I}{\partial \xi} \approx \frac{I(\xi_R) - I(\xi_B)}{\Delta \xi} + \frac{N_R - N_B}{\Delta \xi}, \tag{7.8}$$

where N_R and N_B are are the noise values in the red and blue color channels, respectively, ξ_R and ξ_B are the corresponding defocus, and $\Delta \xi = \xi_R - \xi_B$. The derivative measurement becomes unstable due to amplification of noise by $\Delta \xi^{-1}$. Increasing the defocus between colors provides better signal to noise ratio (SNR) in the derivative estimate; however, the linearity assumption inherent to the finite difference approximation is compromised when defocus is large (see Fig. 7-2). This plot shows simulated noise-free error in the phase result due to nonlinearity as the wavelength and distance between the images are varied. In the limit of infinitesimally small defocus ($\lambda z \to 0$), the error goes asymptotically to zero. Of course, small defocus leads to small signal and noise instability. Thus, the noise floor will determine the minimum acceptable defocus between images, which sets the maximum accuracy according to Fig. 7-2.

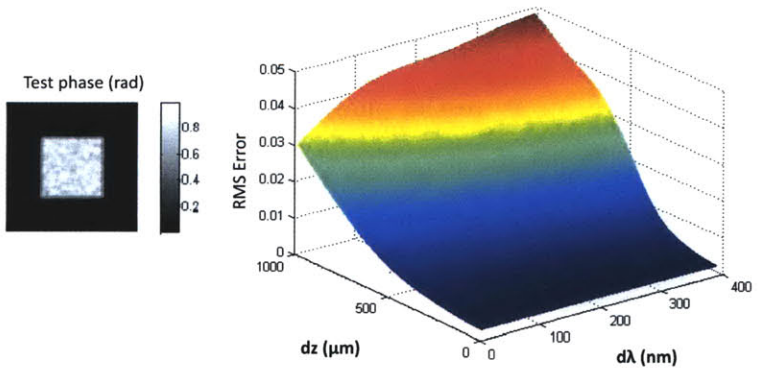

Figure 7-2: Noise-free error simulation for varying values of wavelength and z with a random test phase object. In the absence of noise, the error goes asymptotically to zero with decreasing defocus.

As a general rule for minimizing nonlinearity, we require $\Delta\xi \leq x^2$, where x is the characteristic size of the feature to be reconstructed. This corresponds to the case where there is no more than one significant diffraction ring from a delta function object (see Fig. 7-3), similar to the definition of Fresnel number [31].

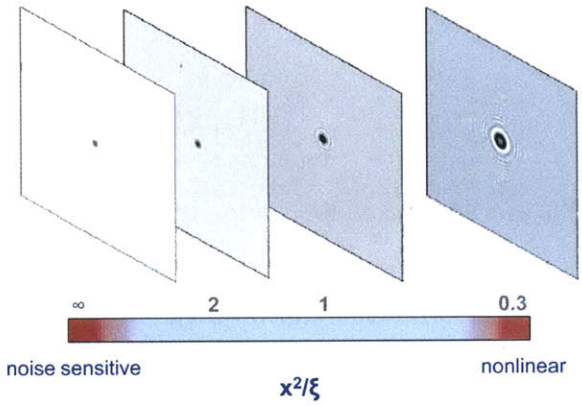

Figure 7-3: Validity range for accurate phase imaging. x is the characteristic object size to be recovered.

7.3 Controlling chromatic aberration

Where there are no optics between the object and the camera (free-space dispersion), the phase recovered will be that at the image plane, yielding a defocused result. We desire an in-focus phase image, where the two colors used are over and under focused by the same amount, making the result accurate to second order. Furthermore, in order to non-destructively measure the phase, an imaging system must be used to relay the complex field being measured to the camera, and all refractive imaging systems have some chromatic dispersion.

Below, we outline the method for designing an in-focus phase imaging system with tunable defocus, either in a $4f$ setup [210] or in a microscope. Microscope objectives usually attempt to correct the effects of chromatic aberration with expensive compound achromatic lenses [199]. Here, we recommend cheap lenses which are not corrected for chromatic aberration, and outline the procedure for quantifying defocus.

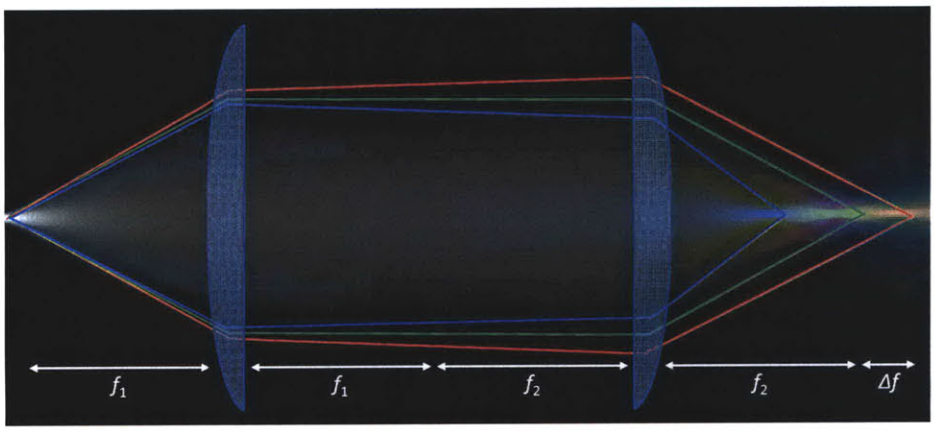

Figure 7-4: Chromatic $4f$ system for controlling wavelength-dependent focus: schematic of ray trace for red, green and blue wavelengths.

7.3.1 Chromatic defocus in a $4f$ system

For a single thin lens, using the Lens maker's formula [210], the shift in focal length f at wavelength λ from the center wavelength λ_0 is:

$$\Delta f(\lambda) = \frac{n(\lambda) - n(\lambda_0)}{(n(\lambda) - 1)} f(\lambda_0), \tag{7.9}$$

where $n(\lambda_0)$ and $n(\lambda)$ are the lens refractive indices at λ_0 and λ, respectively. In a $4f$ system designed for λ_0 (see Fig. 7-4), the wavelength-dependent axial focal shift is

$$\Delta f'(\lambda) = \Delta f_2(\lambda) + \frac{f_2(\lambda)^2}{\Delta f_1(\lambda) + \Delta f_2(\lambda) - (f_1(\lambda)^2 / \Delta f_1(\lambda))}, \tag{7.10}$$

where $\Delta f_1(\lambda)$ and $\Delta f_2(\lambda)$ are the focal length shifts of the first and second lenses, respectively, $f_1(\lambda) = f_1(\lambda_0) - \Delta f_1(\lambda)$ and $f_2(\lambda) = f_2(\lambda_0) - \Delta f_2(\lambda)$. The total chromatic defocus in the $4f$ system is $\xi(\lambda) = \lambda \cdot \Delta f'(\lambda)$ and has been plotted in Fig 7-5(a). Note that defocus is nearly linear with wavelength, allowing for a well-centered measurement of the intensity derivative, with green in-focus and red and blue defocused by equal and opposite amounts.

One can choose $f_1(\lambda)$ and $f_2(\lambda)$ (or the dispersion of the lens material) to tune the slope of this curve such that the optimal defocus exists for a given object.

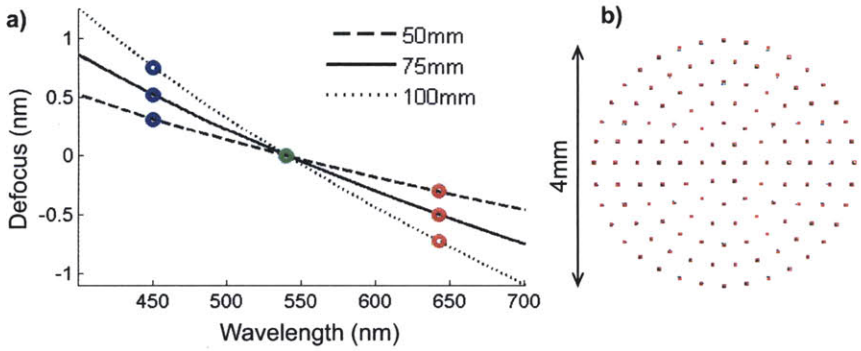

Figure 7-5: Design of a chromatic $4f$ system for differential defocus of color channels. (a) Quantification of chromatic defocus for three values of f_2 given $f_1 = 200mm$ with BK7 lens dispersion, (b) spot diagram at image showing negligible lateral chromatism.

7.3.2 Lateral chromatic aberration

It should be noted that the colors also incur slightly different spherical aberration, giving rise to lateral chromatic aberrations, which the above derivation of chromatic defocus ignores. For a single lens, chromatic defocus is proportional to f/V, while lateral chromatic aberration is proportional to h/V, with h being the lateral field of view and V being the Abbe number of the lens material [210],

$$V = \frac{n_D - 1}{n_F - n_C}, \tag{7.11}$$

where n_D, n_F and n_C are the Fraunhofer spectral lines at 589.2nm, 486.1nm and 656.3nm respectively. For reference, the Abbe number for BK7 glass is 64.7. Thus, axial chromatic aberration will be much stronger than lateral chromatic aberration as long as $h << f$. We show in Fig. 7-5(b) a spot diagram from a Zemax ray trace that demonstrates negligible lateral aberrations in the $4f$ system used, but caution that this condition might become difficult to meet in very high NA systems. Another way to avoid lateral chromatic aberration is to use specialty gradient index or diffractive lenses [211].

7.3.3 Choice of color camera

We have chosen here to use a Bayer filter camera, which is the standard type of color camera. These cameras obtain color information by aligning a filter array over the sensor such that every second pixel is green-filtered, and every fourth is red or blue-filtered, as in Fig. 7-6(a). The spectral response of the filter for a typical color sensor is shown in Fig. 7-6(b).

Lateral aliasing could occur for the maximum spatial frequency that the camera supports, and we suggest oversampling the data by a factor of four to avoid this. In practice, lateral aliasing has not been a problem, and demosaicing algorithms for JPEG images have no noticeable effect on the results. More expensive 3CCD cameras and Foveon sensors would provide perfect lateral sampling; however, the spectral width of the Foveon color channels is much larger than that of the Bayer filter pattern, reducing the contrast between the channels and giving a more noise-sensitive result. Since noise is a critical factor in this technique, Bayer filter cameras have an advantage.

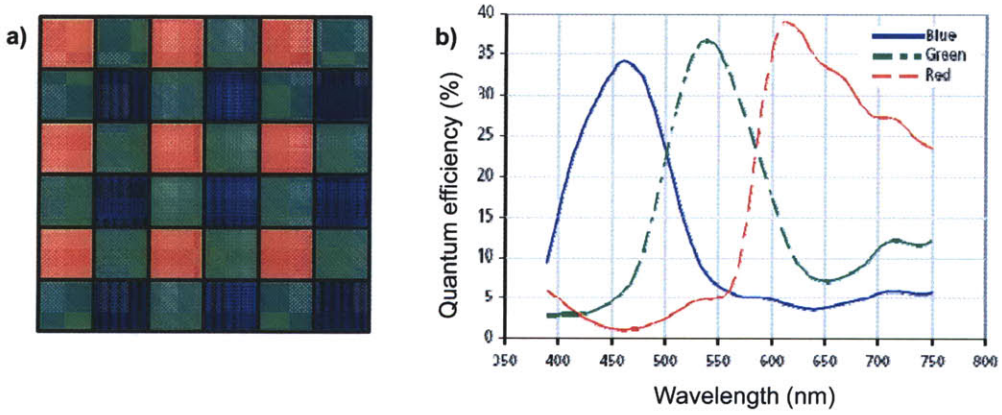

Figure 7-6: (a) Bayer filter color pattern, (b) spectrum of filters in standard Bayer-filter camera.

7.3.4 Imaging with achromats

Since a key application for this technique will be live cell microscopy of fast dynamics, we look next at a microscope imaging system, where most standard objectives are

achromatic or apochromatic (*i.e.* they correct for chromatic defocus at two or more wavelengths). Achromatic objectives which focus red and blue (but not green) wavelengths to the same position will have a wavelength-focus curve of the form shown in Fig. 7-7(a). Thus, the red and blue channel have nearly the same defocus (by design) and measuring the intensity derivative as $\partial I/\partial \xi \approx (I_R - I_B)/\Delta\xi$ will give negligible phase contrast (see example in Fig. 7-7(b)). Instead, the intensity derivative should be measured as follows:

$$\frac{\partial I}{\partial \xi} \approx \frac{(I_R + I_B) - 2I_G}{2\Delta\xi}, \tag{7.12}$$

where R, G and B denote the red, green and blue and $\Delta\xi$ is the defocus difference between the red/blue channels and the green channel. The result is shown in Fig. 7-7(c), giving a much better phase image. Conveniently, the green color channel will have half the noise of each of the red and blue channels, since green occupies twice the area of the total sensor in the Bayer pattern (Fig. 7-6(a)). Therefore, by using achromats and averaging the red and blue channels, we achieve optimal noise performance. Similarly, we can double the resolution of the sensor when red and blue channels contain the same information. Again, the defocus should correspond to a centered derivative measure.

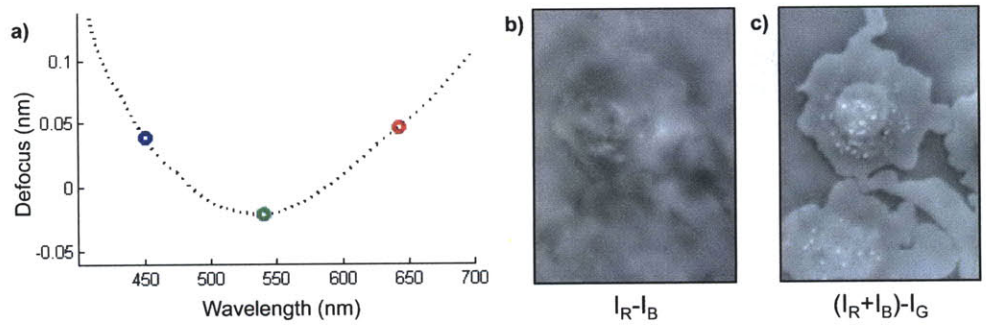

Figure 7-7: Imaging with achromatic lens. (a) Focal shift plot for standard achromatic lens, (b) phase result using standard processing, (c) phase result using achromatic processing.

7.4 Experimental results

A MEMS deformable mirror (DM) array [212] developed for adaptive optics [213] provides a well-characterized dynamic phase object. Using the setup shown in Fig. 7-8, the phase of a DM with 16 actuators addressed was imaged (see Fig. 7-9). The green color channel is in focus (no phase contrast), while the red and blue channels are under and over focused, respectively. From this single color image, the solution of Eq. 7.1 provides a quantitative map of the phase, which is then reinterpreted as height ($height = \phi\lambda/2\pi\Delta n$). The mirror was reconfigured dynamically and the phase was captured in real-time.

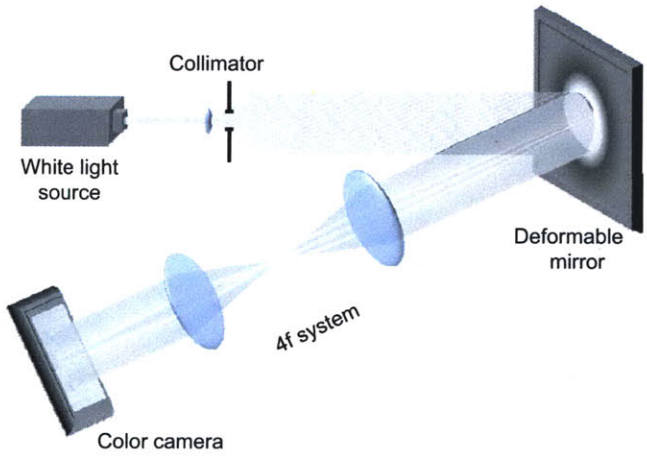

Figure 7-8: Experimental setup for deformable mirror experiments.

For these experiments, the light source was a Tungsten-Halogen lamp, the $4f$ system parameters were $f_1 = 200$ mm, $f_2 = 75$ mm, and a 5 Megapixel camera (Edmund Optics 3112c) with standard Bayer color filter was used. The DM was a Boston Micromachines Corp. 12 x 12 actuator array with $3.5\mu m$ stroke and 8kHz frame rate.

Microscope image results using an achromatic objective with Eq. 7.12 and 7.1 are shown in Fig. 7-10. Images were obtained with a Nikon Eclipse T2000-U using a 20x/0.4NA objective lens and Koehler illumination. Figure 7-10(a,b) demonstrates the capabilities of our system for imaging sharp phase gradients with submicron accuracy. The MIT test object was fabricated by Se Young Yang using electron beam

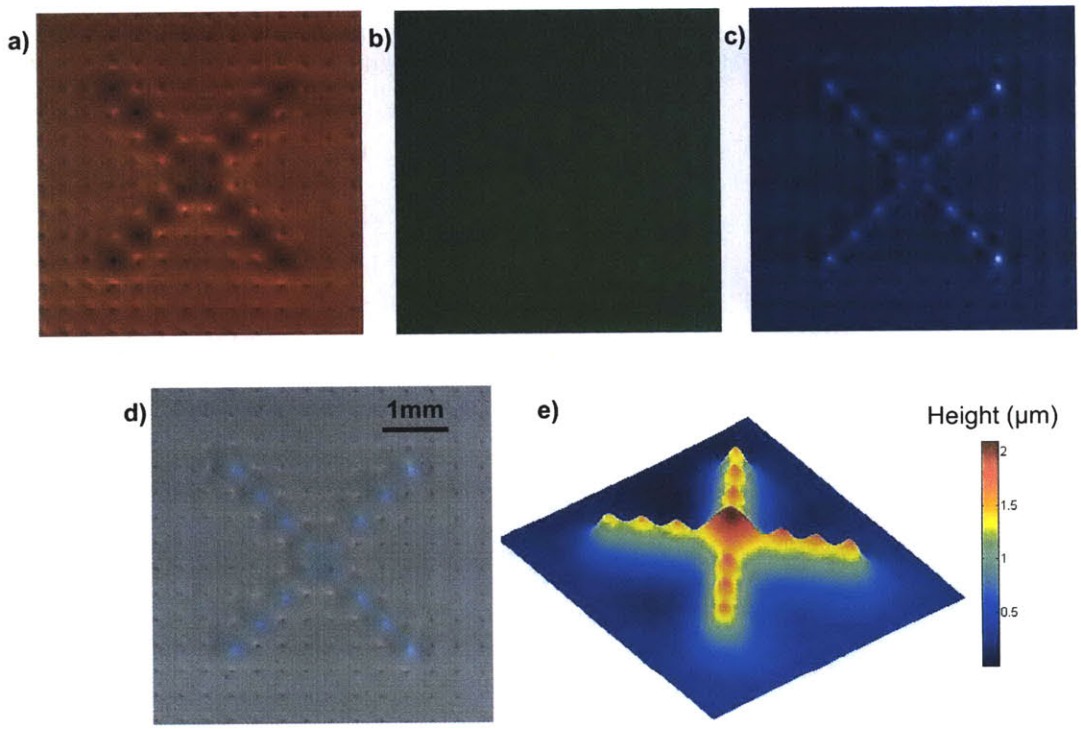

Figure 7-9: Phase retrieval from a single color image. (a-c) Red, green and blue color channels, (d) captured color image of DM with 16 posts actuated. (e) Phase retrieval solution giving inverse height profile across the mirror.

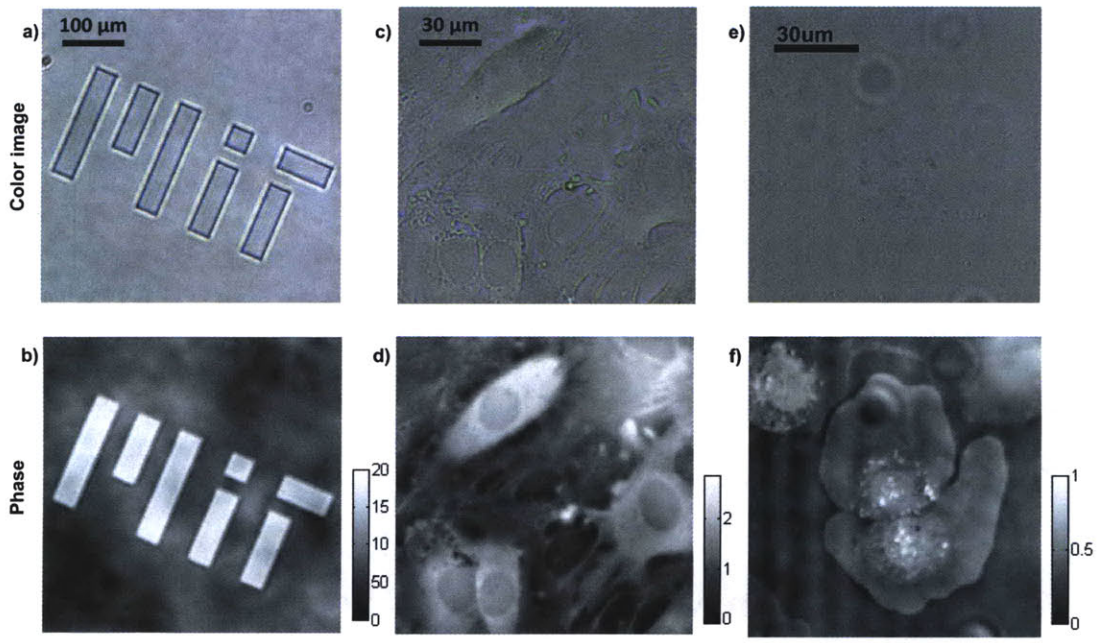

Figure 7-10: Phase retrieval in a standard brightfield microscope. (a) Color image of PMMA test object, (b) recovered phase map (colorbar indicates nm). (c) Color image of live HMVEC cells, (d) recovered optical path length map (normalized). (e) Color image of HeLa cells, (f) Phase map (normalized).

lithography to etch a 190nm deep trench in Polymethyl methacrylate (PMMA). Note that the sharp edges appear as an outlines in the color image, due to light at those sharp edges scattering outside the system aperture. Figure 7-10(c,d) shows phase imaging of a live cell sample of adult human dermal microvascular endothelial cells (HMVEC) in EGM-2MV growth medium (video available by request), and Fig. 7-10(e,f) is a live cell sample of HeLa cells. In the case of the cells, which are much smoother than the MIT object, the contrast is very low in the color images, but still sufficient for obtaining quantitative phase results.

7.4.1 Material dispersion considerations

The disadvantage of this technique is that color-dependent absorption or material dispersion will create artifacts in the result. Reflective objects such as the MEMS deformable mirror presented above will not have these problems, but in the transmission case these may be present. We have found these effects to be minimal in

all of the biological samples presented here, as well as the PMMA test object. For example, in the PMMA test objects, we can roughly calculate the expected erroneous phase shift due to material dispersion. PMMA has a relatively high material dispersion, with refractive index n at the mean color channel wavelengths of $n_R = 1.48858$, $n_G = 1.49423$ and $n_R = 1.50019$ [214]. Thus, the difference in refractive index is about 0.4% of the nominal refractive index, meaning phase shift errors will be approximately 0.4% of the total phase shifts. For the $190nm$ phase objects used here this amounts to a phase shift difference of 0.004 radians, or less than $1nm$ when phase is converted to height.

7.5 Comparison with other methods

A comparison of experimental results to that of a commercial interferometer is shown in Fig. 7-11. The recovered phase maps match very well, although the interferometer result exhibits some streaking, likely due to the unwrapping algorithm aliasing at large phase gradients. TIE-based techniques do not require unwrapping and therefore do not suffer from this problem, making them more suitable for measuring sharp phase objects without stringent sampling requirements in the lateral dimensions. This advantage will be particularly useful in large-scale density measurements such as those explored in Chapter 3, where long optical path lengths lead to large phase gradients. The elimination of the need for phase unwrapping also has advantage in computational speed of computing the result. In the next section, we describe a real-time implementation enabled by parallel processing.

A comparison of the result obtained with traditional TIE is also shown in Fig. 7-12 for images of HMVEC cells. The traditional TIE result was obtained from two oppositely focused images of approximately equivalent defocus as occurs between the color channels, but using the green color chanel only to give equivalent resolution. The difference map shows no obvious systematic differences where the cells are and is mainly a result of the differential noise between the images, giving a cloudy effect. This suggests that material dispersion is not a problem in these results. Some

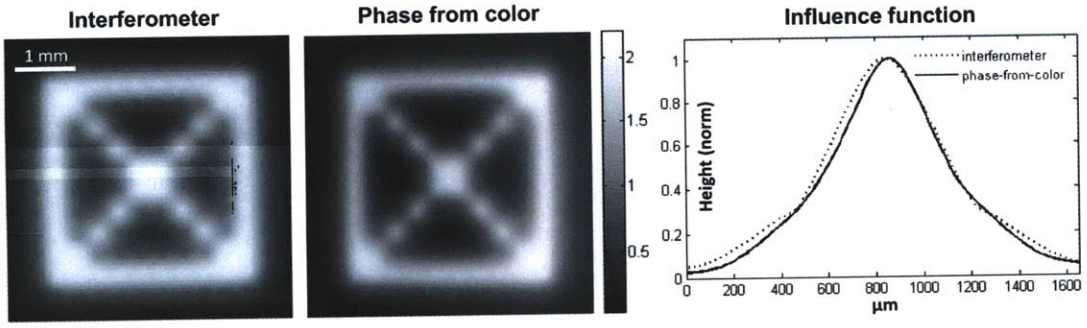

Figure 7-11: Comparison with commercial profilometer data. (Left) Height map from Zygo interferometer compared to (Middle) height map from the technique described here. Colorbar indicates height in μm. (Right) Cross-section along one actuator (influence function of DM) using both techniques.

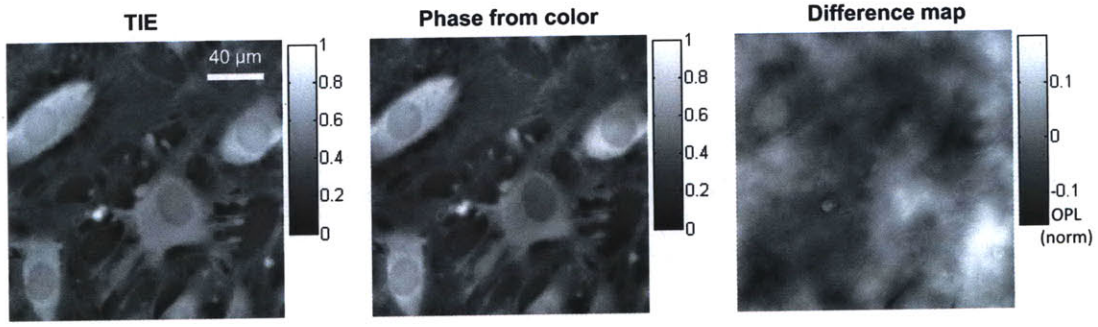

Figure 7-12: Comparison with traditional TIE. (Left) Normalized optical path length (OPL) from traditional TIE, (Middle) normalized OPL from our technique and (Right) the difference between the two results.

small differences are seen at the edges of the cells, but it is difficult to attribute these differences to any one phenomena, since it could be a result of imperfect image registration between the two intensity images in the traditional TIE reconstruction, or due to movement of the cells between the two images captured.

7.6 Real-time computations on a GPU

Given a measurement of $\partial I/\partial \xi$, Eq. 7.1 is solved directly for $\phi(x, y)$ using standard Poisson solvers, as in traditional TIE imaging. Since FFTs are fast (order $N^2 logN$) and amenable parallel processing, the FFT Poisson solution to Eq. 7.1 is used for real-time computation, also offering tolerance to boundary condition errors [53]. Graphics

Processing Units (GPUs) are particularly good for inexpensive parallel computing on a standard computer. GPUs are becoming standard computation tools in optics [215, 216] and computer vision [217, 218], offering huge speedup factors using standard computers. We use here an NVidia GTX 285 GPU with 240 processor cores and 1 GB of memory to solve Eq. 7.1 in real-time. Code was written by Nick Loomis in NVidia CUDA and C [219].

Figure 7-13 outlines the steps used in the real-time processing system on the GPU. A Bayer-encoded image frame is read from the camera into the host computer's memory (CPU), then transferred to the GPU. The color channels are separated out and normalized against the pre-measured background intensity, and then used to compute the defocus derivative, $\partial I/\partial \xi$. Equation 7.1 is then solved by taking a parallelized FFT, deconvolving in the FD with a small regularization parameter proportional to the noise estimate, and then taking the inverse FFT. The resulting phase map is displayed directly from the GPU or returned to the host computer.

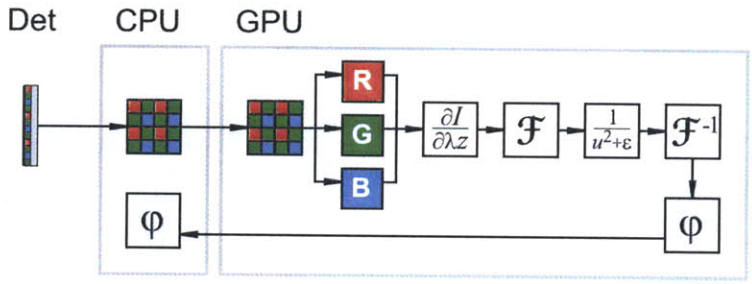

Figure 7-13: Schematic of processing steps on the GPU. Det: detector, CPU: host computer.

A snapshot image from this real-time system is shown in Fig. 7-14, taken win a Nikon Eclipse TE2000-U microscope with 20x achromatic objective (NA=0.4) and slowly dying HeLa cell samples. The individual red, green and blue color channels are displayed, along with their color composite image, showing little phase contrast, and the quantitative phase map recovered is shown on the right-hand side.

Measured performance times are given in Fig. 7-15. The GPU time is the total time spent by the GPU and host computer when calculating phase from a single input image and is the minimum time required per input frame. GPU time is linear with the

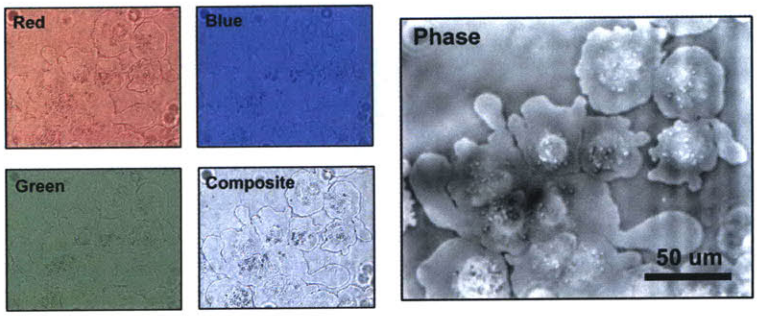

Figure 7-14: Snapshot from real-time reconstruction. Contrast was adjusted for display.

number of pixels and includes fixed overhead from FFT computations. The overhead becomes marginally more significant with faster frame rates, decreasing the relative performance of the GPU - with the GPU falling behind the camera at approximately 2000 fps.

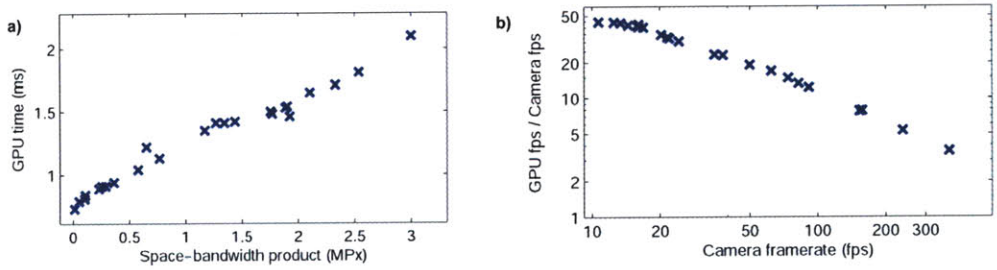

Figure 7-15: GPU performance. (a) Computation time vs. number of pixels in image, (b) GPU speed/camera read-in speed vs. framerate.

7.7 Discussion

We have proposed and demonstrated a new method for high-resolution, in-focus phase imaging that is simple, inexpensive, accurate and only camera-limited in terms of speed. The method benefits from all the advantages of a partially coherent system, namely the potential for diffraction-limited resolution, simple experimental setup, and scalability. The single-shot nature of the technique eliminates hardware misalignment between images and motion artifacts, and there is no specialty hardware to be purchased. In developing this technique, we have explored a new way to look at chromatic

dispersion in imaging systems and described how to use it to gain phase information, rather than treating it purely as aberration. This allows use of inexpensive lenses that are not corrected for chromatic aberration.

Chapter 8

Quantitative phase imaging in a Volume Holographic Microscope

8.1 Introduction

In this chapter, a method for quantitative phase imaging in a Volume Holographic Microscope (VHM) from a single exposure is demonstrated. The VHM system uses a multiplexed volume hologram (VH) to simultaneously collect images from different focal planes. This 3D intensity information is then used to solve the TIE and recover phase quantitatively [220].

8.2 Volume Holographic Microscopy

Volume Holographic Microscopy (VHM) [88, 221] is a technique for imaging 3D intensity information on a 2D camera. It is a versatile tool for real-time spatial and spectral filtering, allowing three-dimensional imaging which, when combined with confocal techniques, obtains depth-sectioned images without scanning [222]. Given the large range of applications in biological imaging, where objects of interest are often transparent or semi-transparent, it is desired to obtain phase contrast within the VHM system. VHM under coherent illumination will have a very narrow field of view; thus, interferometric techniques are not suitable. Knife-edge methods have been im-

plemented recently as a non-quantitative means of phase contrast in the VHM [223]. Here, we describe how to use the TIE imaging technique [63] to quantitatively recover the phase from VHM images, without hardware modification.

Volume holograms (VHs) [224] are recorded in PQ-PMMA with multiple reference beams at slightly different angles, or at different wavelengths [225]. When the VH is illuminated by partially coherent light, Bragg matching ensures that only the light originating from certain depth slices are passed through the VH filter, and each diffracts to a different angle. Thus, multiple depth slices are imaged simultaneously on one camera plane, laterally separated from each other. The number of depth slices is given by the number of multiplexed gratings recorded, and the bandwidth of the illumination determines the lateral width of each slice. A detailed description can be found in Barbastathis [226].

When a thin phase object, such as a biological sample, is placed centered in the system's entrance pupil plane, the resulting VHM image contains a through-focus stack of intensity images, obtained in a single shot. This 3D intensity information can then be used with phase retrieval algorithms to recover quantitative phase information as described below. The phase retrieval algorithm used here is the Transport of Intensity (TIE) technique.

In a similar method, quadratically distorted thin gratings (*i.e.* Raman-Nath regime) were used to obtain two images at different depths in a single shot [227]. These images were later input to phase diversity techniques for wavefront sensing [228]. Much work has been done to extend these results to more efficient gratings [229] and broadband light [230]. However, a Raman-Nath grating quickly loses efficiency and suffers severe crosstalk as more gratings are multiplexed into the hologram. VHM, in contrast, operates in the Bragg regime enjoying two benefits: high efficiency [231] and multiplexing with minimal crosstalk [232, 233, 234]. Chapter 5 described a method for using more than two depth slices of intensity to improve the accuracy of phase recovery. Thin gratings will be limited by crosstalk in the number of depth slices that can be multiplexed and the degradation due to crosstalk, where VHs can record as many depth slices as will fit on the camera, enabling improved phase imaging.

8.3 The VHM system

The VHM system geometry is shown in Fig. 8-1, for the case of a VH with two multiplexed holographic gratings. Illumination is provided by a white light source with notch filter of bandwidth 40nm centered at 532nm. By using broadband illumination with sharp-edged notch filters, crosstalk between depth slices can be minimized (as compared to LED illumination) while still obtaining a large lateral field of view with flat illumination across each slice.

The object to be imaged is placed in the system in transmission mode, and the VH is located in the Fourier plane of a $4f$ imaging system. Each multiplexed grating within the hologram is Bragg matched to a different depth within the object and diffracts to a different carrier spatial frequency, which gets projected to a different location on the camera by the collector lens [235].

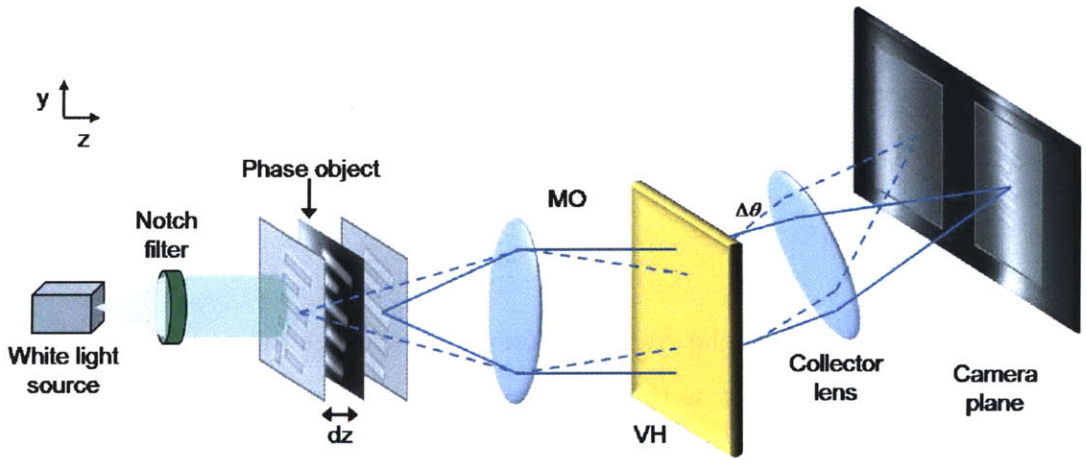

Figure 8-1: Schematic of a VHM system. The VH is located on the Fourier plane of the 4f system, and each multiplexed grating acts as a spatial-spectral filter to simultaneously project images from different depths on a CCD camera, laterally separated. MO is microscope objective.

According to coupled mode theory [231], a grating recorded at one wavelength can be Bragg matched at another wavelength by using a different reconstruction angle. The propagation vectors of the incident ($\vec{k_i}$) and diffracted ($\vec{k_d}$) beams at the Bragg condition are related by the K-vector closure relation,

$$\vec{k_{i,1}} - \vec{k_{d,1}} = \vec{k_{i,2}} - \vec{k_{d,2}} = \vec{K}, \tag{8.1}$$

where $\left|\vec{k_{i,1}}\right| = \left|\vec{k_{d,1}}\right| = \frac{2\pi n}{\lambda}$, $\left|\vec{k_{i,2}}\right| = \left|\vec{k_{d,2}}\right| = \frac{2\pi n}{\lambda}$, $\vec{K}$ is the grating vector, n is the refractive index of the recording material, and λ is wavelength in free space (see Fig. 8-2).

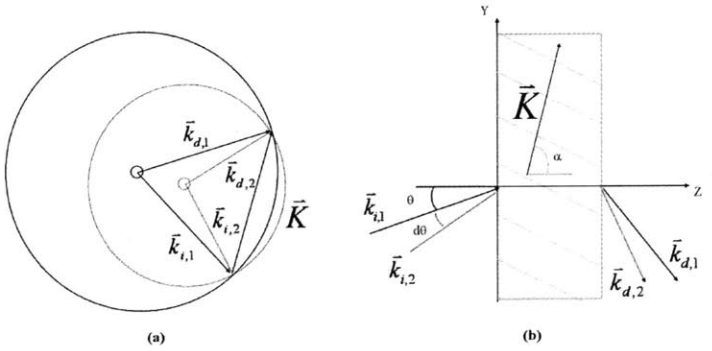

Figure 8-2: (a) Bragg circle diagram (b) Geometry analysis of a volume holographic grating (image courtesy of Yuan Luo).

The relationship between the mismatch in the illumination angle ($d\theta$) and wavelength ($d\lambda$) is given by

$$\frac{\partial\theta}{\partial\lambda} = \frac{K}{4\pi n \sin(\alpha - \theta)} \tag{8.2}$$

where α is the angle of the grating vector with respect to the normal to the recording material surface, and θ is the reconstruction beam angle, as shown in Fig. 8-2. Equation 8.2 shows that incident beams with different wavelengths can be reconstructed using plane-wave illumination at their respective incident beam angles. Thus, lateral information about the object can also be obtained with a broadband source, and the bandwidth determines the field of view.

8.4 TIE in the VHM

The depth-slices must first be extracted from the VHM image which contains one depth slice sub-image for each multiplexed grating. The VHM image is bit-wise di-

vided by the background image (*i.e.* the input field without an object) to normalize the intensity values and account for non-uniform illumination. Where the background image is dark, a division-by-zero instability occurs; thus, a small regularization parameter is used. Once the depth slices have been intensity normalized and cropped from the VHM image, they are laterally registered to each other using a modified cross-correlation algorithm that accounts for opposite phase contrast. Finally, the axial intensity derivative is computed using the depth slices, which is then used to solve for phase via the TIE (Eq. 4.1). One advantage of capturing all the images at once is that object motion between images is not detrimental, and large data sets can be captured simultaneously.

8.5 Experimental results

Experiments were conducted in a transmission VHM system (built by Yuan Luo), with two gratings multiplexed in a single VH. Illumination was provided by a collimated Tungsten-Halogen white light source with a bandpass filter centered at 650nm and having a bandwidth of 40nm. A 50x objective lens (NA=0.65) and a Mitutuyo collection lens formed the $4f$ system, and images were captured on a monochrome CCD array. To test the phase retrieval accuracy, a known test object was fabricated by electron beam etching of PMMA and placed at the object plane of the $4f$ system such that it was halfway between the two multiplexed axial focal planes of the VHM. Figure 8-3(a) shows the captured image using the test object, where the two bright bands correspond to two multiplexed depth slices having an axial separation of $50\mu m$. The two sub-images are oppositely defocused. Figures 8-3(b,c) are the extracted registered depth sections after background normalization, and Fig. 8-3(d) shows the resulting retrieved phase.

The result verifies that the recovered phase is quantitatively accurate. The weak low-pass filter effect is a consequence of the relatively large Δz between the two depth slices. This can be avoided by using a VH that has been recorded with an optimized axial depth slice separation for the object under test.

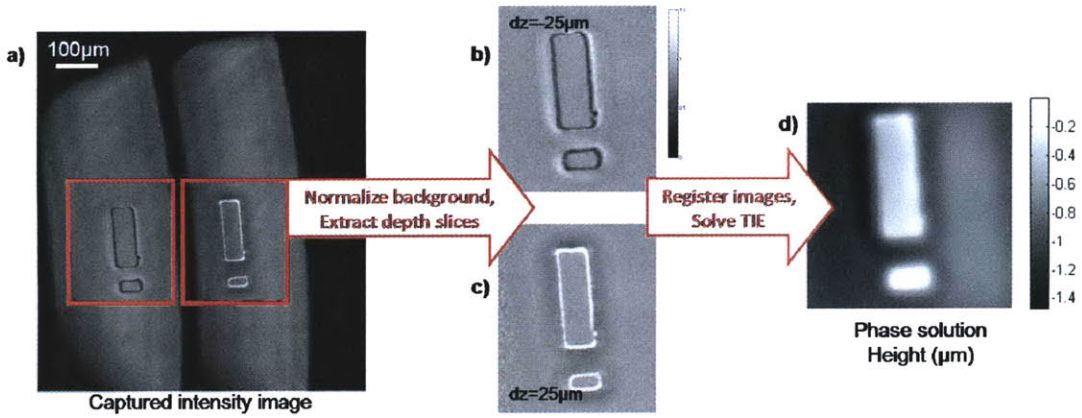

Figure 8-3: Phase recovery from a VHM image. (a) Image captured by the camera. (b,c) Extracted background normalized sub-images, over and under-focused by the same amount. (d) Recovered height.

As a comparison, we imaged the object under similar conditions, but with two separate images between which the object was axially translated by $50\mu m$. These two images were then used to obtain phase information according to traditional TIE imaging. The resulting phase image is compared to that obtained from a single image using our technique in Fig. 8-4, using an onion skin as the phase object.

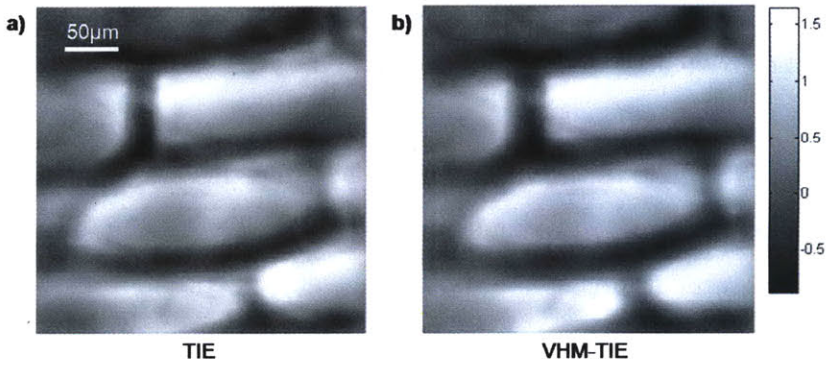

Figure 8-4: Comparison of phase recovery methods with an onion skin object. (a) Phase from traditional TIE method ($\Delta z = 50\mu m$), (b) phase from a single-shot VHM system (radians).

8.6 Discussion

We have demonstrated an extension to the VHM system which allows quantitative phase measurement without hardware modification and from a single-shot. The technique is a promising add-on modality for real-time capture of phase information in a VHM. Furthermore, it opens the door to exploration of fast dynamics with thick phase objects. Future work will include use of VHs with more multiplexed gratings and higher order correction of the nonlinearity in the phase result. Further, 3D imaging with the TIE is an interesting possibility, but has important limitations [187]. 2D phase results from thick weakly scattering objects can be predicted when the defocus distance is on the order of the depth of field and the object is only a few times thicker than the depth of field [236]. If sectioned intensity information can be obtained by a VHM, the opportunity for single-shot 3D phase information without tomography would be a very interesting possible extension of this technique; however, more work is needed to explore this potential.

Chapter 9

Conclusions and future work

This thesis has explored new methods of computational imaging for phase recovery. It was demonstrated that phase tomography can be modified for smooth diffusion distributions to detect and localize large changes in water content in operating fuel cell membranes from very few angles. This system has many other applications in large-scale density measurements, such as temperature or humidity distributions in air. By using temporal unwrapping and very fast sensors, such as line scan sensors, the system would be able to recover large phase gradients from long optical path lengths, making it suitable for such large-scale measurements of dynamic refractive index changes. For the fuel cell application, the next steps are to build a feedback system to correct for water content disturbances. Greater accuracy and detail could be achieved by more sophisticated post-processing and compression techniques could reduce large data sets. As it is, the system is suitable for laboratory studies of operating fuel cells and could be developed to for use in field studies where space is not a constraint and environmental conditions can be controlled. Still, work should be done to reduce the complexity of the system setup. For example, TIE techniques could be investigated for application to the fuel cell membrane measurements.

Higher order axial intensity derivatives were shown to help in recovering accurate phase information from stacks of defocused images, by modifying the TIE technique. This method is practical and should help in improving results for all forms of TIE imaging, particularly where small Δz steps are difficult to accomplish and the linearity

assumption is difficult to meet. When noise corrupts the images, however, the Kalman filtering technique will offer better performance, and is a promising technique for versatile new applications in recovering phase from stacks of noisy images. Further work is needed in assessing the performance of the technique and computing the error bounds. The Kalman filter is highly computational and will benefit from new methods for compression and intelligent data processing with large state vectors, much of which can be found in the literature of control theory. Furthermore, the Kalman filter offers an intuitive way for extending this technique to situations where the 'noise' is not shot noise in the image, but due to scattering media between the object and the camera. This would be done by including 'process noise' in the derivation of the Kalman filter and statistically modeling the scattering process. Furthermore, we point out that the propagation transfer function in the Kalman filter need not be linear homogeneous propagation, and simple adaptations could lead to complex-field estimation as the light propagates through nonlinear or arbitrary refractive index media. Since it is a recursive technique, the Kalman filter could be extended to make adaptive measurements, in which the complex-field is estimated and the optimal transfer function is imposed on the system before the next measurement is taken, achieving the best possible accuracy from intensity measurements.

The work of Chapter 7 demonstrates real-time phase recovery in a white light microscope and should have further applications in imaging of fast-moving cellular dynamics and biological samples in a microfluidic channel, an important field in live cell biological imaging [23]. Adaptive optics (AO), in particular, requires fast calculation of the phase map, and often employs matrix solutions to the phase from low-resolution Shack-Hartmann sensors. The speed and spatial resolution (which are related) of Schack-Hartmann sensors is currently sufficient for today's AO systems because the adaptive mirrors used for correction are currently of low spatial resolution (the largest currently available is 32 x 32 actuators). However, MEMS-based adaptive mirrors offer great promise for scalability, and when these devices reach large actuator counts, speed and resolution of the wavefront sensor will become more important. TIE is currently under investigation as an adaptive optics correction method [237], and is

the basis for the curvature sensing method [238, 239]. Our method for phase recovery still has limitations imposed by using color as a free parameter for obtaining phase. Namely, object wavelength-dependent dispersion and absorption are neglected, and will cause problems when they are significant. More work must be done to study these limitations and possible corrections for them. One attractive application is the use of this technique for large-scale density measurements, such as temperature distributions in air. There could be great experimental advantages in being able to use partially coherent illuminations and capture large changes in density in a single-shot, without the need for phase unwrapping or a separate reference beam.

The work in Chapter 8 can accurately reconstruct 2D complex-field objects from their 3D intensity information obtained in a VHM. Current extensions include the application to color-coded VHM and a more thorough characterization of the hologram in use for digital post-processing correction of fabrication errors. In the case of optically sectioned intensity images, there remains the the very interesting question of 3D phase information and whether it is possible to compute accurately the 3D complex-field of thick objects without tomography. If methods for accurate 3D imaging could be developed in the VHM, it could provide an elegant method of single-shot 3D imaging of phase and amplitude.

Appendix A

Derivation of Poynting vector

$S \propto I\nabla_{\perp}\phi(x,y)$

The term inside the brackets of Eq. 4.1, $I\nabla_{\perp}\phi(x,y)$, can be thought of as the local Poynting vector. Here, we derive this relationship from Maxwell's equations in a source-free region. Thus, the TIE is a local conservation of energy within a homogeneous media, which directly follows from Maxwell's equations. Start with a plane wave traveling predominantly in the $\hat{z}$ direction, $\overline{E} = A(x,y)e^{i\phi(x,y)}\hat{z}$, where A is amplitude and $\phi(x,y)$ is phase.

We use Maxwell's equations in source-free regions in free space [240] with the constitutive relations $\overline{D} = \epsilon_0\overline{E}$ and $\overline{B} = \mu_0\overline{H}$:

$$\begin{aligned} \nabla \times \overline{H} &= \epsilon_0 \frac{\partial}{\partial t}\overline{E} \\ \nabla \times \overline{E} &= -\mu_0 \frac{\partial}{\partial t}\overline{H} \\ \nabla \cdot \overline{E} &= 0 \\ \nabla \cdot \overline{H} &= 0, \end{aligned} \tag{A.1}$$

where $\epsilon_0 = 8.85 \times 10^{-12}$ farad/m and $\mu_0 = 4\pi \times 10^{-7}$ henry/m are, respectively, the permittivity and the permeability of free space. Assuming time harmonic fields,

let $\frac{\partial}{\partial t} \rightarrow i\omega$ to get:

$$-i\omega\mu\overline{H} = \nabla \times \overline{E} = e^{i\phi(x,y)} \left[\hat{x} \left(\frac{\partial A}{\partial y} + Ai \frac{\partial \phi(x,y)}{\partial y} \right) - \hat{y} \left(\frac{\partial A}{\partial x} + Ai \frac{\partial \phi(x,y)}{\partial x} \right) \right], \quad \text{(A.2)}$$

$$\overline{H}^* = \frac{e^{-i\phi(x,y)}}{i\omega\mu} \left[\hat{x} \left(\frac{\partial A}{\partial y} - Ai \frac{\partial \phi(x,y)}{\partial y} \right) - \hat{y} \left(\frac{\partial A}{\partial x} - Ai \frac{\partial \phi(x,y)}{\partial x} \right) \right]. \quad \text{(A.3)}$$

Using the definition of the Poynting vector, $\overline{S} = \overline{E} \times \overline{H}^*$, and substituting in Eq. A.3 and $\overline{E}$, we get:

$$\begin{aligned} \overline{S} \quad &= \hat{x} \left[\tfrac{Ae^{i\phi(x,y)}}{i\omega\mu} \left(e^{-i\phi(x,y)} \left(\tfrac{\partial A}{\partial x} - Ai \tfrac{\partial \phi(x,y)}{\partial x} \right) \right) \right] \quad \text{(A.4)} \\ &\quad + \hat{y} \left[\tfrac{Ae^{i\phi(x,y)}}{i\omega\mu} \left(e^{-i\phi(x,y)} \left(\tfrac{\partial A}{\partial y} - Ai \tfrac{\partial \phi(x,y)}{\partial y} \right) \right) \right] \\ &= \tfrac{-iA}{\omega\mu} \left(\hat{x} \tfrac{\partial A}{\partial x} + \hat{y} \tfrac{\partial A}{\partial y} \right) + \tfrac{A^2}{\omega\mu} \left(\hat{x} \tfrac{\partial \phi(x,y)}{\partial x} + \hat{y} \tfrac{\partial \phi(x,y)}{\partial y} \right) \\ &= \tfrac{-1}{\omega\mu} \left(iA\nabla_\perp A + I\nabla_\perp \phi(x,y) \right). \quad \text{(A.5)} \end{aligned}$$

Therefore, the time-average Poynting vector power density is,

$$\langle S \rangle = \frac{1}{2} Re \left\{ \overline{S} \right\} = -\frac{1}{2\omega\mu} \left[I\nabla_\perp \phi(x,y) \right], \quad \text{(A.6)}$$

and the proof is complete.

Appendix B

Wave-optical derivation of Higher Order TIE

We provide here an alternative derivation of the higher order TIE technique described in Ch. 5. The derivation follows a similar path as the wave-optical derivation of traditional TIE given in Beleggia [169]. Here we show only the 1D version for clarity, where the 2D extension is straightforward.

The key to the derivation is a Taylor expansion of the Fresnel operator $H(x; z, \lambda)$ in the Fourier Domain:

$$H(u; z, \lambda) = e^{-i\pi\lambda z u^2} = 1 - i\pi\lambda z u^2 - \frac{(\pi\lambda z)^2 u^4}{2} - ..., \tag{B.1}$$

where u is the spatial frequency variable, λ is the spectrally-weighted mean wavelength of illumination, and z is the propagation distance. In the traditional TIE derivation, only the first two terms are kept (*i.e.* linearization with respect to z). For higher order TIE, we keep more than the linear terms. Here, we derive 2^{nd} order TIE as an example.

We use $\psi(x) = Ae^{i\phi(x)}$ to represent the wave-field or complex object transmittance function to be recovered, with $\Psi(u) = \mathcal{F}\psi$ being its Fourier Transform. The measured intensity, $I(x; z, \lambda)$, of a wave-field propagated by z is therefore:

$$
\begin{aligned}
I(x;z,\lambda) &= \left|\mathcal{F}\left\{\Psi(u)H(u;z,\lambda)\right\}\right|^2 \\
&= \left|\mathcal{F}\left\{\Psi(u)(1-i\pi\lambda z u^2 - \frac{(\pi\lambda z)^2 u^4}{2} - ...)\right\}\right|^2
\end{aligned} \tag{B.2}
$$

then, using $i2\pi u \rightarrow \nabla$, we get:

$$
\begin{aligned}
I(u;z,\lambda) &= \left|\psi(x) - i\lambda z\frac{\nabla^2\psi(x)}{4\pi} - \frac{\lambda^2 z^2\nabla^4\psi(x)}{32\pi^2} - ...\right|^2 \\
&= \psi(x)\psi(x)^* - \frac{i\lambda z}{4\pi}\left[\left(\nabla^2\psi(x)^*\right)\psi(x) - \left(\nabla^2\psi(x)\right)\psi(x)^*\right] \\
&\quad -\frac{\lambda^2 z^2}{32\pi^2}\left[\left(\nabla^4\psi(x)^*\right)\psi(x) - \left(\nabla^4\psi(x)\right)\psi(x)^* + 2\nabla^2\psi(x)\nabla^2\psi(x)^*\right] \\
&\quad -\frac{i\lambda^3 z^3}{128\pi^3}\left[\left(\nabla^4\psi(x)^*\right)\nabla^2\psi(x) - \left(\nabla^4\psi(x)\right)\nabla^2\psi(x)^* + ...\right]
\end{aligned} \tag{B.3}
$$

In the case of 2^{nd} order, this expression simplifies after some algebra to:

$$
\frac{\partial I(x)}{\partial z} - \frac{\Delta z}{2}\frac{\partial^2 I(x)}{\partial z^2} - ... = -\frac{\lambda}{2\pi}\nabla(I(x)\nabla\phi(x)). \tag{B.4}
$$

References

[1] F. Zernike, "How I discovered phase contrast," *Science*, vol. 121, no. 3141, 1955.

[2] C. Vest, *Holographic Interferometry.* NY: Wiley, 1979.

[3] C. J. R. Sheppard and T. Wilson, "Fourier Imaging of Phase Information in Scanning and Conventional Optical Microscopes," *Royal Society of London Philosophical Transactions Series A*, vol. 295, pp. 513–536, 1980.

[4] C. Sheppard, "Defocused transfer function for a partially coherent microscope and application to phase retrieval," *Journal of the Optical Society of America*, vol. 21, no. 5, 2004.

[5] F. Zernike, "Phase contrast, a new method for the microscopic observation of transparent objects," *Physica*, vol. 9, 1942.

[6] H. Bruning, D. Herriott, J. Gallagher, D. Rosenfeld, A. White, and D. Brangaccio, "Digital wavefront measuring interferometer for testing optical surfaces and lenses," *Applied Optics*, vol. 13, no. 11, 1974.

[7] J. Schmit and K. Creath, "Fast calculation of phase in spatial n-point phase-shifting techniques," M. Kujawinska, R. J. Pryputniewicz, and M. Takeda, Eds., vol. 2544, no. 1. SPIE, 1995, pp. 102–111.

[8] J. E. Millerd, N. J. Brock, J. B. Hayes, M. B. North-Morris, M. Novak, and J. C. Wyant, "Pixelated phase-mask dynamic interferometer," K. Creath and J. Schmit, Eds., vol. 5531, no. 1. SPIE, 2004, pp. 304–314.

[9] B. T. Kimbrough, "Pixelated mask spatial carrier phase shifting interferometry algorithms and associated errors," *Appl. Opt.*, vol. 45, no. 19, pp. 4554–4562, 2006.

[10] D. Ghiglia and M. Pritt, *Two-dimensional phase unwrapping: theory, algorithms and software.* Wiley Blackwell, 1998.

[11] D. Ghiglia and L. Romero, "Robust two-dimensional weighted and unweighted phase unwrapping that uses fast transforms and iterative methods," *Journal of the Optical Society of America*, vol. 11, no. 1, 1994.

[12] E. Wolf, "Three-dimensional structure determination of semi-transparent objects from holographic data," *Optics Communications*, vol. 1, no. 4, pp. 153 – 156, 1969.

[13] ——, "Determination of the amplitude and the phase of scattered fields by holography," *Journal of the Optical Society of America*, vol. 60, no. 1, pp. 18–20, 1970.

[14] U. Schnars and W. Jueptner, *Digital holography.* New York: Springer, 2004.

[15] J. Goodman and R. Lawrence, "Digital image formation from electronically detected holograms," *Applied physics letters*, vol. 11, p. 77, 1967.

[16] C. Barsi, W. Wan, and J. W. Fleischer, "Imaging through nonlinear media using digital holography," *Nature Photonics*, vol. 3, pp. 211–215, Apr. 2009.

[17] I. Yamaguchi and T. Zhang, "Phase-shifting digital holography," *Optics Letters*, vol. 22, pp. 1268–1270, 1997.

[18] E. Cuche, P. Marquet, and C. Depeursinge, "Simultaneous amplitude-contrast and quantitative phase-contrast microscopy by numerical reconstruction of Fresnel off-axis holograms," *Applied Optics*, vol. 38, no. 34, pp. 6994–7001, 1999.

[19] E. Cuche, F. Bevilacqua, and C. Depeursinge, "Digital holography for quantitative phase-contrast imaging," *Optics Letters*, vol. 24, no. 5, pp. 291–293, 1999.

[20] J. Goodman, *Introduction to Fourier Optics*, McGraw-Hill, Ed. McGraw-Hill Science/Engineering/Math, 1996.

[21] G. Nomarski and A. Weill, "Application la mtallographie des mthodes interfrentielles deux ondes polarises," *Rev. Metall.*, vol. 2, pp. 121–128, 1955.

[22] D. Murphy, *Differential interference contrast (DIC) microscopy and modulation contrast microscopy.* New York: Wiley-Liss, 2000.

[23] D. J. Stephens and V. J. Allan, "Light Microscopy Techniques for Live Cell Imaging," *Science*, vol. 300, no. 5616, pp. 82–86, 2003.

[24] C. Sheppard, "Advanced Light Microscopy. Vol. 2. Specialized Methods," *Journal of Modern Optics*, vol. 37, no. 7, pp. 1277–1278, 1990.

[25] C. J. Cogswell, N. I. Smith, K. G. Larkin, and P. Hariharan, "Quantitative DIC microscopy using a geometric phase shifter," C. J. Cogswell, J.-A. Conchello, and T. Wilson, Eds., vol. 2984, no. 1. SPIE, 1997, pp. 72–81.

[26] M. Arnison, K. Larkin, C. Sheppard, N. Smith, and C. Cogswell, "Linear phase imaging using differential interference contrast microscopy," *Journal of Microscopy*, vol. 214, pp. 7–12, 2004.

[27] S. V. King, A. Libertun, R. Piestun, C. J. Cogswell, and C. Preza, "Quantitative phase microscopy through differential interference imaging," *Journal of Biomedical Optics*, vol. 13, no. 2, p. 024020, 2008.

[28] E. Van Munster, L. Van Vliet, and J. Aten, "Reconstruction of optical pathlength distributions from images obtained by a wide-field differential interference contrast microscope," *Journal of Microscopy*, vol. 188, no. 2, pp. 149–157, 1997.

[29] S. Kou, L. Waller, G. Barbastathis, and C. Sheppard, "Transport-of-intensity approach to differential interference contrast (TI-DIC) microscopy for quantitative phase imaging," *Optics Letters*, vol. 35, no. 3, pp. 447–449, 2010.

[30] D. Drapcho and K. V. Donck, "Label-free live-cell imaging for high-content screening," *Photonics.com*, vol. November, 2009.

[31] M. Born and E. Wolf, *Principles of Optics*, Born, M. & Wolf, E., Ed. Pergamon Press, 1959.

[32] G. Stroke, *An introduction to coherent optics and holography*, G. Stroke, Ed. Academic Press, 1966.

[33] B. Platt, "History and principles of Shack-Hartmann wavefront sensing," *Journal of Refractive Surgery*, vol. 17, no. 5, pp. 573–577, 2001.

[34] R. Gerchberg and W. Saxton, "A practical algorithm for the determination of phase from image and diffraction plane pictures," *Optik*, vol. 35, pp. 237–246, 1972.

[35] J. Fienup, "Reconstruction of an object from the modulus of its fourier transform," *Optics Letters*, vol. 3, 1978.

[36] ——, "Phase retrieval algorithms: a comparison," *Applied Optics*, vol. 21, 1982.

[37] J. Cederquist, J. Fienup, C. Wackerman, S. Robinson, and D. Kryskowski, "Wave-front phase estimation from fourier intensity measurements," *Journal of the Optical Society of America A*, vol. 6, no. 7, pp. 1020–1027, 1989.

[38] R. Gonsalves, "Phase retrieval from modulus data," *Journal of the Optical Society of America A*, vol. 66, pp. 961–964, 1976.

[39] G. Yang, B. Dong, B. Gu, J. Zhuang, and O. Ersoy, "Gerchberg-Saxton and Yang-Gu algorithms for phase retrieval in a nonunitary transform system: a comparison," *Applied Optics*, vol. 33, no. 2, pp. 209–218, 1994.

[40] R. Rolleston and N. George, "Image reconstruction from partial Fresnel zone information," *Applied Optics*, vol. 25, no. 2, pp. 178–183, 1986.

[41] ——, "Stationary phase approximations in Fresnel-zone magnitude-only reconstructions," *Journal of the Optical Society of America A*, vol. 4, no. 1, pp. 148–153, 1987.

[42] J. Fienup, "Iterative method applied to image reconstruction and to computer-generated holograms," *Optical Engineering*, vol. 19, no. 3, pp. 291–305, 1980.

[43] R. Piestun and J. Shamir, "Control of wave-front propagation with diffractive elements," *Optics Letters*, vol. 19, no. 11, pp. 771–773, 1994.

[44] Z. Zalevsky, D. Mendlovic, and R. Dorsch, "Gerchberg-Saxton algorithm applied in the fractional Fourier or the Fresnel domain," *Optics Letters*, vol. 21, 1996.

[45] J. A. Dominguez-Caballero, S. Takahashi, S. J. Lee, and G. Barbastathis, "Design and fabrication of computer generated holograms for Fresnel domain lithography," in *Digital Holography and Three-Dimensional Imaging.* Optical Society of America, 2009, p. DWB3.

[46] B. H. Dean and C. W. Bowers, "Diversity selection for phase-diverse phase retrieval," *Journal of the Optical Society of America A*, vol. 20, no. 8, pp. 1490–1504, 2003.

[47] S. Mayo, P. Miller, S. Wilkins, T. Davis, D. Gao, T. Gureyev, D. Paganin, D. Parry, A. Pogany, and A. Stevenson, "Quantitative x-ray projection microscopy: phase contrast and multi-spectral imaging," *Journal of Microscopy*, vol. 207, pp. 79–96, 2002.

[48] H. Stark, Y. Yang, and Y. Yang, *Vector Space Projections: A Numerical Approach to Signal and Image Processing, Neural Nets, and Optics.* New York, NY, USA: John Wiley & Sons, Inc., 1998.

[49] T. Gerke and R. Piestun, "Aperiodic volume optics," *Nature Photonics*, vol. 4, no. 3, pp. 188–193, 2010.

[50] S. Pavani and R. Piestun, "High-efficiency rotating point spread functions," *Optics Express*, vol. 16, no. 5, pp. 3484–3489, 2008.

[51] A. Devaney and R. Childlaw, "On the uniqueness question in the problem of phase retrieval from intensity measurements," *Journal of the Optical Society of America*, vol. 68, pp. 1352–1354, 1978.

[52] J. Fienup, "Reconstruction of a complex-valued object from the modulus of its Fourier transform using a support constraint," *Journal of the Optical Society of America A*, vol. 4, pp. 118–123, 1987.

[53] L. J. Allen and M. P. Oxley, "Phase retrieval from series of images obtained by defocus variation," *Optics Communications*, vol. 199, no. 1-4, pp. 65 – 75, 2001.

[54] L. Allen, H. Faulkner, K. Nugent, M. Oxley, and D. Paganin, "Phase retrieval from images in the presence of first-order vortices," *Physical Review E*, vol. 63, no. 3, p. 37602, 2001.

[55] H. I. Campbell, S. Zhang, A. H. Greenaway, and S. Restaino, "Generalized phase diversity for wave-front sensing," *Optics Letters*, vol. 29, no. 23, pp. 2707–2709, 2004.

[56] R. Gonsalves, "Phase retrieval by differential intensity measurements," *Journal of the Optical Society of America A*, vol. 4, pp. 166–170, 1987.

[57] W. H. Southwell, "Wave-front analyzer using a maximum likelihood algorithm," *Journal of the Optical Society of America*, vol. 67, no. 3, pp. 396–399, 1977.

[58] R. Gonsalves, "Small-phase solution to the phase-retrieval problem," *Optics Letters*, vol. 26, no. 10, pp. 684–685, 2001.

[59] T. Gureyev, A. Pogany, D. Paganin, and S. Wilkins, "Linear algorithms for phase retrieval in the Fresnel region," *Optics Communications*, vol. 231, no. 1-6, pp. 53 – 70, 2004.

[60] D. Paganin, S. Mayo, T. Gureyev, P. Miller, and S. Wilkins, "Simultaneous phase and amplitude extraction from a single defocused image of a homogeneous object," *Journal of Microscopy*, vol. 206, no. 1, pp. 33–40, 2002.

[61] W.-X. Cong, N.-X. Chen, and B.-Y. Gu, "Phase retrieval in the fresnel transform system: a recursive algorithm," *Journal of the Optical Society of America A*, vol. 16, no. 7, pp. 1827–1830, 1999.

[62] S. G. Podorov, K. M. Pavlov, and D. M. Paganin, "A non-iterative reconstruction method for direct and unambiguous coherent diffractive imaging," *Optics Express*, vol. 15, no. 16, pp. 9954–9962, 2007.

[63] M. R. Teague, "Deterministic phase retrieval: a Green's function solution," *Journal of the Optical Society of America*, vol. 73, no. 11, pp. 1434–1441, 1983.

[64] N. Streibl, "Phase imaging by the transport equation of intensity," *Optical Communications*, vol. 49, no. 1, 1984.

[65] M. Teague *et al.*, "Image formation in terms of the transport equation," *Journal of the Optical Society of America A*, vol. 2, no. 11, pp. 2019–2026, 1985.

[66] K. A. Nugent, D. Paganin, and T. Gureyev, "A phase odyssey," *Physics Today*, vol. 54, no. 8, pp. 27–32, 2001.

[67] D. Paganin and K. Nugent, "Noninterferometric phase imaging with partially coherent light," *Physical Review Letters*, vol. 80, no. 12, 1995.

[68] E. Barone-Nugent, A. Barty, and K. Nugent, "Quantitative phase-amplitude microscopy I: optical microscopy," *Journal of Microscopy*, vol. 206, pp. 194–203, 2002.

[69] A. Barty, K. Nugent, D. Paganin, and A. Roberts, "Quantitative optical phase microscopy," *Optics Letters*, vol. 23, no. 11, pp. 817–819, 1998.

[70] R. Gonsalves, "Phase retrieval and diversity in adaptive optics," *Optical Engineering*, vol. 21, pp. 829–832, 1982.

[71] R. G. Paxman, T. J. Schulz, and J. R. Fienup, "Joint estimation of object and aberrations by using phase diversity," *Journal of the Optical Society of America A*, vol. 9, no. 7, pp. 1072–1085, 1992.

[72] J. H. Seldin and R. G. Paxman, "Joint estimation of amplitude and phase from phase-diversity data," in *Adaptive Optics: Analysis and Methods/Computational Optical Sensing and Imaging/Information Photonics/Signal Recovery and Synthesis Topical Meetings on CD-ROM.* Optical Society of America, 2005, p. JTuB4.

[73] D. J. Lee, M. C. Roggemann, and B. M. Welsh, "Cramér-rao analysis of phase-diverse wave-front sensing," *Journal of the Optical Society of America A*, vol. 16, no. 5, pp. 1005–1015, 1999.

[74] R. G. Paxman and J. R. Fienup, "Optical misalignment sensing and image reconstruction using phase diversity," *Journal of the Optical Society of America A*, vol. 5, no. 6, pp. 914–923, 1988.

[75] D. Lee, M. Roggemann, B. Welsh, and E. Crosby, "Evaluation of least-squares phase-diversity technique for space telescope wave-front sensing," *Applied Optics*, vol. 36, no. 35, pp. 9186–9197, 1997.

[76] M. Roggemann, D. Tyler, and M. Bilmont, "Linear reconstruction of compensated images: theory and experimental results," *Applied Optics*, vol. 31, no. 35, pp. 7429–7441, 1992.

[77] L. Mugnier and G. Rousset, "Noise propagation in wave-front sensing with phase diversity," *Applied Optics*, vol. 38, p. 23, 1999.

[78] D. Brady, *Optical imaging and Spectroscopy.* Wiley Interscience, 2009.

[79] C.-H. Chang, L. Waller, and G. Barbastathis, "Design and optimization of broadband wide-angle antireflection structures for binary diffractive optics," *Optics Letters*, vol. 35, no. 7, pp. 907–909, 2010.

[80] M. A. Neifeld and J. Ke, "Optical architectures for compressive imaging," *Applied Optics*, vol. 46, no. 22, pp. 5293–5303, 2007.

[81] A. Kak and M. Slaney, *Principles of Computerized Tomographic Imaging.* Philadelphia: Society for Industrial and Applied Mathematics, 2001.

[82] M. G. Raymer, M. Beck, and D. McAlister, "Complex wave-field reconstruction using phase-space tomography," *Phys. Rev. Lett.*, vol. 72, no. 8, pp. 1137–1140, Feb 1994.

[83] J. Edward R. Dowski and W. T. Cathey, "Extended depth of field through wave-front coding," *Applied Optics*, vol. 34, no. 11, pp. 1859–1866, 1995.

[84] A. Levin, R. Fergus, F. Durand, and W. T. Freeman, "Image and depth from a conventional camera with a coded aperture," *ACM Trans. Graph.*, vol. 26, no. 3, p. 70, 2007.

[85] M. Levoy and P. Hanrahan, "Light field rendering," in *SIGGRAPH '96: Proceedings of the 23rd annual conference on Computer graphics and interactive techniques.* New York, NY, USA: ACM, 1996, pp. 31–42.

[86] G. Lippmann, "La photographie integrale," *Comptes-Rendus*, vol. 146, pp. 446–451, 1908.

[87] R. Raskar, A. Agrawal, and J. Tumblin, "Coded exposure photography: motion deblurring using fluttered shutter," *ACM Trans. Graph.*, vol. 25, no. 3, pp. 795–804, 2006.

[88] W. Liu, D. Psaltis, and G. Barbastathis, "Real-time spectral imaging in three spatial dimensions," *Optics Letters*, vol. 27, no. 10, pp. 854–856, 2002.

[89] S. Webb, *From the watching of shadows: the origins of radiological tomography.* Taylor & Francis, 1990.

[90] J. Radon, "ber die Bestimmung von Funktionen durch ihre Integralwerte lngs gewisser Mannigfaltigkeiten," *Math.-Phys. Kl.*, vol. 69, pp. 262–277, 1917.

[91] M. Bertero, *Inverse Problems in Imaging.* Bristol: Institute of Physics, 2002.

[92] J. Prince and A. Willsky, "Constrained sinogram restoration for limited-angle tomography," *Optical Engineering*, vol. 29, pp. 535–545, 1990.

[93] J. L. Prince and A. S. Willsky, "A geometric projection-space reconstruction algorithm," *Linear Algebra and its Applications*, vol. 130, pp. 151 – 191, 1990.

[94] C. Brown, D. Burns, F. Spelman, and A. Nelson, "Computed tomography from optical projections for three-dimensional reconstruction of thick objects," *Applied Optics*, vol. 31, no. 29, pp. 6247–6254, 1992.

[95] D. W. Sweeney and C. M. Vest, "Reconstruction of three-dimensional refractive index fields from multidirectional interferometric data," *Applied Optics*, vol. 12, no. 11, pp. 2649–2664, 1973.

[96] R. Snyder and L. Hesselink, "High speed optical tomography for flow visualization," *Applied Optics*, vol. 24, no. 23, pp. 4046–4051, 1985.

[97] C. Soller, R. Wenskus, P. Middendorf, G. Meier, and F. Obermeier, "Interferometric tomography for flow visualization of density fields in supersonic jets and convective flow," *Applied Optics*, vol. 33, no. 14, pp. 2921–2932, 1994.

[98] W. Choi, C. Fang-Yen, K. Badizadegan, S. Oh, N. Lue, R. Dasari, and M. Feld, "Tomographic phase microscopy," *Nature Methods*, vol. 4, no. 9, 2007.

[99] N. Jayshree, G. Datta, and R. Vasu, "Optical tomographic microscope for quantitative imaging of phase objects," *Applied Optics*, vol. 39, no. 2, pp. 277–283, 2000.

[100] A. Barty, K. Nugent, A. Roberts, and D. Paganin, "Quantitative phase tomography," *Optical Communications*, vol. 175, 2000.

[101] T. Noda, S. Kawata, and S. Minami, "Three-dimensional phase-contrast imaging by a computed-tomography microscope," *Applied Optics*, vol. 31, no. 5, pp. 670–674, 1992.

[102] F. Charrière, A. Marian, F. Montfort, J. Kuehn, T. Colomb, E. Cuche, P. Marquet, and C. Depeursinge, "Cell refractive index tomography by digital holographic microscopy," *Optics letters*, vol. 31, no. 2, pp. 178–180, 2006.

[103] A. Devaney, "A filtered backpropagation algorithm for diffraction tomography," *Ultrasonic Imaging*, vol. 4, no. 4, pp. 336 – 350, 1982.

[104] M. Maleki and A. Devaney, "Phase-retrieval and intensity-only reconstruction algorithms for optical diffraction tomography," *Journal of the Optical Society of America A*, vol. 10, no. 5, pp. 1086–1092, 1993.

[105] E. Wolf, "Principles and Development of Diffraction Tomography,," *Trends in Optics: Research, Developments and Applications*, pp. 83–110, 1996.

[106] B. Stamnes, "Validity of diffraction tomography based on the first Born and the first Rytov approximations," *Appl. Opt*, vol. 37, pp. 2996–3006, 1998.

[107] V. Lauer, "New approach to optical diffraction tomography yielding a vector equation of diffraction tomography and a novel tomographic microscope," *Journal of Microscopy*, vol. 205, pp. 165–176, 2002.

[108] S. S. Kou and C. J. Sheppard, "Imaging in digital holographic microscopy," *Opt. Express*, vol. 15, no. 21, pp. 13 640–13 648, 2007.

[109] S. S. Kou and C. J. R. Sheppard, "Image formation in holographic tomography," *Opt. Lett.*, vol. 33, no. 20, pp. 2362–2364, 2008.

[110] G. Gbur and E. Wolf, "Diffraction tomography without phase information," *Optics letters*, vol. 27, no. 21, pp. 1890–1892, 2002.

[111] G. Gbur, M. Anastasio, Y. Huang, and D. Shi, "Spherical-wave intensity diffraction tomography," *Journal of the Optical Society of America A*, vol. 22, no. 2, pp. 230–238, 2005.

[112] M. Anastasio, D. Shi, Y. Huang, and G. Gbur, "Image reconstruction in spherical-wave intensity diffraction tomography," *Journal of the Optical Society of America A*, vol. 22, no. 12, pp. 2651–2661, 2005.

[113] G. Gbur and E. Wolf, "Hybrid diffraction tomography without phase information," *Journal of the Optical Society of America A*, vol. 19, no. 11, pp. 2194–2202, 2002.

[114] J. Wyant, "Interferometric optical metrology: basic systems and principles," *Laser Focus*, vol. 65-71, 1982.

[115] Y. Hu, J. Xi, J. Chicharo, E. Li, and Z. Yang, "Discrete cosine transform-based shift estimation for fringe pattern profilometry using a generalized analysis model," *Applied Optics*, vol. 45, no. 25, 2006.

[116] H. Yun and C. Hong, "Interframe intensity correlation matrix for self-calibration in phase-shifting interferometry," *Applied Optics*, vol. 44, no. 23, pp. 4860–4869, 2005.

[117] J. Schwider and R. Burow, "Digital wavefront measuring interferometry: some systematic error sources," *Applied Optics*, vol. 22, no. 21, 1983.

[118] K. Creath, "Phase-measurement interferometry: Beware these errors," *SPIE*, vol. 1553, 1991.

[119] L. Waller and G. Barbastathis, "Error analysis of phase-shifting for phase and amplitude tomographic reconstruction," *Adaptive Optics: Analysis and Methods/Computational Optical Sensing and Imaging/Information Photonics/Signal Recovery and Synthesis Topical Meetings*, 2007.

[120] R. Rangayyan, A. Dhawan, and R. Gordon, "Algorithms for limited-view computed tomography: an annotated bibliography and a challenge," *Applied Optics*, vol. 24, no. 23, pp. 4000–4013, 1985.

[121] T. Inouye, "Image reconstruction with limited angle projection data," *IEEE Transactions on Nuclear Science*, vol. NS-26, pp. 2666–2671, 1979.

[122] M. Davison, "The ill-conditioned nature of the limited angle tomography problem," *SIAM Journal on Applied Mathematics*, vol. 43, no. 2, pp. 428–448, 1983.

[123] K. Tam and V. Perez-Mendez, "Tomographical imaging with limited-angle input," *Journal of the Optical Society of America*, vol. 71, no. 5, pp. 582–593, 1981.

[124] E. Payot, F. Preteux, Y. Trousset, and R. Guillemaud, "3D reconstruction from incomplete fourier spectra: An extrapolation approach," *Statistical and stochastic methods for image processing*, vol. 2823, 1996.

[125] M. Ravichandran and F. Gouldin, "Reconstruction of smooth distributions from a limited number of projections," *Applied Optics*, 1988.

[126] A. Oppenheim, R. Schafer, and J. Buck, *Discrete-time signal processing.* New Jersey: Prentice Hall, 1999.

[127] T. Ursell, "The diffusion equation a multi-dimensional tutorial," October 2007, `http://www.rpgroup.caltech.edu/ natsirt/aph162/diffusion.pdf`.

[128] L. Waller, J. Kim, Y. Shao-Horn, and G. Barbastathis, "Interferometric tomography of fuel cells for monitoring membrane water content," *Optics Express*, vol. 17, no. 17, pp. 14 806–14 816, 2009.

[129] A. LaConti, M. Hamilton, and R. McDonald, *Handbook of Fuel Cells - Fundamentals, Technology, and Applications.* Wiley, 2003.

[130] C. Thawornkuno and C. Panjapornpon, "Estimation of water content in PEM fuel cell," *Chiang Mai J. Sci.*, vol. 35, no. 1, pp. 202–220, 2008.

[131] D. Wilkinson and J. St-Pierre, "In-plane gradients in fuel cell structure and conditions for higher performance," *Journal of Power Sources*, vol. 113, 2003.

[132] S. Knights, K. Colbow, J. St-Pierre, and D. Wilkinson, "Aging mechanisms and lifetime of PEFC and DMFC," *Journal of Power Sources*, vol. 127, 2004.

[133] U. Pasaogullari and C. Wang, "Liquid water transport in gas diffusion layer of polymer electrolyte fuel cells," *Journal of the Electrochemical Society*, vol. 151, no. 3, 2004.

[134] I. Manke, C. Hartnig, M. Grünerbel, J. Kaczerowski, W. Lehnert, N. Kardjilov, A. Hilger, J. Banhart, W. Treimer, and M. Strobl, "Quasi-in situ neutron tomography on polymer electrolyte membrane fuel cell stacks," *Applied Physics Letters*, vol. 90, no. 18, p. 184101, 2007.

[135] F.-Y. Zhang, D. Spernjak, A. K. Prasad, and S. G. Advani, "In situ characterization of the catalyst layer in a Polymer Electrolyte Membrane fuel cell," *Journal of The Electrochemical Society*, vol. 154, no. 11, pp. B1152–B1157, 2007.

[136] J. St-Pierre, "PEMFC in situ liquid-water-content monitoring status," *Journal of the Electrochemical Society*, vol. 154, no. 7, 2007.

[137] S. Tsushima, K. Teranishi, K. Nishida, and S. Hirai, "Water content distribution in a polymer electrolyte membrane for advanced fuel cell system with liquid water supply," *Magnetic Resonance Imaging*, vol. 23, 2005.

[138] S. Tsushima, K. Teranishi, and S. Hirai, "Magnetic resonance imaging of the water distribution within a polymer electrolyte membrane in fuel cells," *Electrochemical and Solid-State Letters*, vol. 7, no. 9, pp. A269–A272, 2004.

[139] R. Satija, D. Jacobson, M. Arif, and S. Werner, "In situ neutron imaging technique for evaluation of water management systems in operating PEM fuel cells," *Journal of Power Sources*, vol. 129, 2004.

[140] R. Mosdale, G. Gebel, and M. Pineri, "Water profile determination in a running proton exchange membrane fuel cell using small-angle neutron scattering," *Journal of Membrane Science*, vol. 118, no. 2, pp. 269 – 277, 1996.

[141] N. Pekula, K. Heller, P. A. Chuang, A. Turhan, M. M. Mench, J. S. Brenizer, and K. Ünlü, "Study of water distribution and transport in a polymer electrolyte fuel cell using neutron imaging," *Nuclear Instruments and Methods in Physics Research A*, vol. 542, pp. 134–141, 2005.

[142] R. J. Bellows, M. Y. Lin, M. Arif, A. K. Thompson, and D. Jacobson, "Neutron imaging technique for in situ measurement of water transport gradients within nafion in polymer electrolyte fuel cells," *Journal of The Electrochemical Society*, vol. 146, no. 3, pp. 1099–1103, 1999.

[143] P. K. Sinha, P. Halleck, and C.-Y. Wang, "Quantification of liquid water saturation in a pem fuel cell diffusion medium using x-ray microtomography," *Electrochemical and Solid-State Letters*, vol. 9, no. 7, pp. A344–A348, 2006.

[144] D. Spernjak, A. K. Prasad, and S. G. Advani, "Experimental investigation of liquid water formation and transport in a transparent single-serpentine pem fuel cell," *Journal of Power Sources*, vol. 170, no. 2, pp. 334 – 344, 2007.

[145] K. Tber, D. Pcza, and C. Hebling, "Visualization of water buildup in the cathode of a transparent pem fuel cell," *Journal of Power Sources*, vol. 124, no. 2, pp. 403 – 414, 2003.

[146] Y. Patil, T. Seery, M. Shaw, and R. Parnas, "In situ water sensing in a Nafion membrane by fluorescence spectroscopy," *Industrial and Engineering Chemistry Research*, vol. 44, 2005.

[147] A. Bazylak, "Liquid water visualization in pem fuel cells: A review," *International Journal of Hydrogen Energy*, vol. 34, no. 9, pp. 3845 – 3857, 2009.

[148] M. Weiss, R. Srivastava, and H. Groger, "Experimental investigation of a surface plasmon-based integrated-optic humidity sensor," *Electronics Letters*, vol. 32, no. 8, 1996.

[149] K. H. Choi, D. J. Park, Y. W. Rho, Y. T. Kho, and T. H. Lee, "A study of the internal humidification of an integrated PEMFC stack," *Journal of Power Sources*, vol. 74, no. 1, pp. 146 – 150, 1998.

[150] E. Alanis, G. Romero, and C. Martinez, "Interferometric measurement of diffusion coefficients through a scanning laser beam," *Optical Engineering*, vol. 39, no. 3, 2000.

[151] J. Kim, L. Waller, G. Barbastathis, and Y. Shao-Horn, "Temperature and water content measurements of nafion membrane in PEM fuel cells by laser interferometry," *Proceedings of the Electrochemical Society*, 2005.

[152] ——, "Methodology to understand the degradation mechanism of nafion membrane in PEM fuel cells," *Electrochemical Society Transactions*, vol. 1, no. 8, 2006.

[153] ——, "Water transport in nafion membrane measured by laser interferometry," *Proceedings of the Electrochemical Society*, vol. 702, no. 420, 2007.

[154] A. Leis, S. Schlicher, H. Franke, and M. Strathmann, "Optically transparent porous medium for nondestructive studies of microbial biofilm architecture and transport dynamics," *Applied and Environmental Microbiology*, pp. 4801–4808, 2005.

[155] J. Huntley and H. Saldner, "Temporal phase-unwrapping algorithm for automated interferogram analysis," *Applied Optics*, vol. 32, no. 17, pp. 3047–3051, 1993.

[156] S. Motupally, A. Becker, and J. Weidner, "Diffusion of water in Nafion 115 membranes," *Journal of the Electrochemical Society*, vol. 147, no. 9, 2000.

[157] T. Zawodzinski, T. Springer, J. Davey, R. Jestel, C. Lopez, J. Valerio, and J. Gottesfeld, "A comparative study of water uptake by and transport through ionomeric fuel cell membranes," *Journal of the Electrochemical Society*, vol. 140, no. 7, 1993.

[158] S. Bajt, A. Barty, K. Nugent, M. McCartney, M. Wall, and D. Paganin, "Quantitative phase-sensitive imaging in a transmission electron microscope," *Ultramicroscopy*, vol. 83, no. 1, pp. 67–73, 2000.

[159] T. Gureyev and S. Wilkins, "On x-ray phase retrieval from polychromatic images," *Optics Communications*, vol. 147, no. 4-6, pp. 229 – 232, 1998.

[160] T. Gureyev, C. Raven, A. Snigirev, I. Snigireva, and S. Wilkins, "Hard x-ray quantitative non-interferometric phase-contrast microscopy," *Journal of Physics D: Applied Physics*, vol. 32, pp. 563–567, 1999.

[161] B. Allman, P. McMahon, K. Nugent, D. Paganin, D. Jacobson, M. Arif, and S. Werner, "Phase radiography with neutrons." *Nature*, 2000.

[162] M. De Graef and Y. Zhu, "Quantitative noninterferometric Lorentz microscopy," *Journal of Applied Physics*, vol. 89, p. 7177, 2001.

[163] K. Nugent and D. Paganin, "Matter-wave phase measurement: a noninterferometric approach," *Physical Review A*, vol. 61, no. 6, p. 63614, 2000.

[164] C. Curl, T. Harris, P. Harris, B. Allman, C. Bellair, A. Stewart, and L. Delbridge, "Quantitative phase microscopy: a new tool for measurement of cell culture growth and confluency in situ," *Pfl "ugers Archiv European Journal of Physiology*, vol. 448, no. 4, pp. 462–468, 2004.

[165] P. McMahon, E. Barone-Nugent, B. Allman, and K. Nugent, "Quantitative phase-amplitude microscopy II: differential interference contrast imaging for biological TEM," *Journal of microscopy*, vol. 206, no. 3, pp. 204–208, 2002.

[166] K. Ichikawa, A. Lohmann, and M. Takeda, "Phase retrieval based on the irradiance transport equation and the Fourier transform method: experiments," *Applied Optics*, vol. 27, no. 16, 1988.

[167] J. Quiroga, J. Gómez-Pedrero, and J. Martínez-Antón, "Wavefront measurement by solving the irradiance transport equation for multifocal systems," *Optical engineering*, vol. 40, p. 2885, 2001.

[168] J. Tiller, A. Barty, D. Paganin, and K. Nugent, "The holographic twin image problem: a deterministic phase solution," *Optics Communications*, vol. 183, no. 1-4, pp. 7–14, 2000.

[169] M. Beleggia, M. Schofield, V. Volkov, and Y. Zhu, "On the transport of intensity technique for phase retrieval," *Ultramicroscopy*, vol. 102, 2002.

[170] D. VanDyck and W. Coene, "A new procedure for wave function restoration in high resolution electron microscopy," *Optik*, vol. 77, no. 3, pp. 125–128, 1987.

[171] D. F. Lynch, A. F. Moodie, and M. A. O'Keefe, "n-beam lattice images. v. the use of the charge-density approximation in the interpretation of lattice images," *Acta Crystallographica Section A*, vol. 31, pp. 300–307, 1975.

[172] M. Tsang and D. Psaltis, "Metaphoric optical computing of fluid dynamics," in *Conference on Lasers and Electro-Optics/Quantum Electronics and Laser Science and Photonic Applications Systems Technologies.* Optical Society of America, 2005, p. QML6.

[173] M. Tsang, D. Psaltis, J. H. Shapiro, and S. Lloyd, "Optical hydrodynamics," in *Frontiers in Optics.* Optical Society of America, 2008, p. FWO3.

[174] W. Wan, S. Jia, and J. W. Fleischer, "Dispersive superfluid-like shock waves in nonlinear optics," *Nature Physics*, vol. 3, pp. 46–51, 2007.

[175] M. J. Mercier, N. B. Garnier, and T. Dauxois, "Reflection and diffraction of internal waves analyzed with the Hilbert transform," *Physics of Fluids*, vol. 20, no. 8, p. 86601, 2008.

[176] M. Mathur and T. Peacock, "Internal wave interferometry," *Phys. Rev. Lett.*, vol. 104, no. 11, p. 118501, 2010.

[177] G. Strang, *Computational Science and Engineering.* Cambridge, MA: Wellesley-Cambridge Press, 2007.

[178] T. E. Gureyev and K. A. Nugent, "Rapid quantitative phase imaging using the transport of intensity equation," *Optics Communications*, vol. 133, no. 1-6, pp. 339 – 346, 1997.

[179] M. Soto, S. Rios, and E. Acosta, "Role of boundary conditions in phase estimation by transport of intensity equation," *Optical Communications*, vol. 184, 2000.

[180] V. Volkov, Y. Zhu, and M. De Graef, "A new symmetrized solution for phase retrieval using the transport of intensity equation," *Micron*, vol. 33, no. 5, pp. 411–416, 2002.

[181] M. Soto, E. Acosta, and S. Ríos, "Performance analysis of curvature sensors: optimum positioning of the measurement planes," *Opt. Express*, vol. 11, no. 20, pp. 2577–2588, 2003.

[182] D. Paganin, A. Barty, P. J. McMahon, and K. A. Nugent, "Quantitative phase-amplitude microscopy. iii. the effects of noise," *Journal of Microscopy*, vol. 214, no. 1, pp. 51–61, 2004.

[183] M. Soto and E. Acosta, "Improved phase imaging from intensity measurements in multiple planes," *Applied Optics*, vol. 46, no. 33, pp. 7978–7981, 2007.

[184] L. Waller, L. Tian, and G. Barbastathis, "Transport of intensity imaging with higher order derivatives," in *Computational Optical Sensing and Imaging.* Optical Society of America, 2009, p. CThA3.

[185] T. E. Gureyev, D. M. Paganin, A. W. Stevenson, S. C. Mayo, and S. W. Wilkins, "Generalized eikonal of partially coherent beams and its use in quantitative imaging," *Phys. Rev. Lett.*, vol. 93, no. 6, p. 068103, 2004.

[186] N. Streibl, "Three-dimensional imaging by a microscope," *J. Opt. Soc. Am. A*, vol. 2, no. 2, pp. 121–127, 1985.

[187] C. J. R. Sheppard, "Three-dimensional phase imaging with the intensity transport equation," *Appl. Opt.*, vol. 41, no. 28, pp. 5951–5955, 2002.

[188] S. W. Wilkins, T. E. Gureyev, D. Gao, A. Pogany, and A. W. Stevenson, "Phase-contrast imaging using polychromatic hard x-rays," *Nature*, vol. 384, pp. 335–338, 1996.

[189] T. E. Gureyev, "Composite techniques for phase retrieval in the Fresnel region," *Optics Communications*, vol. 220, no. 1-3, pp. 49 – 58, 2003.

[190] T. Gureyev, I. Nesterets, D. Paganin, A. Pogany, and S. Wilkins, "Linear algorithms for phase retrieval in the Fresnel region. 2. partially coherent illumination," *Optics Communications*, vol. 259, no. 2, pp. 569 – 580, 2006.

[191] L. Waller, L. Tian, and G. Barbastathis, "Transport of intensity imaging with higher order derivatives," *Optics Express*, no. submitted, 2010.

[192] M. Langer, P. Cloetens, J.-P. Guigay, and F. Peyrin, "Quantitative comparison of direct phase retrieval algorithms in in-line phase tomography," *Medical Physics*, vol. 35, no. 10, pp. 4556–4567, 2008.

[193] J. Crassidis and J. Junkins, *Optimal Estimation of Dynamic Systems.* Boca Raton, FL, USA: Chapman & Hall/CRC, 2004.

[194] H. L. V. Trees, *Detection, Estimation, and Modulation Theory. Part III: Radar-Sonar Signal Processing and Gaussian Signals in Noise.* Melbourne, FL, USA: Krieger Publishing Co., Inc., 1992.

[195] D. Simon, *Optimal State Estimation: Kalman, H Infinity, and Nonlinear Approaches.* Wiley-Interscience, 2006.

[196] K. Nishiyama and T. Mita, "Frequency spectrum estimation method using complex Kalman filter," *Electronics and Communications in Japan*, vol. 72, no. 2, pp. 1749–1759, 1989.

[197] L. Waller and G. Barbastathis, "Phase from defocused color images," in *Frontiers in Optics.* Optical Society of America, 2009, p. FThR3.

[198] B. Saleh and M. Teich, *Fundamentals of Photonics.* New York: John Wiley & Sons, 1991.

[199] H. C. King, *The history of the telescope.*, H. C. King, Ed. Dover Publications, 1979.

[200] M. White, *Isaac Newton : The Last Sorcerer.* Reading, EUA : Addison-Wesley, 1997.

[201] J. S. Courtney-Pratt and R. L. Gregory, "Microscope with enhanced depth of field and 3-d capability," *Applied Optics*, vol. 12, no. 10, pp. 2509–2519, 1973.

[202] G. Molesini and F. Quercioli, "Pseudocolor effects of longitudinal chromatic aberration," *Journal of Optics*, vol. 17, no. 6, p. 279, 1986.

[203] M. Browne, O. Akinyemi, and A. Boyde, "Confocal surface profiling utilizing chromatic aberration," *Scanning*, vol. 14, pp. 145–153, 1992.

[204] R. Juskaitis and T. Wilson, "A method for characterizing longitudinal chromatic aberration of microscope objectives using a confocal optical system," *Journal of Microscopy*, vol. 195, no. 1, pp. 17–22, 1999.

[205] F. Guichard, H. Nguyen, R. Tessières, M. Pyanet, I. Tarchouna, and F. Cao, "Extended depth-of-field using sharpness transport across color channels," in *Proceedings of SPIE*, vol. 7250, 2009, p. 72500N.

[206] H. H. Hopkins, "The frequency response of a defocused optical system," *Royal Society of London Proceedings Series A*, vol. 231, pp. 91–103, July 1955.

[207] T. Gureyev and S. Wilkins, "On x-ray phase retrieval from polychromatic images: Erratum," *Optics Communications*, vol. 154, p. 391, 1998.

[208] T. E. Gureyev, S. Mayo, S. W. Wilkins, D. Paganin, and A. W. Stevenson, "Quantitative in-line phase-contrast imaging with multienergy x rays," *Phys. Rev. Lett.*, vol. 86, no. 25, pp. 5827–5830, Jun 2001.

[209] M. A. Anastasio, Q. Xu, and D. Shi, "Multispectral intensity diffraction tomography: single material objects with variable densities," *Journal of the Optical Society of America A*, vol. 26, no. 2, pp. 403–412, 2009.

[210] E. Hecht, *Optics*. Addison-Wesley, 2002.

[211] S. L. Dobson, P. chen Sun, and Y. Fainman, "Diffractive lenses for chromatic confocal imaging," *Applied Optics*, vol. 36, no. 20, pp. 4744–4748, 1997.

[212] T. G. Bifano, R. K. Mali, J. K. Dorton, J. Perreault, N. Vandelli, M. N. Horenstein, and D. A. Castanon, "Continuous-membrane surface-micromachined silicon deformable mirror," *Optical Engineering*, vol. 36, no. 5, pp. 1354–1360, 1997.

[213] J. A. Perreault, T. G. Bifano, B. M. Levine, and M. N. Horenstein, "Adaptive optic correction using microelectromechanical deformable mirrors," *Optical Engineering*, vol. 41, no. 3, pp. 561–566, 2002.

[214] S. N. Kasarova, N. G. Sultanova, C. D. Ivanov, and I. D. Nikolov, "Analysis of the dispersion of optical plastic materials," *Optical Materials*, vol. 29, pp. 1481–1490, 2007.

[215] T. Shimobaba, T. Ito, N. Masuda, Y. Abe, Y. Ichihashi, H. Nakayama, N. Takada, A. Shiraki, and T. Sugie, "Numerical calculation library for diffraction integrals using the graphic processing unit: the GPU-based wave optics library," *Journal of Optics A: Pure and Applied Optics*, vol. 10, p. 075308, 2008.

[216] T. Shimobaba, Y. Sato, J. Miura, M. Takenouchi, and T. Ito, "Real-time digital holographic microscopy using the graphic processing unit," *Optics Express*, vol. 16, pp. 11 776–11 781, 2008.

[217] J. Fung and S. Mann, "Computer vision signal processing on graphics processing units," in *Proceedings of the IEEE International Conference on Acoustics, Speech, and Signal Processing (ICASSP 2004)*, 2004, pp. 83–89.

[218] Y. Allusse, P. Horain, A. Agarwal, and C. Saipriyadarshan, "GpuCV: An open-source GPU-accelerated framework for image processing and computer vision," in *MM08: Proceeding of the 16th ACM international conference on Multimedia*, 2008, pp. 1089–1092.

[219] N. Loomis, L. Waller, and G. Barbastathis, "High-speed phase recovery using chromatic transport of intensity computation in graphics processing units," in *Digital Holography*. Optical Society of America, 2010, p. JMA7.

[220] L. Waller, Y. Luo, and G. Barbastathis, "Quantitative phase imaging in a volume holographic microscope," P. K. Rastogi and E. Hack, Eds., vol. 1236, no. 1. AIP, 2010, pp. 76–80.

[221] Y. Luo, P. Gelsinger, J. Barton, G. Barbastathis, and R. Kostuk, "Optimization of multiplexed holographic gratings in PQ-PMMA for spectral-spatial imaging filters," *Optics Letters*, vol. 33, no. 6, pp. 566–568, 2008.

[222] G. Barbastathis, M. Balberg, and D. Brady, "Confocal microscopy with a volume holographic filter," *Optics Letters*, vol. 24, no. 12, pp. 811–813, 1999.

[223] Y. Luo, P. Gelsinger, E. De Leon, J. Harwell, J. Barton, R. Kostuk, and G. Barbastathis, "Phase Contrast Volume-Holographic Microscope," *Frontiers in Optics*, 2009.

[224] P. van Heerden, "Theory of optical information storage in solids," *SPIE Milestone Series MS*, vol. 171, pp. 427–434, 2001.

[225] Y. Luo, S. Oh, and G. Barbastathis, "Wavelength-coded multifocal microscopy," *Optics Letters*, vol. 35, pp. 781–783, 2010.

[226] G. Barbastathis, "The transfer function of volume holographic optical systems," in *Photorefractive Materials and Their Applications 3*. Springer Berlin, 2007, pp. 51–76.

[227] P. Blanchard and A. Greenaway, "Simultaneous multiplane imaging with a distorted diffraction grating," *Applied optics*, vol. 38, pp. 6692–6699, 1999.

[228] P. Blanchard, D. Fisher, S. Woods, and A. Greenaway, "Phase-diversity wavefront sensing with a distorted diffraction grating," *Applied Optics*, vol. 39, no. 35, pp. 6649–6655, 2000.

[229] X. Fengjie, J. Zongfu, X. Xiaojun, and G. Yifeng, "High-diffractive-efficiency defocus grating for wavefront curvature sensing," *Journal of the Optical Society of America A*, vol. 24, no. 11, pp. 3444–3448, 2007.

[230] P. Blanchard and A. Greenaway, "Broadband simultaneous multiplane imaging," *Optics Communications*, vol. 183, no. 1-4, pp. 29–36, 2000.

[231] H. Kogelnik, "Coupled wave theory for thick hologram gratings," *The Bell System Technical Journal, Vol. 48, no. 9, November 1969, pp. 2909-2947*, vol. 48, pp. 2909–2947, 1969.

[232] C. Gu, J. Hong, I. McMichael, R. Saxena, and F. Mok, "Cross-talk-limited storage capacity of volume holographic memory," *Journal of the Optical Society of America A*, vol. 9, no. 11, pp. 1978–1983, 1992.

[233] K. Curtis and D. Psaltis, "Cross talk in phase-coded holographic memories," *Journal of the Optical Society of America A*, vol. 10, no. 12, pp. 2547–2550, 1993.

[234] G. Barbastathis, M. Levene, and D. Psaltis, "Shift multiplexing with spherical reference waves," *Applied Optics*, vol. 35, no. 14, pp. 2403–2417, 1996.

[235] A. Sinha, G. Barbastathis, W. Liu, and D. Psaltis, "Imaging using volume holograms," *Optical Engineering*, vol. 43, no. 9, pp. 1959–1972, 2004.

[236] C. J. Bellair, C. L. Curl, B. E. Allman, P. J. Harris, A. Roberts, L. M. D. Delbridge, and K. A. Nugent, "Quantitative phase amplitude microscopy iv: imaging thick specimens," *Journal of Microscopy*, vol. 214, pp. 62–69, 2004.

[237] A. J. Meehan, P. Bedggood, B. Allman, K. A. Nugent, and A. B. Metha, "High resolution wavefront sensing and mirror control for vision science by quantitative phase imaging," in *Adaptive Optics: Methods, Analysis and Applications*. Optical Society of America, 2009, p. JWB5.

[238] F. Roddier, "Curvature sensing and compensation: a new concept in adaptive optics," *Appl. Opt.*, vol. 27, no. 7, pp. 1223–1225, 1988.

[239] ——, "Wavefront sensing and the irradiance transport equation," *Appl. Opt.*, vol. 29, no. 10, pp. 1402–1403, 1990.

[240] J. Kong, *Electromagnetic Wave theory*. Cambridge, MA: EMW Publishing, 2000.